DISSERTATION

A STUDY OF THE RELATIONSHIP BETWEEN THUNDERSTORM PROCESSES AND CLOUD-TOP ICE CRYSTAL SIZE

Submitted by

Daniel T. Lindsey

Department of Atmospheric Science

In partial fulfillment of the requirements

For the Degree of Doctor of Philosophy

Colorado State University

Fort Collins, Colorado

Summer 2008

UMI Number: 3332705

INFORMATION TO USERS

The quality of this reproduction is dependent upon the quality of the copy submitted. Broken or indistinct print, colored or poor quality illustrations and photographs, print bleed-through, substandard margins, and improper alignment can adversely affect reproduction.

In the unlikely event that the author did not send a complete manuscript and there are missing pages, these will be noted. Also, if unauthorized copyright material had to be removed, a note will indicate the deletion.

UMI®

UMI Microform 3332705
Copyright 2008 by ProQuest LLC.
All rights reserved. This microform edition is protected against unauthorized copying under Title 17, United States Code.

ProQuest LLC
789 E. Eisenhower Parkway
PO Box 1346
Ann Arbor, MI 48106-1346

COLORADO STATE UNIVERSITY

June 19, 2008

WE HEREBY RECOMMEND THAT THE DISSERTATION PREPARED UNDER OUR SUPERVISON BY DANIEL T. LINDSEY ENTITLED A STUDY OF THE RELATIONSHIP BETWEEN THUNDERSTORM PROCESSES AND CLOUD-TOP ICE CRYSTAL SIZE BE ACCEPTED AS FULFILLING IN PART REQUIREMENTS FOR THE DEGREE OF DOCTOR OF PHILOSOPHY.

Committee on Graduate Work

____

____

____

____

____

Advisor

____

Department Head

ABSTRACT OF DISSERTATION

A STUDY OF THE RELATIONSHIP BETWEEN THUNDERSTORM PROCESSES AND CLOUD-TOP ICE CRYSTAL SIZE

Satellite observations and numerical models are used to understand the physical mechanisms responsible for thunderstorms with varying cloud-top ice crystal sizes. Geostationary Operational Environmental Satellite (GOES) data are used to create a three-year climatology of cloud-top 3.9 μm reflectivity, a quantity which is closely correlated with particle size. Maximum mean values are found over the High Plains and Rocky Mountain regions of the U.S., suggesting that convection over that region tends to generate smaller anvil ice crystals than areas throughout much of the eastern U.S. To correct for preferred forward scattering by the cloud-top ice crystals, an effective radius retrieval using GOES is developed. Forward radiative transfer simulations are run for a wide range of cloud-top ice crystal sizes and sun-cloud-satellite scattering angles. The output is used to generate a lookup table, so that GOES-measured radiances may be used along with sun-satellite geometry to obtain an estimate for particle size. Validation of the retrieval shows that the assumed scattering properties perform quite well.

To help explain the geographical variation in cloud-top ice crystal size, a composite analysis is performed in the High Plains region by averaging environmental conditions for days which produced both small and large ice crystal storms. Small ice is found to occur with relatively high based storms and steep mid-level lapse rates. Additionally, observational evidence from a pyrocumulonimbus event is presented to show the effect of low-level cloud condensation nuclei (CCN) on cloud-top ice crystal size.

Model simulations using the Colorado State University Regional Atmospheric Modeling System (RAMS) are performed to help understand the physical mechanisms responsible for cloud-top ice crystal size. Through a series of sensitivity tests, it is found that larger low-level CCN concentrations lead to smaller anvil ice. In addition, as cloud-base temperature decreases (and cloud-base height increases), storm-top ice crystals get smaller. A weaker updraft strength is found to have very little effect on ice crystal size.

Daniel T. Lindsey
Department of Atmospheric Science
Colorado State University
Fort Collins, Colorado 80523-1372
Summer 2008

ACKNOWLEDGEMENTS

This research was supported by NOAA Grant number NA17RJ1228.

I want to thank my advisor, Dr. Richard Johnson, as well as committee members Drs. Dave Thompson, Chris Kummerow, Bogusz Bienkiewicz, and Mark DeMaria. I also want to thank NOAA for allowing me to pursue this research. A number of people contributed greatly to this research via lengthy conversations and email correspondence. A likely incomplete list of these individuals includes: Dr. Louie Grasso, Dr. Daniel Rosenfeld, Dr. Frank Evans, Dr. Andrew Heymsfield, Dr. Don Hillger, Dr. John Knaff, Jack Dostalek, Cindy Combs, Dr. Manajit Sengupta, Dr. Michael Fromm, and Dr. Martin Setvak, and Kathy Fryer. Finally, I want to thank my family and friends for continued moral support.

CONTENTS

FIGURES

TABLES

CHAPTER 1

INTRODUCTION

The generation of ice particles by thunderstorms is a topic which has received little attention in the literature. It is generally accepted that the ice which populates convective anvils is generated by both heterogeneous and homogeneous nucleation, but the details which determine the size of cloud-top ice crystals are largely lacking. Reasons why thunderstorm crystal size is important include 1) its radiative effects and resulting impact on the Earth's radiation budget, 2) a possible correlation with updraft strength, and 3) its role as a danger to aircraft. More information about each of these follows. The overall goal of this study is to determine which physical mechanisms play a part in determining thunderstorm-top ice crystal size.

Boudala et al. (2007) discuss how including the effects of small ice particles in general circulation models (GCMs) has notable effects on the Earth's radiation budget. Most GCMs do not predict ice particle size, but rather infer it from other predicted microphysical variables. It is therefore extremely important to understand those factors which affect cloud-top ice crystal size in convection. Some GCMs either set ice particle size as a constant, or parameterize it by simply using temperature: colder temperatures imply smaller crystals. This simple approximation demands investigation.

Rosenfeld and Lensky (1998) use satellite data to examine cloud-top particle size in growing cumulus clouds. They find that substantial differences exist between maritime and continental clouds, and as updraft magnitude increases, cloud particle growth with height is reduced. This implies that stronger storms may have smaller cloud-top ice crystals. Given that convective clouds change on time scales shorter than one hour, satellite retrievals of particle size would need to be performed using a geostationary satellite, which typically provides at least four images per hour. With an estimate of cloud-top particle size every fifteen minutes, the evolution of storm-top microphysics may be monitored, and a determination may be made whether particle size provides useful information about storm intensity.

Recent evidence suggests that convectively-generated ice crystals may be dangerous for aircraft (Rasumussen 2007, personal communication). There have been over 100 known events of aircraft engine power loss in the presence of high altitude ice (but no cloud liquid water and no radar returns). It is believed that the ice crystals damage the interiors of engines. More research is needed to understand exactly why these incidents occur, as well as whether ice crystal size and number concentration play a role.

In addition to thunderstorm updraft strength potentially having an effect on ice crystal size, a few other factors may play a role. These include aerosols and low-level thermodynamics. Previous research has shown that cloud condensation nuclei (CCN) can affect cloud droplet number and size, so perhaps when these droplets freeze, they maintain their relative size. Low-level thermodynamics had never been linked to ice crystal size until the work by Lindsey et al. (2006); results from this paper are presented in Chapters 3 and 5.1.

In order to investigate in detail these factors which influence thunderstorm-top ice crystal size, a number of methods will be employed. First, several years of geostationary satellite data will be used to generate maps of mean 3.9 μm reflectivity, which, as will be explained later, is a proxy for ice crystal size. This climatology analysis is found in

Chapter 3. In Chapter 4, an ice crystal particle size retrieval is developed and validated to remove the effects of sun angle. Chapter 5 uses a variety of methods to investigate the physical mechanisms responsible for cloud-top ice crystal size. These include a statistical composite analysis, some basic cloud droplet formation and growth theory, observations of storms forming near large wildfires, and some cloud model simulations. Chapter 2 contains some background information and Chapter 6 offers a brief summary and conclusions.

CHAPTER 2

BACKGROUND

Before beginning the investigation into convectively-generated ice crystals, a review of several topics is needed. In this study, extensive use is made of satellite observations, particularly a band in the shortwave infrared portion of the spectrum, so the background behind this remote sensing technique is explored below. Next, previous work related to effective radius retrievals is reviewed. Finally, we present a few papers which make a connection between CCN and convective cloud physics.

Satellite observations of thunderstorms have been widely documented since the launch of Geostationary Operational Environmental Satellites (GOES) in the 1970's. The primary advantages of GOES observations are high temporal resolution (~15 minutes) and complete coverage of the continental US. Current GOES spatial resolution is 1-4 km, which is sufficient for resolving most thunderstorm tops. A number of studies in the 1970's and 1980's assessed the utility of GOES to identify thunderstorms and infer their intensity and characteristics. Purdom (1973) observed meso-highs using satellite imagery, and later Purdom (1976) used GOES data to identify mesoscale features such as convective lines, sea breeze fronts, outflow boundaries, and storm mergers. Adler and Fenn (1979) used geostationary satellite data to calculate cloud-top cooling rates and storm structure, and compared their observations to severe storm reports. Infrared satellite imagery was used by Maddox (1981) to define and study Mesoscale Convective

Complexes (MCCs). One of the first studies looking at infrared cloud-top structure identified the enhanced-V (McCann 1983) as a possible severe storm indicator. This structure is characterized by the coldest portion of the thunderstorm top being shaped like a "V", with a warmer region downwind. He found that storms having an enhanced-V were often severe, but a minority of severe storms exhibited the enhanced-V structure, making the probability of detection rather low. Adler et al. (1985) used a number of infrared satellite indicators to form a thunderstorm index, then compared index values to observations of severe storms. All of these early studies focused on the visible (0.4 - 0.7 μm) and window infrared (10 - 11 μm) portion of the spectrum. The shortwave infrared (3 - 4 μm) portion of the spectrum was not yet available on a geostationary imager.

Observations in the shortwave infrared region were first available with the Advanced Very High Resolution Radiometer (AVHRR) aboard the TIROS N polar orbiter, launched in 1978 (Kidder and Vonder Haar 1995). AVHRR band 3 is centered at 3.7 μm. The first geostationary platform having a shortwave infrared band was the Visible and Infrared Spin Scan Radiometer (VISSR) Atmospheric Sounder (VAS) aboard GOES-4, which was launched in 1980. More recent GOES imagers, beginning with GOES-8 (launched in 1994), have a channel centered near 3.9 μm (band 2).

Liljas (1987) and Scorer (1987) first noted curious differences in AVHRR 3.7 μm radiances among thunderstorm tops. In order to further investigate this observation, Setvák and Doswell (1991) showed how one might calculate the reflected component of the measured 3.7 μm radiance. The AVHRR radiance at 3.7 μm can be split into two components:

$$R_{3.7} = R_{r_{3.7}} + \varepsilon_{3.7} R_{e_{3.7}}(T), \qquad (1)$$

where $R_{3.7}$ is the total radiance at the band centered at 3.7 μm, $R_{r_{3.7}}$ is the solar reflected component at 3.7 μm, $\varepsilon_{3.7}$ is the emissivity of the scene at 3.7 μm, and $R_{e_{3.7}}(T)$ is the blackbody radiance 3.7 μm with temperature *T*. The first term can be written as

$$R_{r_{3.7}} = \alpha_{3.7}[R_{e_{3.7}}(T_{sun})(\frac{A}{B})^2 \cos(\phi)], \tag{2}$$

where $\alpha_{3.7}$ is the 3.7 μm reflectivity, $R_{e_{3.7}}(T_{sun})$ is the blackbody radiance of the sun (T_{sun} is taken to be 5800 K), *A* is the radius of the sun, *B* is the average radius of Earth's orbit, and ϕ is the solar zenith angle. For simplicity, the quantity in brackets will be denoted *S*, or the solar flux at the top of the atmosphere. For a cloud of sufficient optical thickness, the transmissivity is approximately zero. This approximation, along with Kirchoff's Law, gives

$$\varepsilon_{3.7} + \alpha_{3.7} = 1. \tag{3}$$

Substituting Eqs. (2) and (3) into Eq. (1), the 3.7 μm reflectivity is given by

$$\alpha_{3.7} = \frac{R_{3.7} - R_{e_{3.7}}(T)}{S - R_{e_{3.7}}(T)}. \tag{4}$$

Setvák and Doswell (1991) calculated the 3.7 μm reflectivity of thunderstorms using AVHRR data, and found that some storms have larger values than others. They postulated that very strong updrafts may be ejecting tiny ice crystals to the upper portions of the storm, which would result in enhanced 3.7 μm reflectivity.

It is well documented that liquid water clouds are more effective reflectors of 3.5 - 4.0 μm radiation than ice water clouds (e.g., Turk et al. 1998). However, the majority of thunderstorm tops exist at temperatures well below -40 °C, meaning their composition is dominated by ice crystals. Differences in the size distributions of these ice crystals have an effect on 3.5 - 4.0 μm reflectivity. Past studies have shown that more numerous smaller crystals tend to be more effective reflectors at 3.7 μm (Melani et al. 2003a,b). In addition, Setvák et al. (2003) observed similar thunderstorm top reflectivity characteristics at 3.9 μm from GOES as at 3.7 μm from AVHRR. Examples of thunderstorms with relatively high and low 3.9 μm reflectivity are given in Figs. 1a and 1b, respectively. Values of 3.9 μm reflectivity for storms on the plains in Fig. 1a approach 15% (warmer colors), while values for most of the storms in Fig. 1b are less than 5% (cooler colors). Details on how 3.9 μm reflectivity is calculated with GOES-12 can be found in Chapter 3.

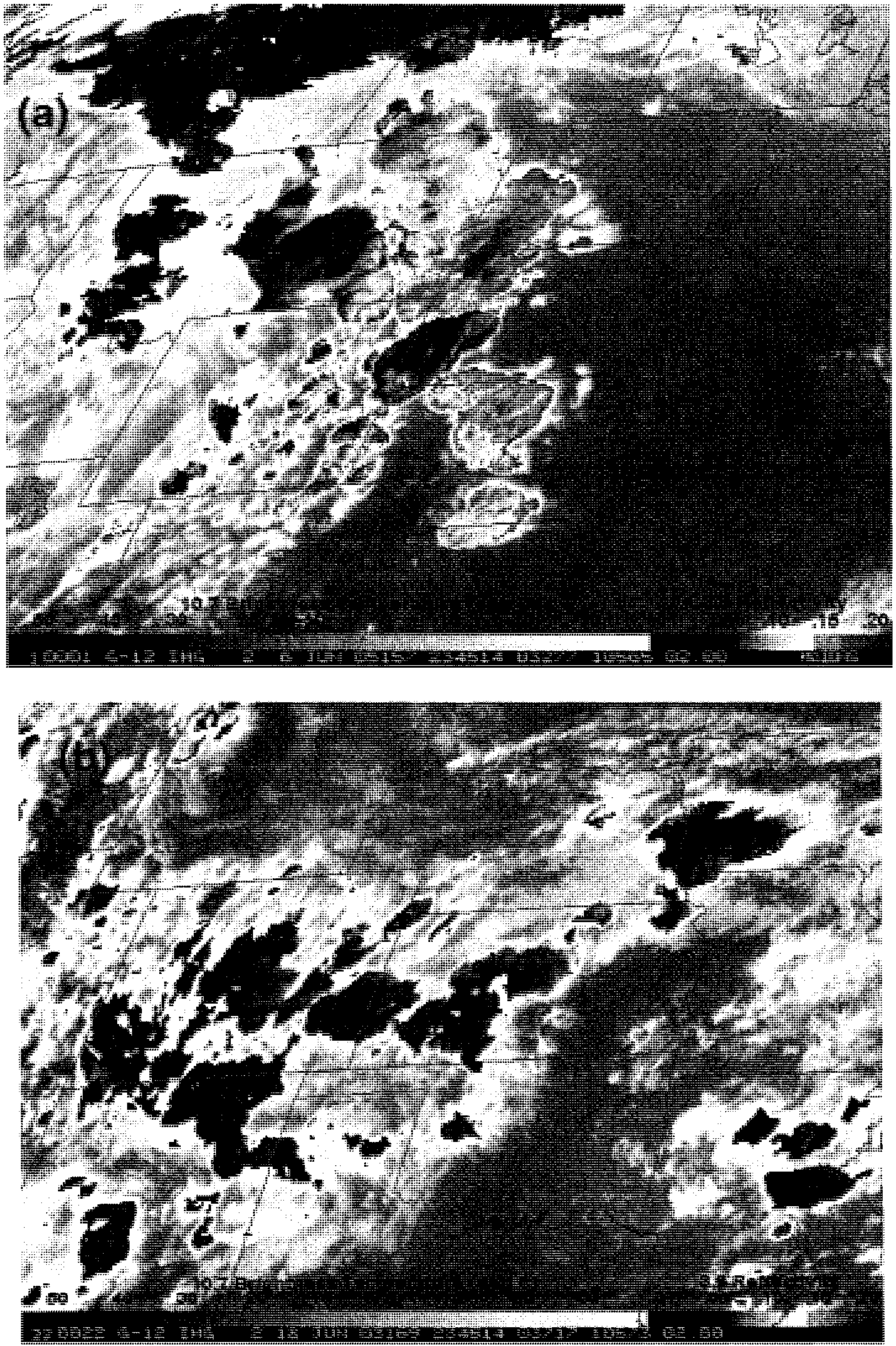

Figure 1: GOES-12 3.9 μm reflectivity for brightess temperatures less than -40° C (in colors), and 10.7 μm (gray shades) for brightness temperatures greater than -40° C, for a) 6 June 2005 at 2345 UTC, and b) 18 June 2003 at 2345 UTC. Warmer colors indicate cold cloud tops with larger 3.9 μm reflectivity values.

Variations in satellite-measured shortwave infrared reflectivity depend not only on the cloud-top microphysical composition, but also on the sun-cloud-satellite geometry (e.g., Nakajima and King 1990). However, if one knows the geometry, it is possible to use satellite-measured reflectivity to estimate certain cloud-top microphysical properties, such as optical depth and effective particle size. A large amount of literature has been devoted to these "microphysical retrievals" over the last 20 years or so. Note in Figs. 1a and 1b that the image time for both cases is 2345 UTC; this means that the sun-cloud-satellite geometry is approximately the same, so the reflectivity differences are likely due to other factors, such as cloud-top microphysics.

Nakajima and King (1990) introduced a method for determining optical thickness and effective radius from a band in the visible and a band in the shortwave infrared portion of the spectrum. They showed that visible reflectance varies mostly with optical thickness, while shortwave IR reflectance varies primarily with effective radius. For clouds having large optical thicknesses, effective radius can be determined with the shortwave IR band alone (e.g., Wetzel et al. 1996). This method works quite well with liquid water clouds due to the predictable scattering properties of cloud droplets, but ice clouds are much more complex due to differing habits and irregular crystal shapes. Minnis et al. (1993) introduced a satellite method to retrieve cirrus cloud properties using visible and IR radiances, but their primary goal was obtaining cloud altitude and optical depth, not particle size. McKague and Evans (2002) described a retrieval technique for various cloud parameters, including ice crystal size, using radiances from the GOES imager. Their method retrieves cloud parameter probability density functions, as opposed to pixel-by-pixel values, and is most useful for evaluating global climate model cloud parameterizations.

More recently, a number of studies have attempted to better document the scattering properties of non-spherical ice crystals (e.g., Yang et al. 2000; Yang et al. 2003, Yang et al. 2005). Baum et al. (2005a) use in situ data collected during a number of field experiments, along with the scattering properties of several ice crystal habits to develop a "recipe" for habit mixtures as a function of crystal size. This information can then be used to make forward model calculations of cloud radiative properties (e.g., Baum et al. 2005b), which in turn can be used to develop a satellite retrieval method. Cooper et al. (2006) perform an information content analysis to determine what combination of spectral measurements yield the best ice cloud effective radius retrieval.

Even with a successful retrieval of cloud-top particle size, the task remains to explain the physical connection between convective processes and cloud-top microphysics. There has been less treatment on this subject in the literature. As noted in Chapter 1, Rosenfeld and Lensky (1998) make a distinction between the vertical evolution of cloud droplet and ice crystal size in continental versus maritime clouds. They show that maritime clouds have a shallow mixed-phase region due to rapid coalescence and rainout. CCN are relatively scarce in oceanic regions, so the cloud droplets which form tend to be relatively large and collide efficiently with other droplets. Continental clouds have a much deeper mixed-phased zone and tend to glaciate at much colder temperatures.

Andreae et al. (2004) study the effect of smoke on convective cloud development. They conclude that aerosols from forest fires in the Amazon serve as CCN to downwind convective clouds, which have delayed precipitation onset due to the resulting small cloud droplets. More water mass is then passed into the anvils, and these clouds produce less rain than other more "pristine" clouds. They also claim that the delayed precipitation onset leads to more vigorous updrafts since additional latent heat of fusion is released aloft with more freezing cloud droplets.

In a recent paper by Rosenfeld et al. (2008), vertical profiles of effective radii are obtained by sampling (with satellite) growing cumulus clouds in various stages of development. The rate at which the effective radius increases with height is assumed to be correlated with updraft strength, so that a cloud field having stronger updrafts will have effective radii growing less rapidly with height. They then show that this satellite-derived proxy for updraft strength agrees fairly well with resulting tornado and hail reports in the central U.S. Although they focus on the effective radius retrieval in liquid water clouds, a result of their analysis is that stronger storms tend to have smaller anvil ice crystals. However, they are careful to point out that other factors may influence the particle sizes, namely, CCN and the depth of the cloud from base to the homogeneous freezing level. Both of these effects will be investigated in detail in Chapter 5.

CHAPTER 3

CLIMATOLOGY OF 3.9 μm REFLECTIVITY

In order to study the 3.9 μm reflectivity of ice clouds (and its evolution in time), it is first necessary to obtain a reasonable estimate of the quantity from GOES measurements. We therefore changed Equation (4) to reflect the shortwave infrared channel available on GOES, the 3.9 μm band. So Equation (4) becomes

$$\alpha_{3.9} = \frac{R_{3.9} - R_{e_{3.9}}(T)}{S - R_{e_{3.9}}(T)}\,. \tag{5}$$

To calculate $\alpha_{3.9}$, we estimate the 3.9 μm blackbody emitting temperature by using the observed 10.7 μm brightness temperature. This requires that the emissivity at 10.7 μm be unity, which for an optically thick cloud is a reasonable approximation (Stephens 1978). In addition, it is assumed that the reflected radiation is isotropic. A more thorough assessment of errors associated with these assumptions can be found in Chapter 4.

Using Eq. (5) and the observed solar zenith angle to compute S (Eq. (2)), $\alpha_{3.9}$ can be calculated at every ice cloud pixel within a GOES field of view. For the purposes of this study, an ice cloud pixel is defined as one in which the 10.7 μm brightness temperature is colder than -40 °C. This restriction eliminates thin cirrus, hopefully minimizes transmission from below, and ensures that all cloud tops are composed almost entirely of ice crystals. Eqs. (2) and (5) show that the 3.9 μm reflectivity calculation becomes undefined as the solar zenith angle approaches 90°, so only those pixels with a solar zenith angle less than 68° were included. This value was chosen by producing a scatterplot of observed 3.9 μm reflectivity versus solar zenith angle for a large number of pixels, and noting that all reflectivities begin to increase as the zenith angle exceeds 68°. This restriction excludes early morning, early evening, and overnight ice clouds from the analysis. An additional screen for optically thin clouds using the GOES visible channel will be added at a later portion of this study (Chapter 4), but for the purposes of the climatological analysis, this screen is not used. Figs 1a and 1b show two examples of the GOES-derived 3.9 μm reflectivity. Pixels having 10.7 μm brightness temperatures colder than -40 °C are colored based on their 3.9 μm reflectivity. In Fig. 1a, the storms in Western South Dakota have particularly large reflectivities (15-20%), but most of the storms in Fig. 1b have much lower values (< 5%). A large number of images of this type can be used to produce climatological mean values of 3.9 μm reflectivity.

Data from GOES-West, centered at 135°W longitude, and GOES-East, centered at 75°W longitude, were analyzed every 2 hours during 2000, 2003, and 2004. These three years were chosen because the data was continuous. Using Eq. (5), 3.9 μm reflectivity values were calculated at every ice cloud pixel within the domain for every month within the chosen period. Figs. 2a and 2b show the results of the GOES-West and GOES-East climatologies, respectively. Infrared pixels were grouped into 1° x 1° latitude/longitude boxes before calculating the mean reflectivity values; detail would be lost with the use of larger boxes, and the use of smaller boxes would introduce noise. All boxes over the U.S. contain at least 10^4 total pixels. Contours in Fig. 2 represent the mean 3.9 μm reflectivity of ice clouds. Over much of the eastern U.S., values are near 2%, while in the High Plains and the Rocky Mountain region, reflectivities are greater than 5%. The GOES-West climatology (Fig. 2a) shows generally larger values than in the eastern U.S., with maxima occurring in eastern Colorado, northwestern Montana, and eastern California. The longitudinal band between 110°W-95°W was viewed by both satellites, and GOES-East values are generally about 1% larger. Conversely, in the longitudinal band between 100°W-95°W, GOES-West values are about 1% larger. The result is a larger east-west gradient in mean reflectivity as viewed from GOES-East compared to GOES-West. This discrepancy will be investigated in more detail later in this chapter.

Since Fig. 2 represents all months of the year, the analyzed ice clouds may have been generated from convection, or they may be non-convective clouds, such as thick cirrus or mountain wave clouds. For example, in Eastern Colorado mountain wave clouds likely dominate the signal during the winter months, but convectively-generated ice clouds, including thunderstorm anvils, dominate during the summer. In order to focus on the convectively-generated clouds, we redo the climatology using only data from May, June, July, and August, and the result is shown in Fig. 3. Comparing the resulting mean values with those in Fig. 2, the general patterns are still present: largest values in the mountains and High Plains, with lower values further east. However, the value of the maximum in Eastern Colorado and Eastern New Mexico increases to over 6.5%. Conversely, the maximum in Western Montana is slightly lower during the summer months, suggesting that the wintertime mountain wave clouds there are more reflective than the summer ice clouds (likely a mix of both wave clouds and convectively-generated clouds). It is also noteworthy that the increase in the maximum values in Eastern Colorado is most notable from the GOES-East perspective (Fig. 2b and Fig. 3b).

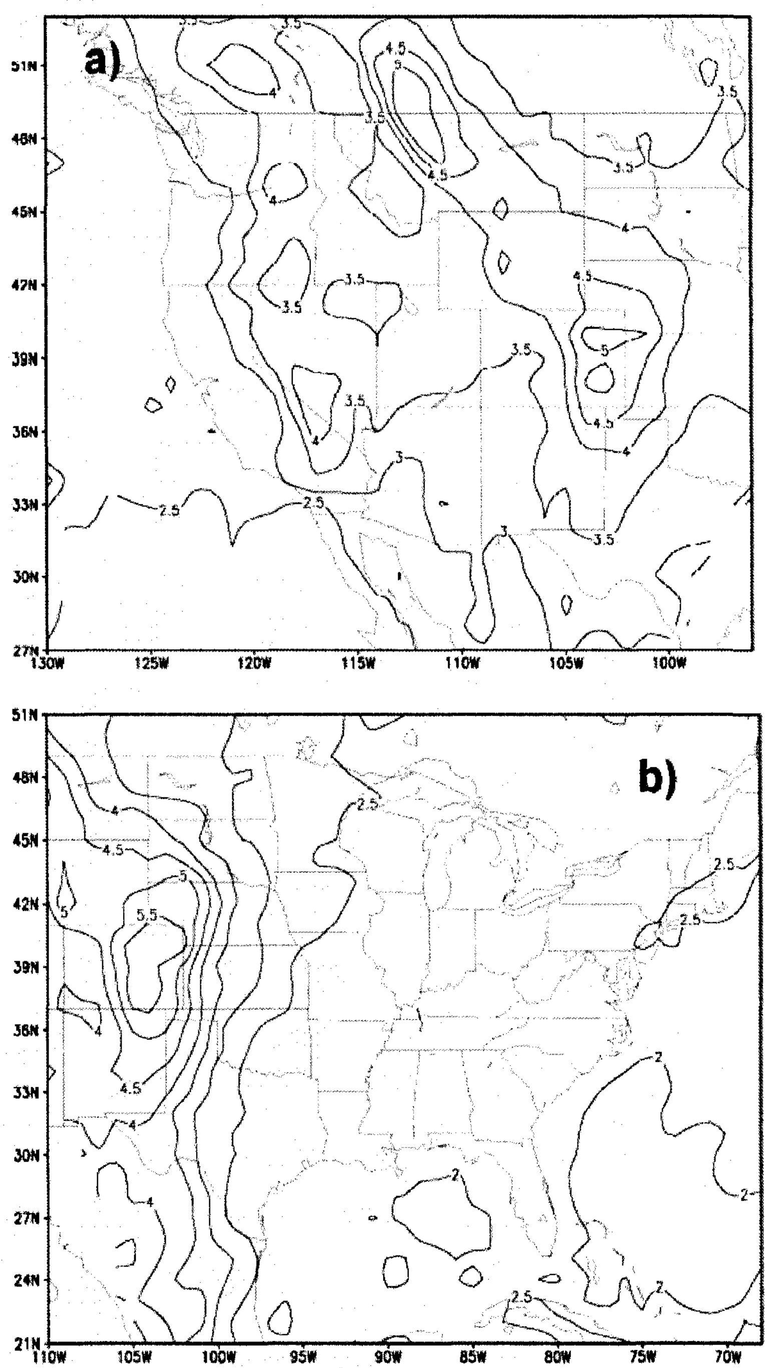

Figure 2: Mean 3.9 μm reflectivity (%) of ice clouds from a) GOES-West and b) GOES-East, during 2000, 2003, and 2004, when the solar zenith angle was less than 68°.

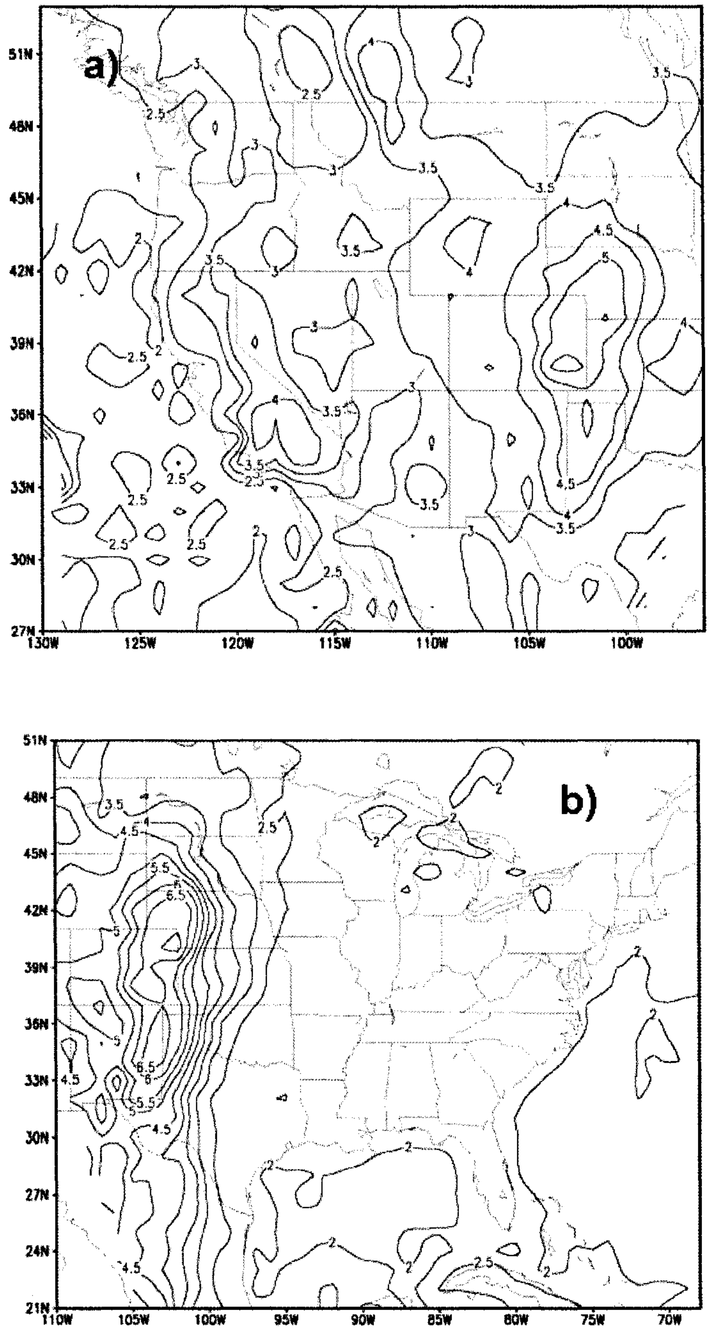

Figure 3: Mean 3.9 μm reflectivity (%) of ice clouds from a) GOES-West and b) GOES-East, from May, June, July and August of 2000, 2003, and 2004, when the solar zenith angle was less than 68°.

A slightly different way to investigate the larger 3.9 μm reflectivity values is to determine the percent of ice clouds whose reflectivity exceeds some value. We choose 5%, and the summertime results are given in Fig. 4. Differences between GOES-East and GOES-West are again evident, particularly in Wyoming, Colorado, and New Mexico. In the Eastern U.S., less than 10% of summertime pixels exceed 5%, but in Eastern Colorado, over 40% of these clouds have 3.9 μm reflectivities exceeding 5%. It should be noted that values in Southern California and particularly off the California coast have little meaning given the relative infrequency of summertime ice clouds there.

The climatological analyses presented up to this point include all ice cloud pixels having brightness temperatures less than -40 °C. There is a possibility that 3.9 μm reflectivity is a function of cloud-top temperature, so that colder clouds may have consistently larger or smaller values than warmer clouds. To check this, Fig. 5 shows maps of mean summertime 3.9 μm reflectivity using only clouds whose brightness temperatures are between -40 °C and -50 °C. Comparing the results in Fig. 5 to those in Fig. 3, it can be seen that excluding the coldest clouds (Fig. 5) indeed results in lower mean 3.9 μm reflectivities, particularly in Eastern Colorado and Eastern New Mexico. A closer look at Eq. (5) shows that $R_{e_{3.9}}(T)$ would be lower for colder clouds, and this would indeed increase the 3.9 μm reflectivity. However, for clouds colder than -40 °C, the magnitude of $R_{e_{3.9}}(T)$ is small compared to the total radiance. Plugging some sample numbers into Eq. (5), a cloud with a 10.7 μm brightness temperature of -70 °C should have a 3.9 μm reflectivity approximately 0.7% larger than a cloud whose 10.7 μm brightness temperature is -40 °C (everything else being equal). But the maximum over Eastern Colorado is 2% larger in Fig. 3 compared to Fig. 5, which means something else is causing the colder clouds to have larger 3.9 μm reflectivities than the warmer clouds. As will be shown later, the colder clouds are likely composed of smaller ice crystals, which serve to increase the cloud's 3.9 μm reflectivity.

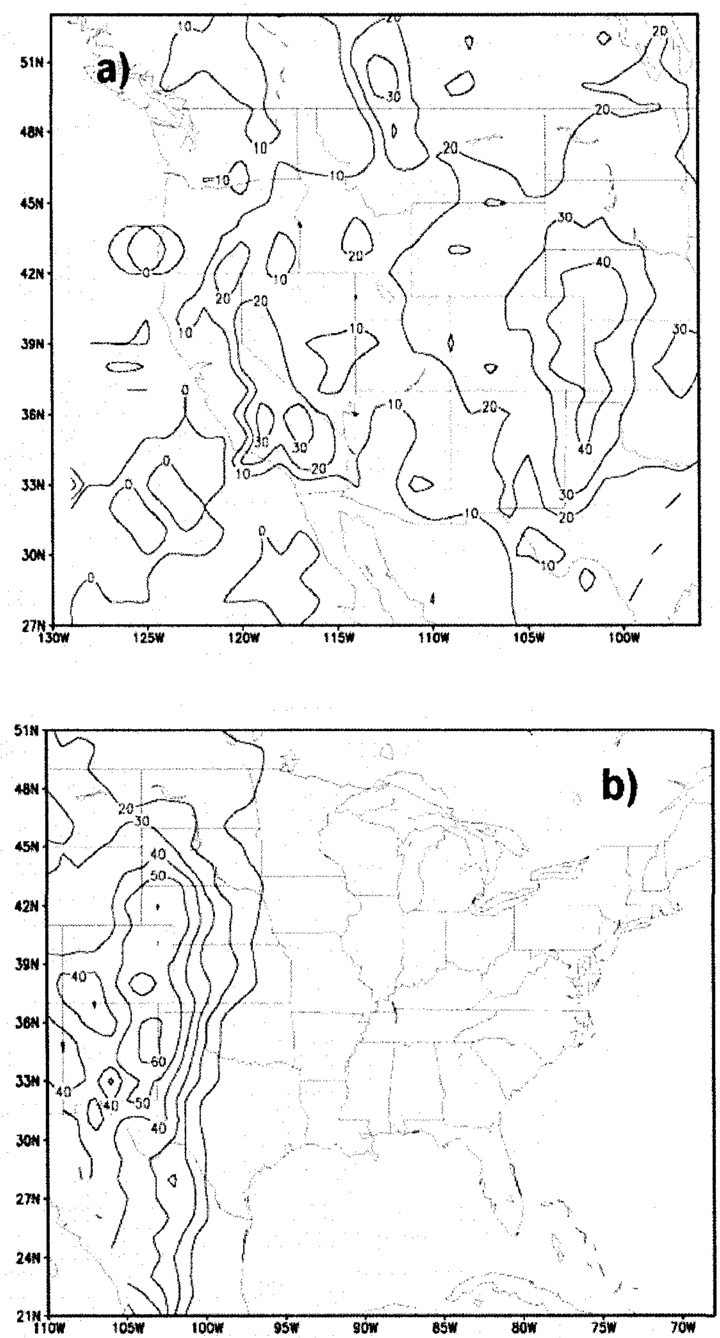

Figure 4: Percent of ice clouds whose 3.9 μm reflectivity exceeds 5% from a) GOES-West and b) GOES-East, during May, June, July, and August of 2000, 2003, and 2004, for times when the solar zenith angle is less than 68°.

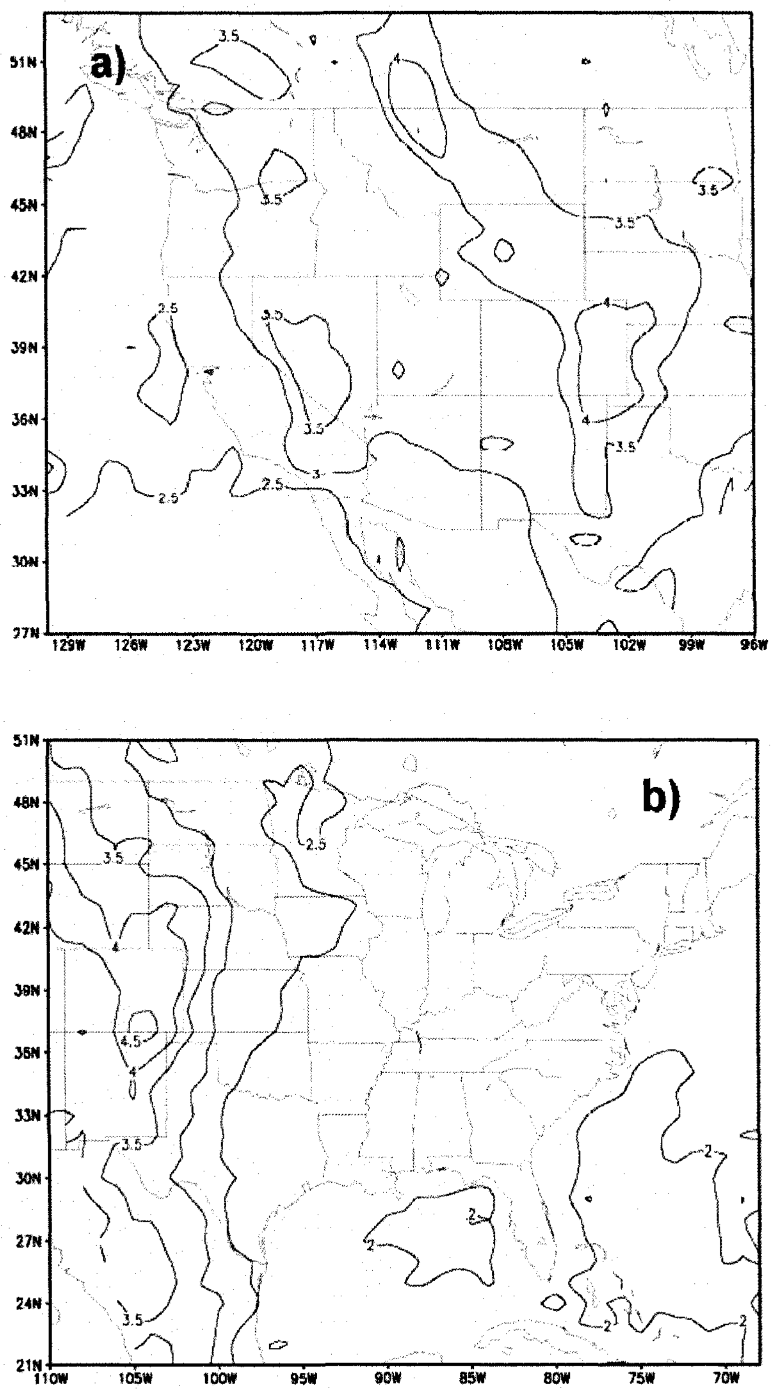

Figure 5: Mean 3.9 μm reflectivity of ice clouds from a) GOES-West and b) GOES-East, from May, June, July and August of 2000, 2003, and 2004, for clouds whose 10.7 μm brightness temperature is between 223 - 233 K, when the solar zenith angle was less than 68°.

Fig. 6 shows the monthly distribution of percent of ice clouds having greater than 5% 3.9 μm reflectivity from September 2003 to August 2004 for 3 longitudinal bands in the Continental U.S. The locations of the 3 bands can be seen in Figs. 2-5. Several things stand out from this graph. First, large values of 3.9 μm reflectivity occur much more frequently in the westernmost band, but this has already been shown in Fig. 4. In the westernmost band, there are 2 distinct peaks: one in November-January, the other in May-August. As has already been suggested, these peaks are likely associated with mountain wave cloud activity and convection, respectively. In the two eastern longitudinal bands, there are no distinct peaks, other than the value going to near zero during the summer months. This is an interesting result which will be discussed in more detail later.

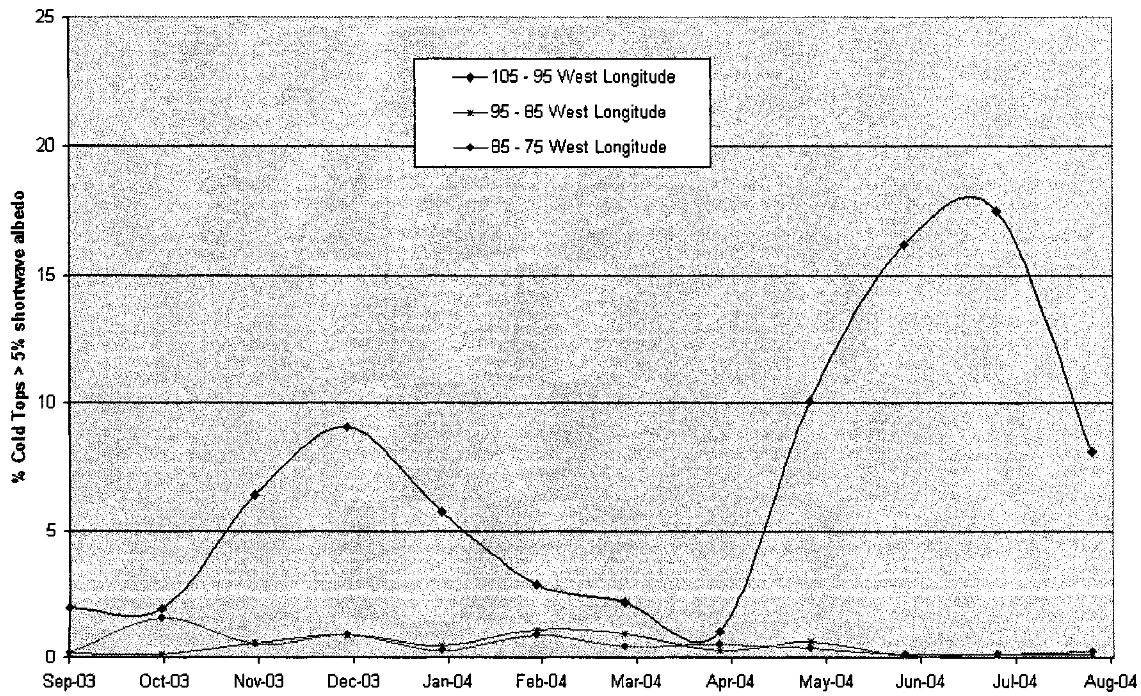

Figure 6: Monthly percent of ice clouds having greater than 5% 3.9 μm reflectivity from September 2003 to August 2004, for 3 longitudinal bands in the Continental U.S.

A histogram showing the distributions of 3.9 μm reflectivity for 4 longitudinal bands is shown in Fig. 7. Note that these longitudinal bands are slightly different from those in Fig. 6. The westernmost band, which corresponds with the largest climatological values of 3.9 μm reflectivity (Fig. 2), has a "flatter" distribution than the other 3 bands. The peak occurs in the 2-3% range, and there's a long tail of possible values out past 10%. For the more eastern bands, the peak occurs in the 1-2% range, and there are virtually no observations greater than 10%. These results are consistent with those in Fig. 2, and show that the High Plains and Rocky Mountain regions have consistently larger 3.9 μm reflectivities that areas further east.

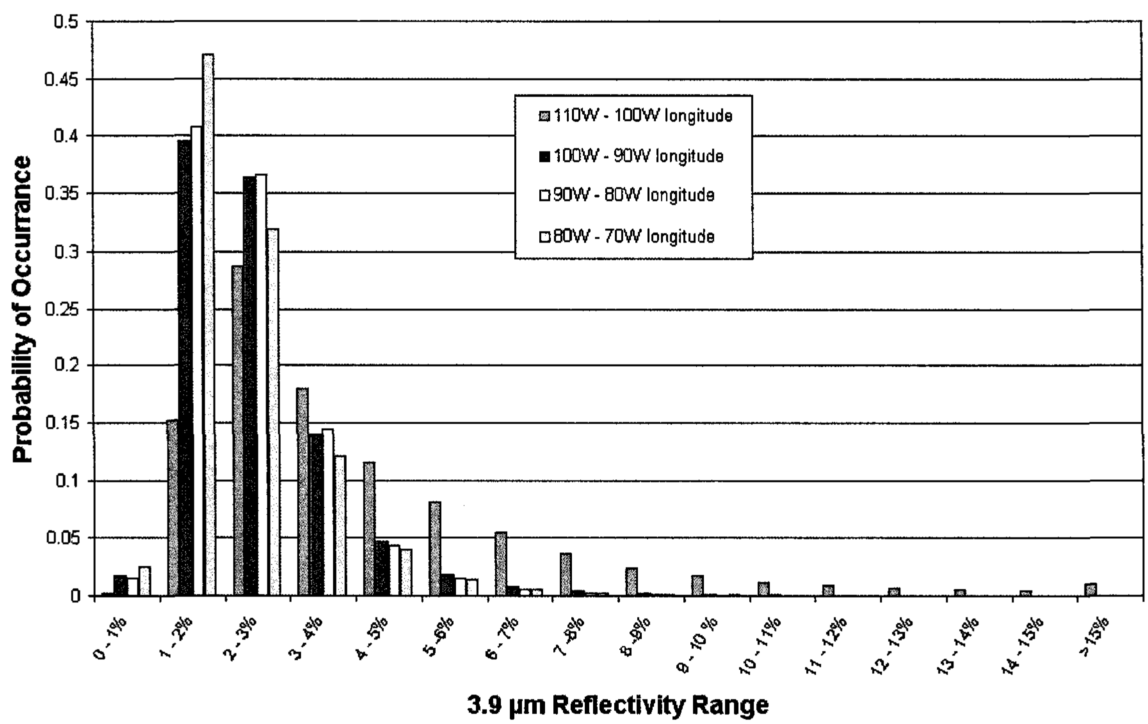

Figure 7: Histogram of 3.9 μm reflectivity from September 2003 to August 2004, for 4 longitudinal bands in the Continental U.S.

As mentioned above, a curious result of these climatological maps is the difference in mean values over parts of the domain as viewed from GOES-East and GOES-West. For example, in Fig. 3 the maximum mean value is near 6.5% in eastern Colorado and eastern New Mexico as viewed from GOES-East, but from GOES-West those areas have values between 4.5-5%. Oppositely, the values in eastern Kansas are actually *lower* as viewed from GOES-East compared to GOES-West. One possible explanation for these differences is that the scattering of the incoming solar radiation is actually *not* isotropic.

To investigate this difference between GOES-East and GOES-West 3.9 μm reflectivity, a day was chosen which had ice clouds in the longitudinal band covered by both satellites in both the morning and afternoon (26 June 2004). Ice cloud pixels viewed by both satellites at approximately the same time were selected, and their 3.9 μm reflectivities were calculated. Table 1 shows the means and standard deviations for various times throughout the day, and the associated reflection angles between the sun and satellite for each pixel. The reflection angles varied slightly with location at a given time, so the mean angles are displayed in the table. Note that in the late afternoon (2345 UTC), 3.9 μm reflectivities are maximized, and GOES-East measures over 3% greater values than GOES-West. At this time, the GOES-East reflection angle is 105° compared to 46° with GOES-West. GOES-East is therefore in a position to measure more forward-scattered radiation than GOES-West, so forward scattering appears to be favored. Earlier in the day, as the reflection angles become closer together, the differences in 3.9 μm reflectivities also decrease. In the morning, reflectivities measured from GOES-West exceed those from GOES-East, but due to a lack of vigorous convection, the absolute values are quite low. This analysis suggests that forward scattering is always preferred, and is maximized for large reflection angles.

Table 1. Mean 3.9 μm reflectivities from GOES-East and GOES-West for different times and reflection angles from 26 June 2004.

Time (UTC)	G-E Refl. Angle (deg)	G-W Refl. Angle (deg)	G-E 3.9 μm Mean Refl. (Std. Dev.)	G-W 3.9 μm Mean Refl. (Std. Dev.)
2345	105	46	7.30 (2.37)	4.00 (1.56)
2315	99	41	5.86 (2.19)	3.98 (1.75)
2245	92	36	4.57 (1.80)	3.75 (1.83)
2215	85	32	3.89 (1.64)	3.73 (2.02)
2045	65	30	2.58 (1.02)	3.05 (1.63)
2015	59	33	2.50 (0.96)	2.92 (1.49)
1945	52	37	2.13 (0.87)	2.38 (1.28)
1915	46	42	2.23 (1.11)	2.20 (1.14)
1845	41	47	2.13 (1.23)	2.05 (1.09)
1745	32	60	1.66 (0.91)	1.70 (0.60)
1715	29	66	1.88 (0.25)	2.08 (0.41)
1645	29	73	1.87 (0.24)	2.34 (0.21)
1615	30	80	1.91 (0.26)	2.41 (0.22)

Fig. 8 shows the diurnal trend in ice cloud pixel frequency for two longitudinal bands. In the morning, ice clouds are much more frequent in the eastern band. These clouds are likely associated with the remnants of nocturnal convective systems which often exist in the Central Plains shortly after sunrise. The western band shows a distinct afternoon maximum in convective ice clouds. The apparent drop-off in ice cloud frequency in the eastern band at 2345 UTC is primarily an artifact of the 68° zenith angle requirement; many areas in this band have zenith angles greater than 68° at 2345 UTC, so those pixels are not included in the analysis, as explained above. Results from Table 1 combined with Fig. 3 explain the differences in 3.9 μm reflectivity as measured from GOES-East and GOES-West. Since forward scattering is preferred, and GOES-East is in a position to measure more forward-scattered radiation during the peak in ice cloud frequency in late afternoon, mean values are higher from GOES-East in the longitudinal band between 105° - 100° W. In the eastern band, morning ice clouds are quite frequent, during which GOES-West measures more forward-scattered radiation, making these mean values larger than from GOES-West. These results are consistent with similar findings by Setvák et al. (2003) and show that the scattering is not isotropic. One method to correct for this preferential forward scattering is to perform a particle size retrieval, which takes into account the angle between the incoming solar radiation, the cloud, and the satellite. This is the subject of Chapter 4.

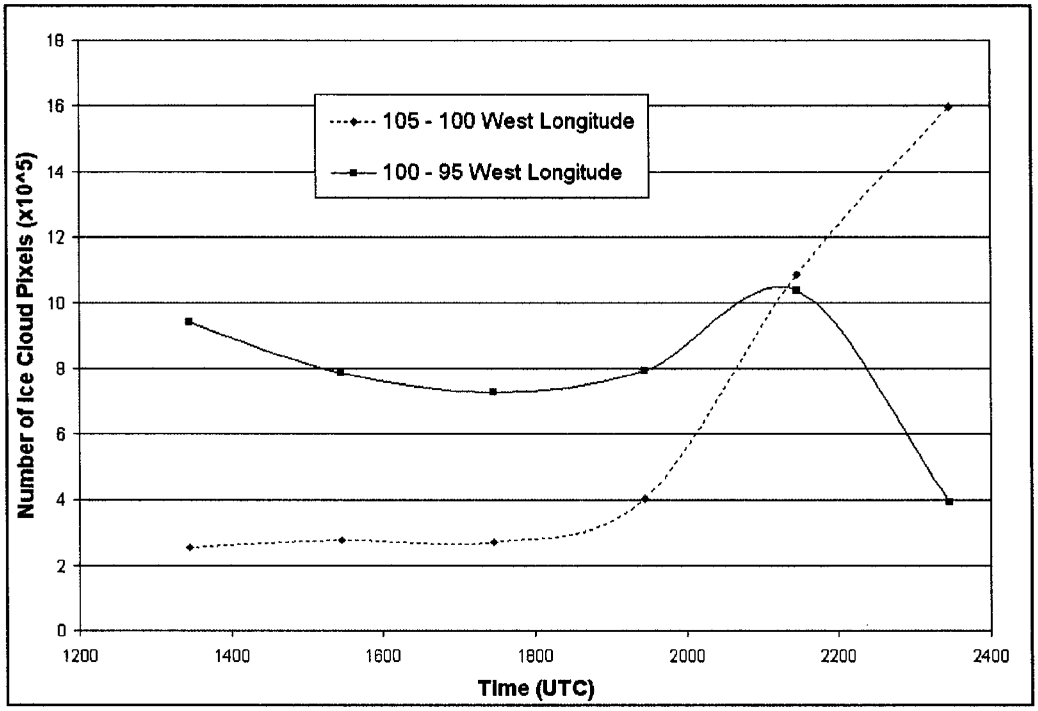

Figure 8. Diurnal trend in ice cloud pixels used in the analysis from Fig. 3, for the longitudinal bands 105° - 100° W and 100° - 95° W, from GOES-East.

CHAPTER 4

ICE CLOUD EFFECTIVE RADIUS RETRIEVAL

In Chapter 3, we determined that incoming solar radiation at 3.9 μm reflected by clouds does not scatter equally in all directions. In particular, forward scattering appears to be preferred. If the goal in measuring storm-top 3.9 μm reflectivity is to monitor the lifecycle of the storm, variations in the measurement attributable to solar geometry need to be corrected. Research such as conducted by Yang et al. (2000) and Baum et al. (2005a) allows for reasonably accurate predictions of ice cloud scattering properties. Using an observational operator, these properties can be used to develop a particle size retrieval which implicitly corrects for the forward scattering preference. Much of the forthcoming information in this chapter can also be found in Lindsey and Grasso (2008).

4.1 The forward model

The observational operator (Greenwald et al. 2002; Grasso and Greenwald 2004) used for the forward model calculations makes use of the plane-parallel version of the Spherical Harmonic Discrete Ordinate Method (SHDOM, Evans 1998), subsequently referred to as SHDOMPP. A homogeneous cloud composed of ice crystals is placed in the upper troposphere, so that its top is near -53 °C, the tropopause temperature in the assumed background sounding. As a test, the cloud top height was varied between -40 and -60 °C, but the 3.9 μm reflectivities calculated by the model were insensitive to its location. Further details of the assumed background sounding are not discussed here since gaseous absorption is very limited above the cold clouds tops, even though absorption by gases is explicitly calculated in the model. Following the results from Baum et al. (2005a), the following mixture of ice crystal habits is assumed: $D_{max} < 60$ μm is 100% droxtals; $60 < D_{max} < 1000$ μm is 15% three-dimensional bullet rosettes, 50% solid columns, and 35% plates; $1000 < D_{max} < 2000$ μm is 45% hollow columns, 45% solid columns, and 10% aggregates; $D_{max} > 2000$ μm is 97% three-dimensional bullet rosettes and 3% aggregates, where D_{max} is the particle maximum dimension. For each calculation, we assume a Gamma size distribution of the form

$$N(D) = AD^{\alpha} e^{-bD}, \tag{5}$$

where D is the equivalent volume spherical diameter, α is the shape parameter, and b is adjusted iteratively to achieve a desired effective radius. The shape parameter was chosen to be 1; a sensitivity analysis of this choice is forthcoming. Following Yang et al. (2000), effective radius (r_e) is defined as

$$r_e = \frac{3}{4} \frac{\int_{D_{MIN}}^{D_{MAX}} V(D)N(D)dD}{\int_{D_{MIN}}^{D_{MAX}} A(D)N(D)dD}, \tag{6}$$

where $V(D)$ is the ice crystal volume and $A(D)$ is the crystal projected area. For a chosen effective radius, we use the habit mixture described above to obtain the cloud's net optical properties, namely, extinction, single scattering albedo, and scattering phase function (which is represented with a Legendre polynomial series having 2500 terms) by weighting these optical properties based on the appropriate habit mixture. Note that a distribution having an effective radius of, say, 24 μm will include crystals having a maximum dimension up to ~ 200 μm (Fig. 9, top axis), so it would include droxtals, 3-dimensional bullet rosettes, solid columns, and plates. Optical properties for these habits were obtained from Yang et al. (2005) by averaging over the spectral range of the GOES 3.9 μm band (3.78 - 4.03 μm). To handle the forward scattering peak, the phase functions have been modified by convolving the portions with scattering angles less than 10° by a gaussian with 0.25° root mean square width, and by adjusting the forward peak height to normalize each phase function. The extinction efficiency, single scattering albedo, and asymmetry parameter were then delta rescaled to maintain consistency. These optical properties were used along with solar geometry information (solar zenith angle and scattering angle) by SHDOMPP to calculate the expected satellite radiance for the GOES 3.9 μm band. The 10.7 μm brightness temperature is also calculated, so that 3.9 μm reflectivity ($\alpha_{3.9}$) can be determined using Eq. (4).

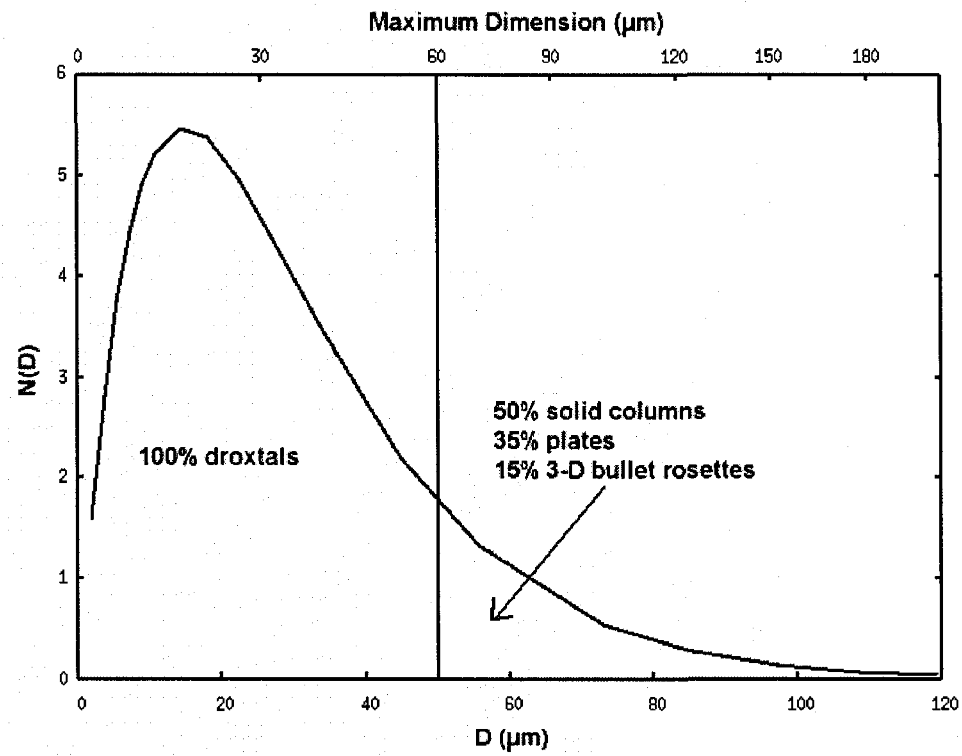

Figure 9. Example Gamma distribution for an effective radius of 24 μm. The axis on the bottom is equivalent volume spherical diameter (D); the axis on the top is ice crystal maximum dimension (D_{max}). The vertical line at D_{max} = 60 μm represents the cutoff between the particle mixtures described in the text.

Note that a GOES retrieval of $\alpha_{3.9}$ requires that the cloud optical depth be sufficiently large to prevent transmission of 3.9 μm radiation from below. Therefore, we limit our retrieval to pixels whose 10.7 μm brightness temperature is colder than -40 °C, minimizing cloud transmissivity. An additional requirement is enforced to screen for optically thin clouds: the GOES visible channel (0.65 μm) reflectance must exceed a critical value. In order to obtain a consistent visible reflectance from each satellite, GOES sensor degradation must be taken into account. A correction obtained from the National Environmental Satellite Data and Information Service (NESDIS) was applied to GOES-10 (formerly GOES-West) and GOES-12 (currently GOES-East) radiances. A similar correction is not currently known for GOES-11 (currently GOES-West), so we calculated the mean visible reflectance for all pixels colder than -40 °C from July 2006, then determined a correction factor (1.12) to force the mean value to match the GOES-12 mean value; this factor was then applied to all GOES-11 visible reflectances. Finally, each visible reflectance was divided by the cosine of the solar zenith angle in order to approximate a reflectance value if the sun were directly overhead. The critical value of visible reflectance for sufficient optical depth was chosen to be 0.60. This value maximized the statistical measures described later in this chapter.

In order to determine the model's sensitivity to optical depth, $\alpha_{3.9}$ was calculated for a wide range of cloud optical depths for distributions having 4 effective radii; the result is given in Fig. 10. For 3.9 μm optical depths greater than 20, $\alpha_{3.9}$ changes very little in every distribution. This means the cloud is sufficiently optically thick to prevent transmission from below, ensuring that the model-calculated $\alpha_{3.9}$ is accurate. For the series of model runs described below, the cloud optical depth was chosen to be greater than 20 for every simulation.

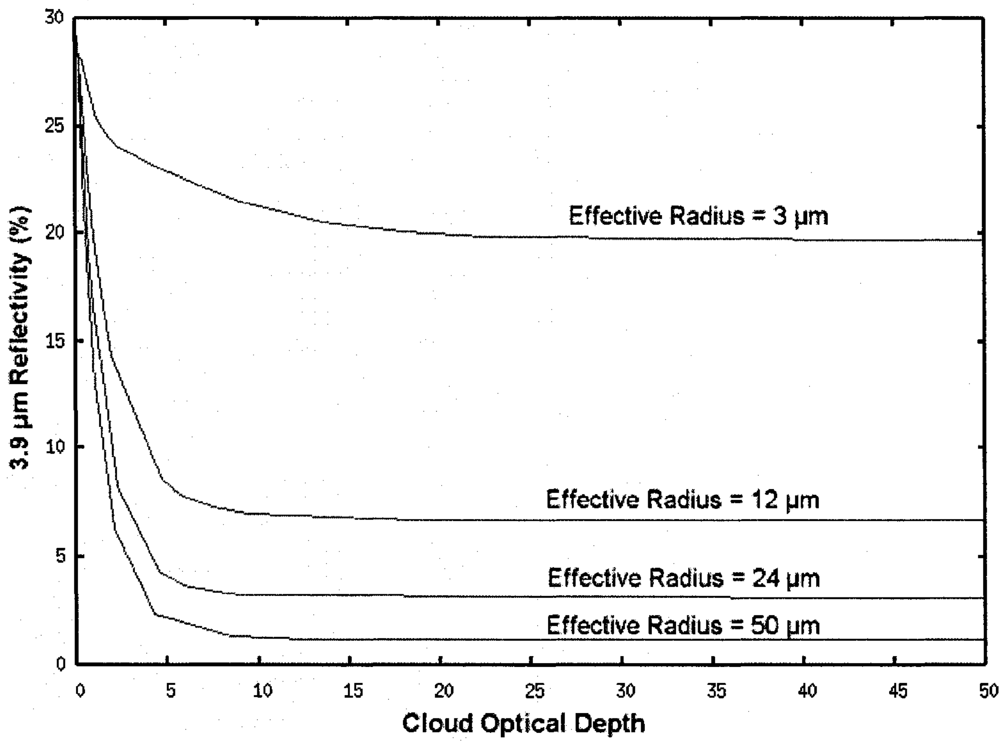

Figure 10. Forward model calculations of 3.9 μm reflectivity as effective radius and cloud 3.9 μm optical depth are varied. A solar zenith angle of 17° and a scattering angle of 136° have been assumed.

A total of 1377 model runs were performed, in which effective radius was varied between 3 and 51 μm, and the solar zenith and scattering angles were varied to account for the most extreme values given the locations of the current GOES. In order to vary the effective radius, ice mass and number concentration were changed, but as noted above the optical depth was forced to exceed 20 in every run. Each model result was used to populate a lookup table, so that GOES 3.9 μm reflectivity measurements can be used along with solar and satellite geometry to unambiguously determine optically thick ice cloud effective radius values. The lookup table is comprised of 27 unique effective radii, and for each one, 51 different times/locations so that the scattering angle varies from 57°-180°, and the solar zenith angle from 1° - 79°. A scattering angle of 57° represents approximately the smallest possible value given the locations of GOES-East (75° W longitude), and GOES-West (135° W longitude). For observed scattering angles/zenith angles/3.9 μm reflectivities falling between those in the lookup table, linear interpolation is used to obtain an effective radius value. An example of this product is provided in Fig. 11. Thunderstorms in western Nebraska have significantly smaller effective radii than those in central Iowa; reasons for these differences are discussed later in this manuscript. Note the missing values near the core of the southernmost thunderstorm in western Nebraska (white pixels surrounded by blue); these pixels were screened out by the visible reflectance requirement. Although actual optical depths are likely quite large here, this area is in the shadow of a significant overshooting dome, so visible reflectances are quite small. We feel that including the visible channel thin cloud screen provides a necessary and important improvement to the retrieval, especially since the relative occurrence of shadowed areas is small. In addition, areas with shadows also have anomalously low 3.9 μm reflectivities, which results in an effective radius estimate which is too large, so screening out these areas may actually be beneficial.

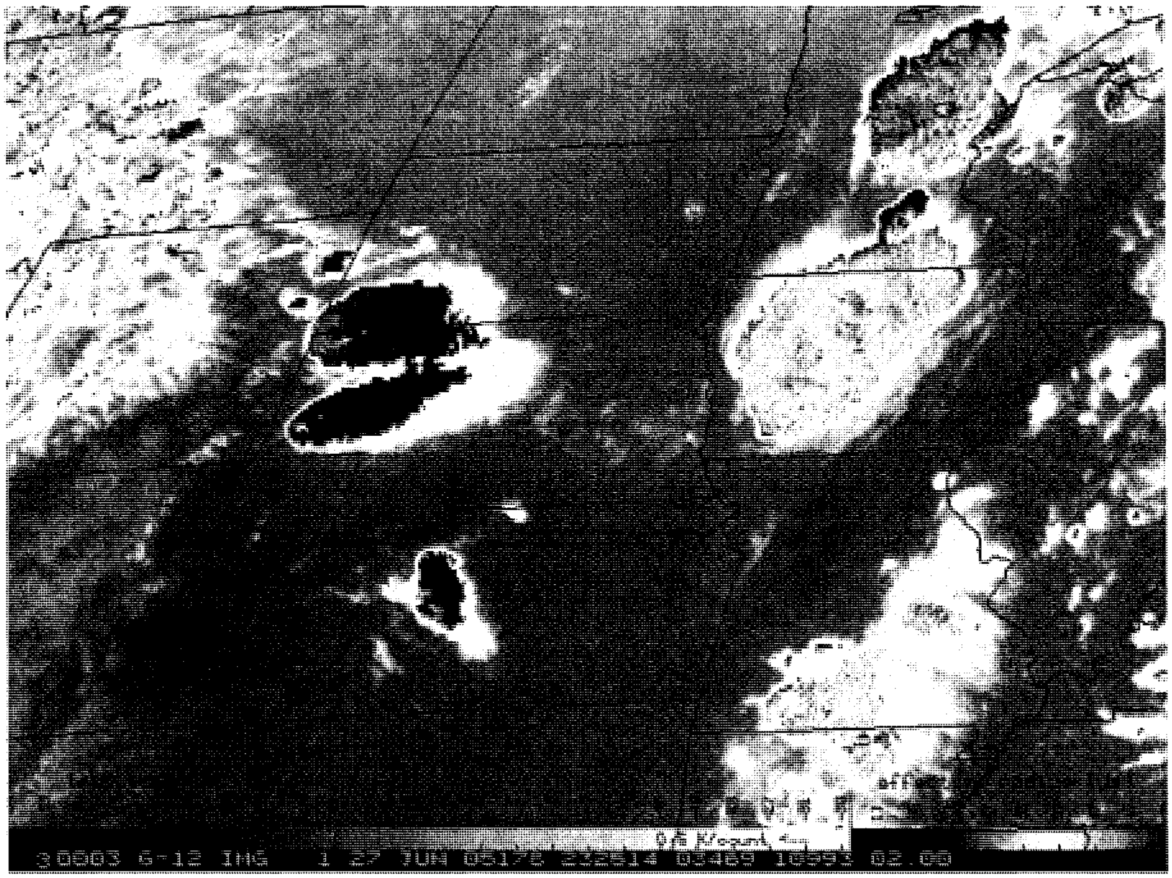

Figure 11. GOES-12 retrieval of effective radius for 10.7 μm brightness temperatures colder than -40 °C (colors), and 10.7 μm brightness temperatures for warmer values (grayscale). Pixels colder than -40 °C but with corrected visible reflectances less than 0.60 are forced to be white.

4.2 Retrieval Error Analysis

Validation of an ice cloud effective radius retrieval is extremely difficult for several reasons. In-situ aircraft observations of cirrus clouds are rare, and those which do exist often have measurement errors associated with them. In addition, remotely-sensed cloud properties provide information about a pixel-sized average cloud area, while aircraft typically fly at a single altitude directly through a cloud. In other words, the aircraft's observations may not be representative of what the satellite detects. Possible sources of error in this retrieval include (but are not limited to) 1) an incorrect estimate of 3.9 μm reflectivity from GOES due to transmission from below or instrument noise, 2) three-dimensional scattering effects due to cloud heterogeneity, 3) the existence of a non-Gamma size distribution, 4) incorrect habit mixture assumptions, and 5) imperfect scattering properties of each habit. We rely on the results of Baum et al. (2005a), who use all available observational results to prescribe the ice crystal habit mixture discussed above, to hopefully minimize some of these errors. Instead of direct comparison with observations, we will employ a number of indirect methods to estimate the retrieval error.

4.2.1 GOES Imager Instrument Noise

Studies of the GOES imager noise levels indicate a 3.9 μm radiance error of +/- 0.008 $mWm^{-2}sr^{-1}cm$ (Hillger et al. 2003). Using this value with Eq. (5), we find the maximum corresponding 3.9 μm reflectivity error to be +/- 0.45% (at a solar zenith angle of 67°, the largest allowed value in the retrieval). Fig. 12a shows the forward model results using a solar zenith angle of 67° and a scattering angle of 131°. Scattering angle is defined as the angle formed between incoming solar radiation, a cloud, and the GOES satellite; 0° is in the forward direction, 180° backward. As shown in Fig. 12a, a 0.45% 3.9 μm reflectivity error leads to only a 0.5 μm effective radius error near 10 μm, but the signal deteriorates for larger effective radii, leading to an error near 10 μm for values near 45 μm. These results suggest that our retrieval is much more accurate for clouds with relatively small effective radii. Fig. 12b shows the same curve as in Fig. 12a, along with two additional curves having different solar zenith and scattering angles. Each curve represents a different time at 30° N. latitude, 105° W. longitude on Julian Day 173. Notice that all three curves begin to flatten out at large effective radii, suggesting that the relatively large retrieval error should be expected for all locations and times of day.

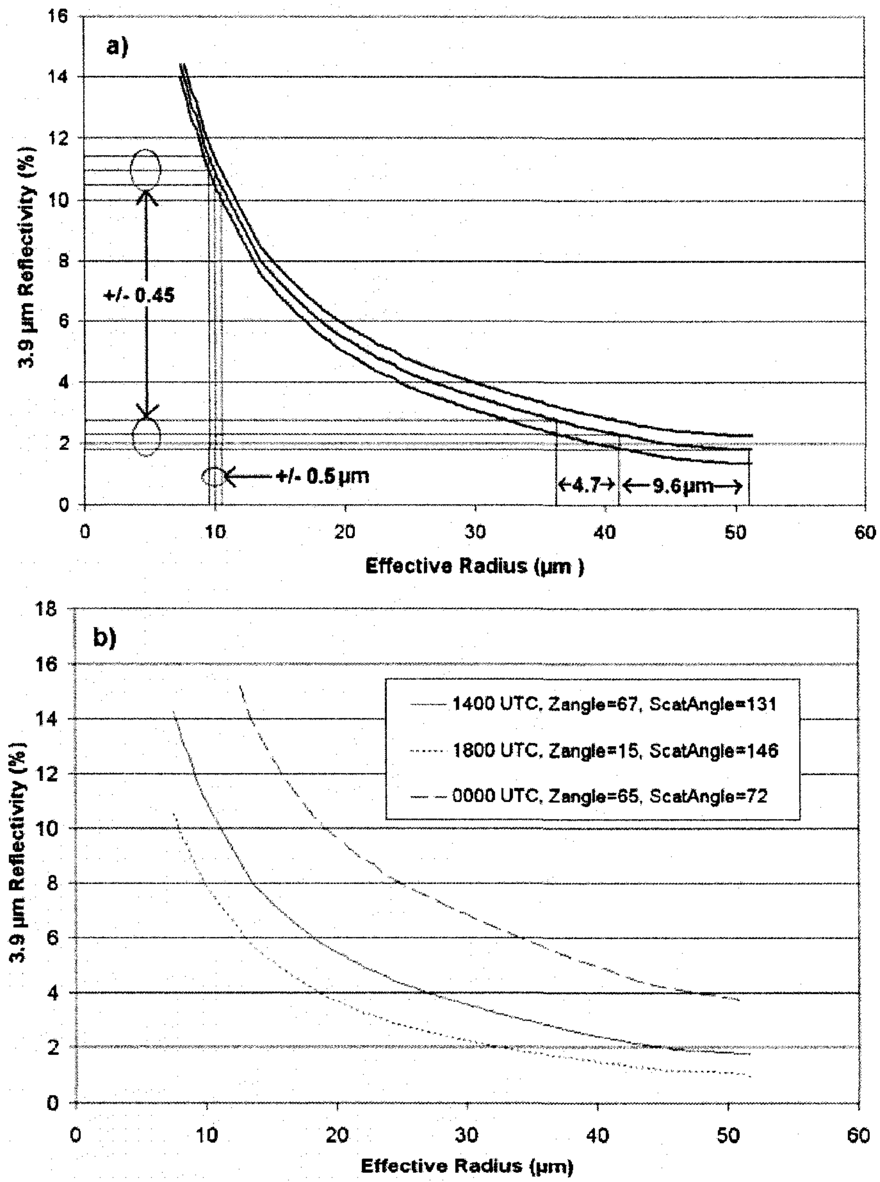

Figure 12. Forward model results showing a) the effect of a 0.45% 3.9 µm reflectivity error on the effective radius retrieval at 10 µm and 41 µm, and b) the relationship between effective radius and 3.9 µm reflectivity for three times at Julian Day 173 for a location at 30° N. latitude, 105° W. longitude.

4.2.2 Comparison with MODIS

Due to its horizontal resolution (1 km) and additional spectral bands, the Moderate Resolution Imaging Spectroradiometer (MODIS) instrument aboard the Aqua and Terra polar-orbiters should be superior to GOES in retrieving cloud particle effective radius. It will therefore make a good basis for comparison. King et al. (2003) describe the MODIS effective radius retrieval algorithm used in the MODIS Level 2 Cloud Product. The most recent version of the Cloud Product (Collection 5) uses the exact same ice crystal habit assumptions as we employ (Yang et al. 2007), but the forward model used to generate the ice lookup tables is different (Discrete Ordinates Radiative Transfer model, DISORT, Stamnes et al. 1988). Additionally, gaseous absorption is neglected with the MODIS scheme in DISORT, but not in SHDOMPP. In the comparisons below, the MODIS effective radius was retrieved using Band 7 (2.13 μm) and one of three possible non-absorbing bands (Band 1 (0.645 μm), Band 2 (0.858 μm), or Band 5 (1.24 μm)). Absorption will be less with MODIS Band 7 than with the GOES 3.9 μm band, particularly for the larger ice crystals (Platnick et al. 2003), so signal saturation at large effective radii should be minimal compared to GOES.

Eleven days from May and June of 2005, 2006, and 2007 were chosen in which at least one MODIS pass corresponded with a GOES scan over active deep convection in the continental U.S. On two of the chosen days, two MODIS passes were selected, making a total of thirteen MODIS passes for this analysis. Twelve of the thirteen MODIS passes were by Aqua, the other by Terra. This is because Aqua passes over the Continental U.S. latest each afternoon, increasing the chances that convection has begun.

For each GOES scene, an algorithm was used to identify individual ice clouds (adjacent pixels having 10.7 μm brightness temperatures colder than -40 °C and visible reflectance greater than 0.60), and each GOES pixel was matched (via latitude and longitude) with a corresponding array of the 25 (the approximate number encompassing one GOES pixel at this latitude) nearest MODIS 1-km pixels. Effective radius values were averaged from these 25 MODIS pixels. It is quite rare for a MODIS scan time to match exactly with a GOES scan time at a given pixel, so a 5-minute difference between scan times was allowed. Finally, GOES effective radius values from each pixel within every identified cloud were averaged, and the corresponding MODIS values were also averaged. By taking the cloud-averaged values, we hope to minimize any possible errors associated with the GOES/MODIS scan time differences. A total of 120 clouds were identified over the 11 days, and the result of the comparison is given in Fig. 13. Using a Student's t-test, the resulting correlation (with correlation coefficient $r = .69$) is significant at a 99.9% confidence level. Note that the GOES-derived effective radius values tend to be larger than those from MODIS (a bias of 8.6 μm), particularly on the larger end. However, over 47% of the variance in the MODIS retrieval is explained by the best-fit curve, suggesting that despite its limitations in spatial and spectral resolution, GOES does a reasonable job of estimating thick cirrus cloud effective radius, at least compared to the MODIS algorithm.

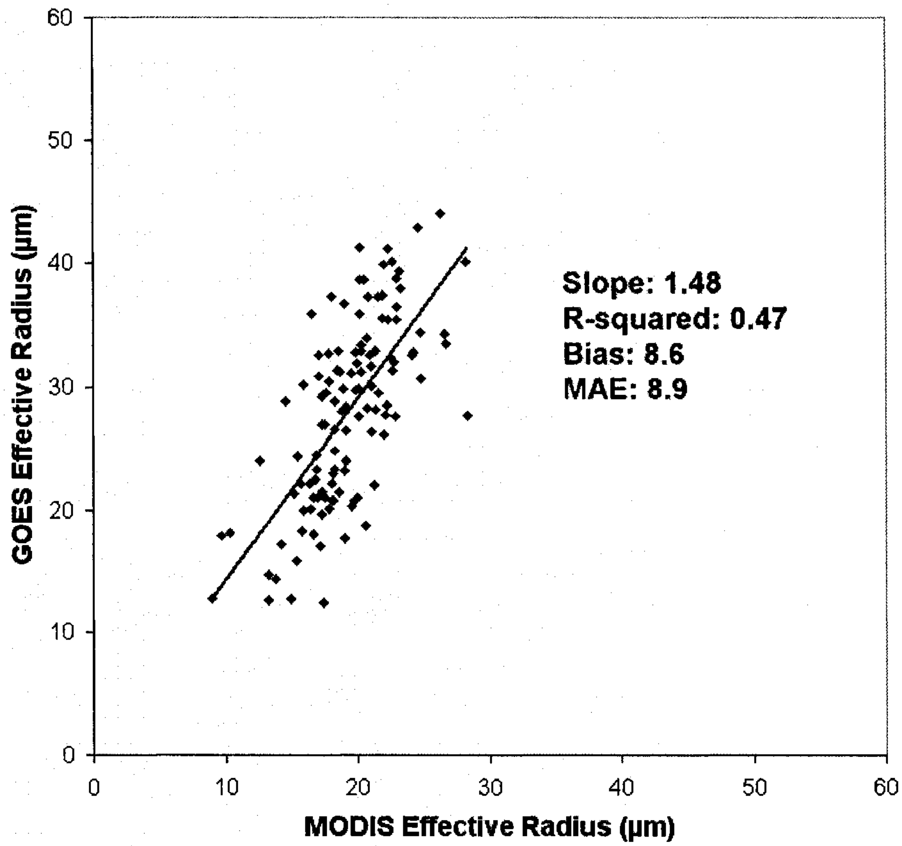

Figure 13. Comparison of effective radius retrievals from MODIS and GOES. Each dot represents a mean effective radius from an individual cloud. The solid line represents the least-squares linear best-fit. The slope of the best-fit line and associated R-squared is indicated, as well as the bias and the mean absolute error (MAE).

Some of the differences between GOES and MODIS may be attributed to the GOES instrument noise described above in Section 4.2.1, but even at the smaller effective radii, the GOES-retrieved values tend to be a bit larger than those from MODIS. Other possible reasons for the observed differences include, but are not limited to: MODIS spatial resolution of 1-km allows smaller-scale cloud structure to be observed compared to GOES; the time difference between GOES and MODIS scans; differences in the development of the retrieval itself, including the use of the 3.9 μm band for GOES and the 2.13 μm band for MODIS, and using different radiative transfer models; errors in the calculation of 3.9 μm reflectivity with GOES; differences in the viewing geometries of MODIS and GOES. Despite the differences, the ultimate goal of this retrieval is not to mimic that of MODIS, but rather to develop a reasonably accurate method which can be run in real-time using GOES. Diurnal trends in cloud-top effective radius can be monitored, while the absolute value of the retrieved effective radius is not particularly important.

4.2.3 GOES-East/West Comparison

A second indirect method to assess retrieval uncertainty makes use of the overlap in coverage of GOES-East and GOES-West over the central U.S. This overlap allows near-simultaneous effective radius retrievals of a single cloud at two different scattering angles. If the independent retrievals turn out to be similar, it suggests that the assumed ice crystal scattering properties are reasonable. On the morning of 6 June 2005, thick cirrus clouds were observed between 110°W - 95°W longitude over the U.S., and numerous thunderstorms formed later in the day in the same region, many of which having very small effective radii. This day is an excellent choice for the comparison described above since 1) both GOES satellites were in Rapid Scan Operation (RSO), providing many times for simultaneous scans, 2) observed thick cirrus clouds had a very wide range of effective radii, and 3) cirrus clouds occurred throughout the day, allowing for a wide range of solar zenith angles.

Starting at 1531 UTC and continuing to 2345 UTC, each time in which GOES-East and GOES-West scan times differed by no more than two minutes were identified (23 total; scattering angles vary from ~ 90° - 151°). At each time, an automated algorithm was used to locate every individual cloud having at least ten 10.7 μm pixels colder than -40 °C and having a mean visible reflectance greater than 0.60. This cloud identification process was implemented for both GOES-East and GOES-West independently. The effective radius was retrieved for each pixel, and values were averaged for each cloud, providing a cloud mean effective radius. Corresponding clouds were identified, with care being taken to ensure the same cloud was being viewed by both satellites.

Fig. 14a is a scatterplot showing the 3.9 μm reflectivity of each cloud as viewed by the two satellites; the linear best-fit line and 1-to-1 line are provided for reference. The best-fit line in Fig. 14a has a slope of 0.54, and GOES-East has a 1.0% high bias compared to GOES-West, indicating that GOES-East regularly measures larger 3.9 μm reflectivities than GOES-West since most of the convective clouds occurred in the afternoon hours, providing a forward-scattering direction for GOES-East. Both the slope and variance are significantly improved with the effective radius retrieval (Fig. 14b). This strong correlation between the GOES-East- and GOES-West-retrieved effective radii suggests that the assumed scattering properties perform quite well. The remaining variance could be associated with any number of potential errors, including those listed at the beginning of Section 4.2, as well as slight calibration differences between GOES-10 and GOES-12. Fig. 14a is provided to show that using 3.9 μm reflectivity alone to infer effective radius would lead to significant errors, but taking into account the expected scattering properties of ice clouds and the sun-satellite geometry significantly improves the retrieval (Fig. 14b).

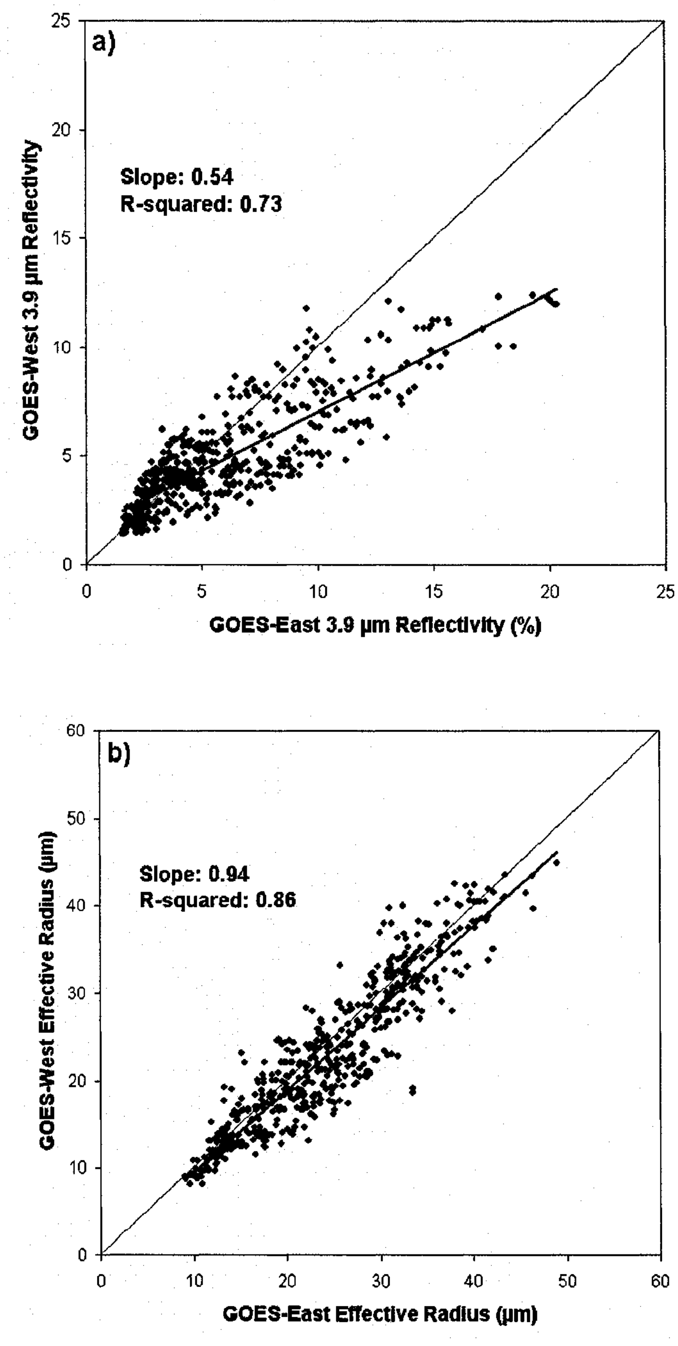

Figure 14. GOES-East/West comparison of a) 3.9 μm reflectivity, and b) retrieved effective radius, from optically thick ice clouds occurring on 6 June 2005 between 1531 - 2345 UTC in the central U.S. Both 3.9 μm reflectivities and effective radii were computed by averaging all pixel values for each cloud. The thick line is the least-squares linear best-fit; the thin line is the one-to-one line for reference. The slope of the best-fit line and associated R-squared is indicated.

4.2.4 Shape Parameter

One arbitrary choice when setting up the forward model runs was the Gamma distribution's shape parameter (α in Eq. (1)), which we chose to be 1. To test the model's sensitivity to this parameter, 3.9 μm reflectivities were calculated for all effective radii using shape parameters of 0 and 4. The largest difference in 3.9 μm reflectivity occurs for an effective radius near 11 μm, a difference of 1.7%. This corresponds to an effective radius uncertainty of +/- 2.0 μm at solar zenith angles approaching 70°; the uncertainty is lower for smaller zenith angles. Considering the wide range of effective radii observed (e.g., see Fig. 3), a maximum uncertainty of 2.0 μm at certain effective radii and solar zenith angles is not a concern. We chose $\alpha = 1$ as an intermediate value between the more extreme possibilities.

4.2.5 Effective radius climatology

In Chapter 3, a map of mean summertime thick cirrus cloud 3.9 μm reflectivity was shown in Fig. 3. It is noted that mean values as viewed from GOES-East and GOES-West differ over certain parts of the country, likely due to preferential forward scattering. Another way to test the effective radius retrieval is to redo this climatology, and plot the mean effective radius rather than the mean 3.9 μm reflectivity. If the magnitudes and locations of maxima/minima agree, this lends more evidence that the assumed scattering properties are reasonable.

Figs. 15a and 15b show the results of this climatology for May, June, July, and August of 2000, 2003, and 2004. Here, we have simply used the observed 3.9 μm reflectivities and solar and satellite geometry parameters along with the lookup tables described above to retrieve effective radius, before calculating the mean values. Notice that over the central U.S., a minimum in mean effective radius is found in southeast Colorado and northeast New Mexico extending into the Texas panhandle. The magnitude and location of this minimum is very similar as viewed from both GOES-East (Fig. 15a) and GOES-West (Fig. 15b). It should be noted that the visible reflectance thin cloud screen was not applied in making these maps because a) it was not applied in Fig. 3, and b) visible data over this period is not readily available. However, based on the results above, we feel that applying the screen will not significantly alter the results. The significant difference in mean effective radius between the High Plains and the eastern U.S. is most likely related to the typical low-level thermodynamic environment in which thunderstorms form, which will be discussed in detail in Chapter 5.

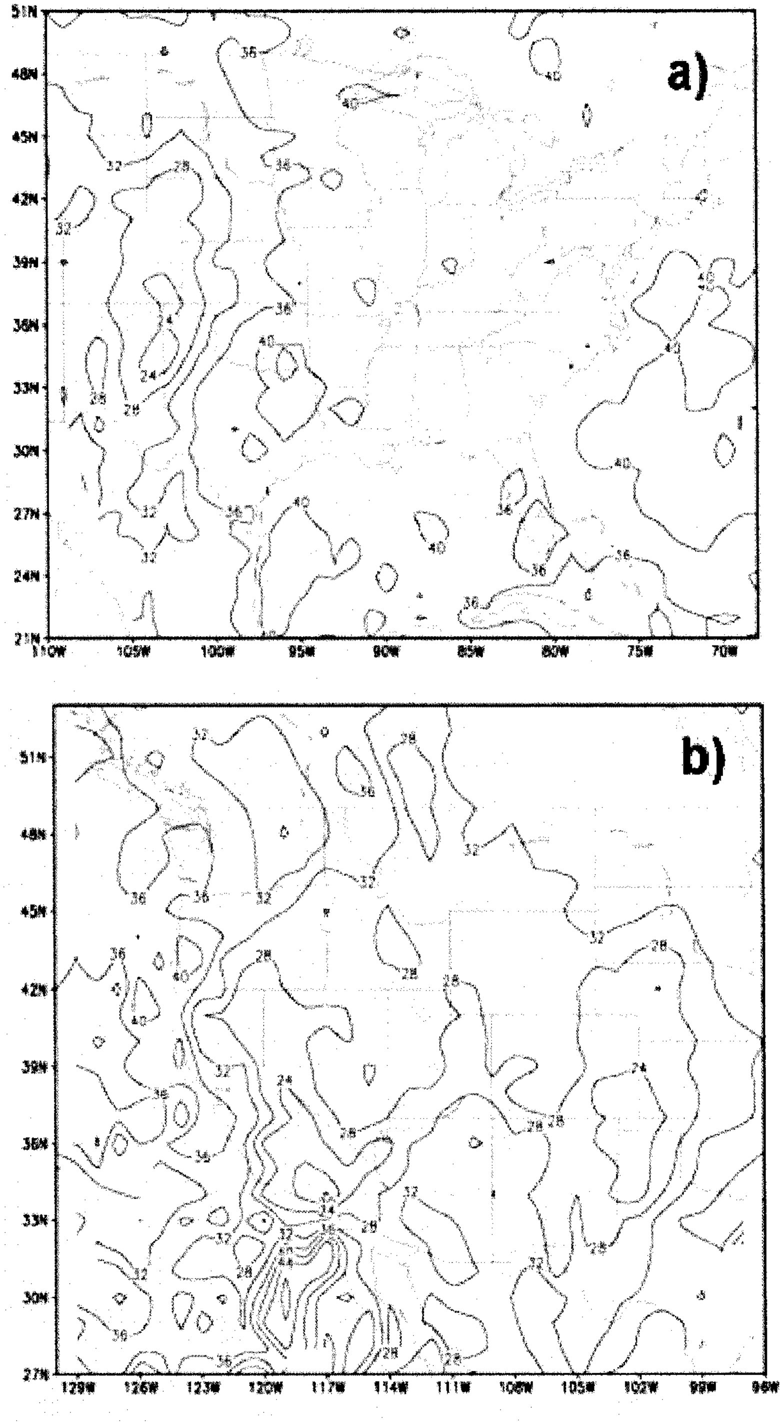

Figure 15. Mean effective radius (μm) of ice clouds from a) GOES-East and b) GOES-West, during May, June, July, and August of 2000, 2003, and 2004, when the solar zenith angle was less than 68°. GOES-East (a) covers much of the eastern Continental U.S., while GOES-West (b) covers the western portion.

CHAPTER 5

PHYSICAL MECHANISMS RESPONSIBLE FOR CLOUD-TOP ICE CRYSTAL SIZE

Up to this point, it has been established that differences in cloud-top ice crystal size exist in various clouds, but there has been little discussion about why these differences occur. Determining the exact physical mechanisms is a very difficult task since detailed observations of small-scale cloud processes in thunderstorms are extremely rare. This is particularly true in the core of a thunderstorm, where the most important processes are likely occurring. In order to investigate these processes, four methods will be employed: 1) a statistical analysis of the pre-storm environments favorable for clouds with differing cloud-top ice crystal sizes, 2) discussion of some basic cloud physics theory, 3) observations of the "CCN effect", and 4) three-dimensional cloud model simulations.

5.1 Statistical Analysis

To investigate whether the pre-storm environment plays a role in determining cloud-top ice crystal size, a composite analysis was performed over the High Plains region having the smallest mean effective radius (Fig. 15a). The analysis domain was chosen roughly within the 32 μm contour in Fig. 15a, or between approximately 30°-45°N latitude and between 100°-110°W longitude. This small domain was selected to minimize other factors which may vary geographically, such as CCN concentration. GOES data during the summer months (June, July, August) of 2003 and 2004 were analyzed, and 16 convective days having a large percentage of thunderstorm tops with relatively small effective radii (roughly less than 26 μm; hereafter referred to as "small ice days") and 16 convective days having a large percentage of thunderstorm tops with relatively large effective radii (roughly greater than 26 μm; "large ice days") were selected. Days similar to those in Figs. 1a and 1b are typical examples of a small ice day and a large ice day, respectively. The mean effective radius was 17.3 μm for the small ice days and 36.8 μm for the large ice days.

For each of the 16 small ice and 16 large ice days, a subset of the domain was chosen based on the location of convective activity. Within this smaller area, all grid points from the North American Regional Reanalysis (NARR) dataset (Mesinger et al. 2006) were extracted. This dataset uses the NCEP Eta model and its data assimilation system, so its horizontal grid spacing is 32 km, it contains 45 vertical levels, and output is available every 3 hours. Additionally, observed precipitation is assimilated hourly and other data sets are incorporated, such as the Noah land surface model. For more details about the NARR, see Mesinger et al. (2006). For each of the 32 days in the analysis, between 500 and 1000 grid points were selected within the subset having convective activity. The 0000 UTC values of temperature, dewpoint, and wind for the entire troposphere were averaged for each of the 16 days. These mean profiles were then averaged for the small ice and large ice days, producing two final mean profiles (Fig. 16). Many of the grid points used in this analysis have surface pressures above 850 hPa, so the profiles are most meaningful at pressures below 850 hPa.

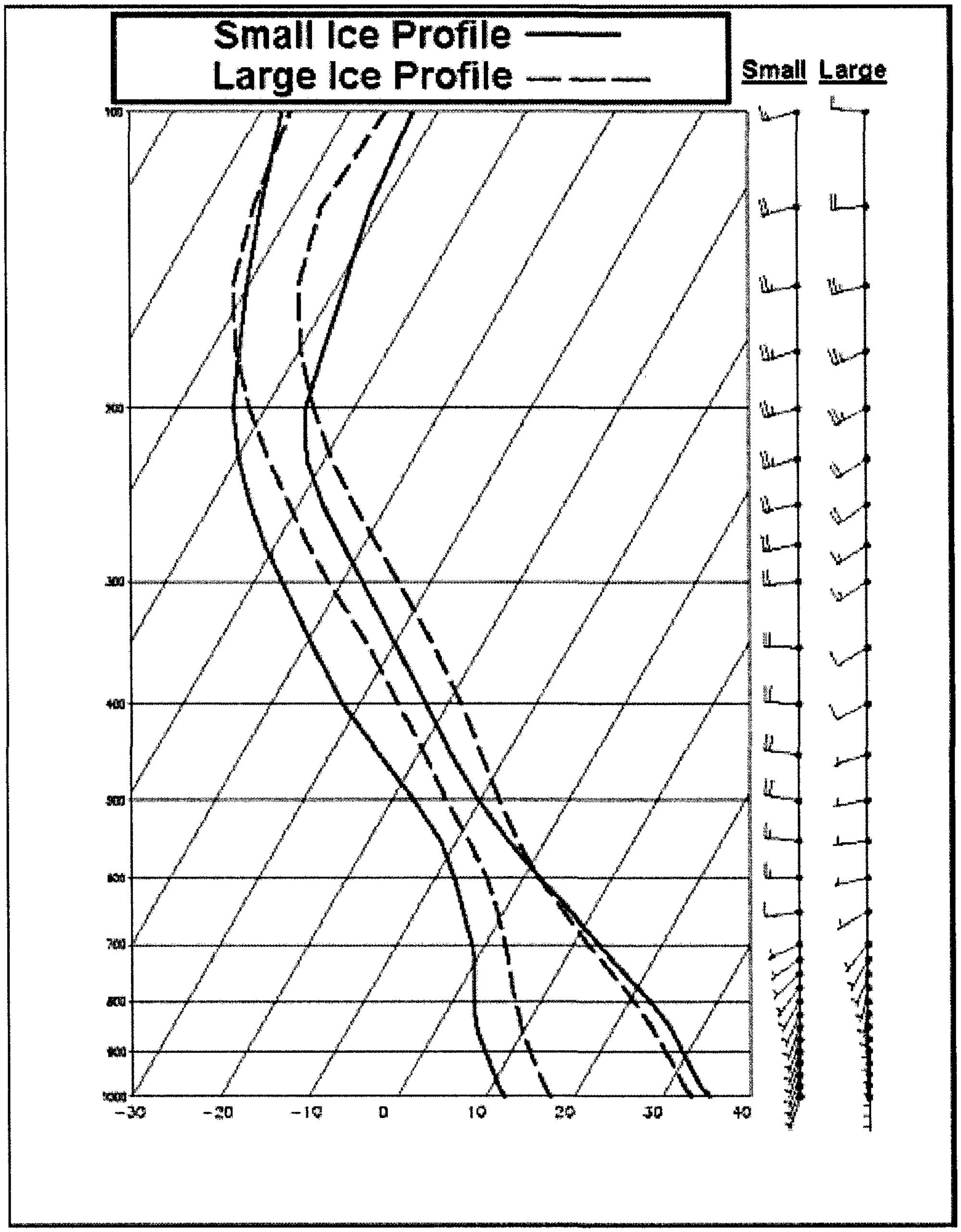

Figure 16. Mean temperature (right) and dewpoint (left) profiles for the small ice (solid) and large ice (dashed) cases, along with mean wind profiles, plotted on a traditional skew-T/log-p diagram. A full wind barb represents 10 knots.

There are several important differences between these two mean profiles. First, the relative humidity throughout the small ice profile is lower, especially in the lowest 400 hPa. A larger dewpoint depression near the surface suggests that a fairly dry boundary layer is supportive of thunderstorm tops with small cloud-top ice. Second, the 800-300-hPa lapse rate is noticeably steeper in the small ice case. This more unstable environment would promote stronger updrafts. Finally, the mid-level westerlies are stronger in the reflective case, resulting in larger surface-to-500-hPa shear.

To get a more quantitative understanding of the results, values of selected variables were collected at each grid point, and means and standard deviations were calculated for each of the 32 days. Next, the resulting means were averaged together for each case (small ice and large ice), and the standard deviations were also averaged. Results are given in Table 2. To estimate significance, a difference-of-means t-test was performed using the mean standard deviations calculated above. Values in Table 2 with greater than 95% significance are in italics; those exceeding 99% significance are in bold.

Table 2. Means for several parameters for the 16 small ice and 16 large ice days. Italicized numbers indicate the difference of means exceeds 95% significance; bold numbers for difference of means exceeding 99% significance.

Parameter	Small Ice Mean	Large Ice Mean
CAPE (J/kg)	*567*	*219*
Precipitable Water (mm)	**17.7**	**23.1**
Surface Temperature (˚C)	28.2	26.1
Surface Dew Point (˚C)	*4.5*	*7.2*
700 hPa RH (%)	**42**	**56**
500 hPa RH (%)	58	65
800-500 hPa Lapse Rate (˚C per km)	**8.5**	**7.4**
Sfc - 500 hPa Zonal Shear (ms^{-1})	**9.9**	**2.3**
Depth of cloud base to -38 ˚C level (m)	*5210*	*6036*

Difference of means exceeds 95% significance

Difference of means exceeds 99% significance

The Convective Available Potential Energy (CAPE) for the small ice case is over twice that of the large ice case, verifying that instability is greater when smaller cloud-top ice is observed (even though convection was observed in both cases). Precipitable water values are smaller and 700-hPa relative humidity values are lower for the small ice case, further underscoring the possible importance of relatively dry air. Lapse rates are significantly steeper in the small ice case (the standard deviations for lapse rate were very small), and the surface-to-500-hPa zonal shear is much larger on the small ice days.

Surface temperature and dewpoint values were used to calculate the lifted condensation level (LCL). Using this as the cloud base height, the distance from cloud base to the homogeneous freezing level, taken to be -38 °C assuming ammonium sulfate CCN (DeMott et al. 1994), was calculated for both cases, and cloud depths are significantly larger in the large ice case.

5.2 Theory of Cloud Droplet and Ice Crystal Sizes

In order to discuss cloud droplet and ice crystal sizes, it is best to begin with the initial cloud droplet nucleation process. The majority of this discussion is based on parts of Rogers and Yao (1989). Within a parcel of rising air, cloud droplets will begin to form when the air reaches saturation, assuming there are at least some CCN available (and observations show that *some* CCN are virtually always present). It is typically assumed that cloud droplets are distributed in a well-behaved manner, such as a Gamma distribution, and the mean size of that distribution can be tracked as a proxy for the size of the droplet population.

In general, two factors determine the mean size of the cloud droplet population: the total water mass and the droplet number concentration. Total water mass depends on the temperature at which saturation occurs, and is governed by the Clausius-Clapeyron relationship. Colder air holds less water vapor than warmer air, so clouds which form at colder temperatures will have less available water vapor and therefore less total water mass. Droplet number concentration depends primarily on the number of available CCN, but also on the ambient supersaturation (which in turn depends on the updraft strength).

Rogers and Yao (1989) note a relationship between droplet number concentration, (N), CCN concentration (C), and updraft speed (U) based on earlier work by Twomey:

$$N \approx 0.88C^{2/(k+2)}[7x10^{-2}U^{3/2}]^{k/(k+2)}, \tag{6}$$

where k can vary between 0.4 and 1.0. If we choose k to be 0.8 and C to be 600 cm^{-3}, Fig. 17 shows the relationship between activated droplets and updraft strength from Eq. (6). Notice that when U is near 7 m s^{-1}, the number of activated droplets begins to exceed 600 cm^{-3}. This seems to be an unrealistic result since more cloud droplets are forming than CCN are available (C). It is suspected that Eq. (6) is most relevant for clouds with relatively weak updrafts, so for stronger updrafts, the curve should technically approach the limit of available CCN, in this case 600 cm^{-3}. The bottom line of this analysis is that for clouds whose updrafts exceed ~10 m s^{-1}, nearly all of the available CCN should be nucleated.

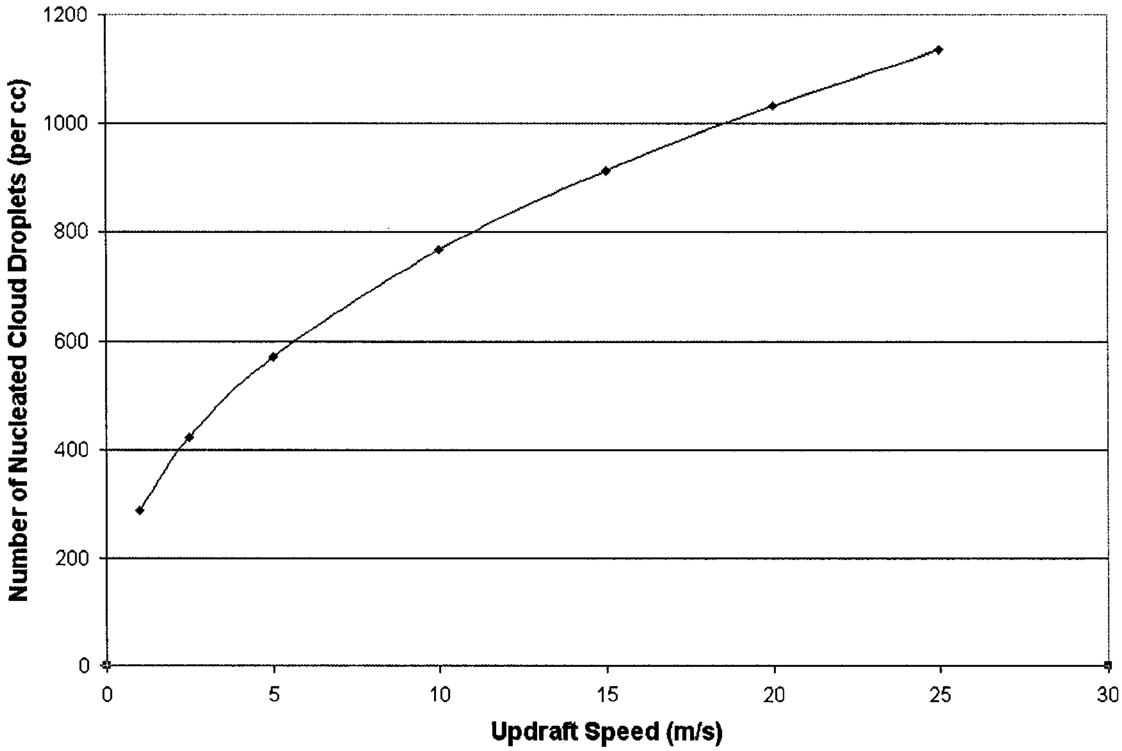

Figure 17. Relationship between updraft strength and number of nucleated cloud droplets using Eq. (6), with C=600 cm^{-3} and k=0.8.

In order to get a general idea of realistic cloud droplet sizes, and how the size depends on water mass and number concentration, it is useful to derive an expression for cloud droplet mean diameter. If we assume that a cloud droplet is spherical, its diameter, D, is given by

$$D = \left(\frac{6V}{\pi}\right)^{1/3}, \qquad (7)$$

where V is the volume of a single cloud droplet. If the cloud droplet mass mixing ratio is given by M (grams of cloud water per kg of air) and the number concentration is given by N (number of cloud droplets per kg of air), then their ratio, M/N, gives the mass of a single droplet in grams. Letting ρ_W be the density of water, then

$$V = \frac{M}{N\rho_W}. \tag{8}$$

Substituting Eq. (8) into Eq. (7), we get

$$D = \left(\frac{6M}{\pi N \rho_W} \right)^{1/3}. \tag{9}$$

If we let $\rho_W = 1$ g cm^{-3}, and note from the forthcoming cloud model results that M generally varies between 0.5 and 8 and N depends on CCN concentration (but a reasonable value is 600 mg^{-1}), then Figs. 18 and 19 show D from Eq. (9) as a function of cloud water mass mixing ratio and cloud droplet number concentration, respectively.

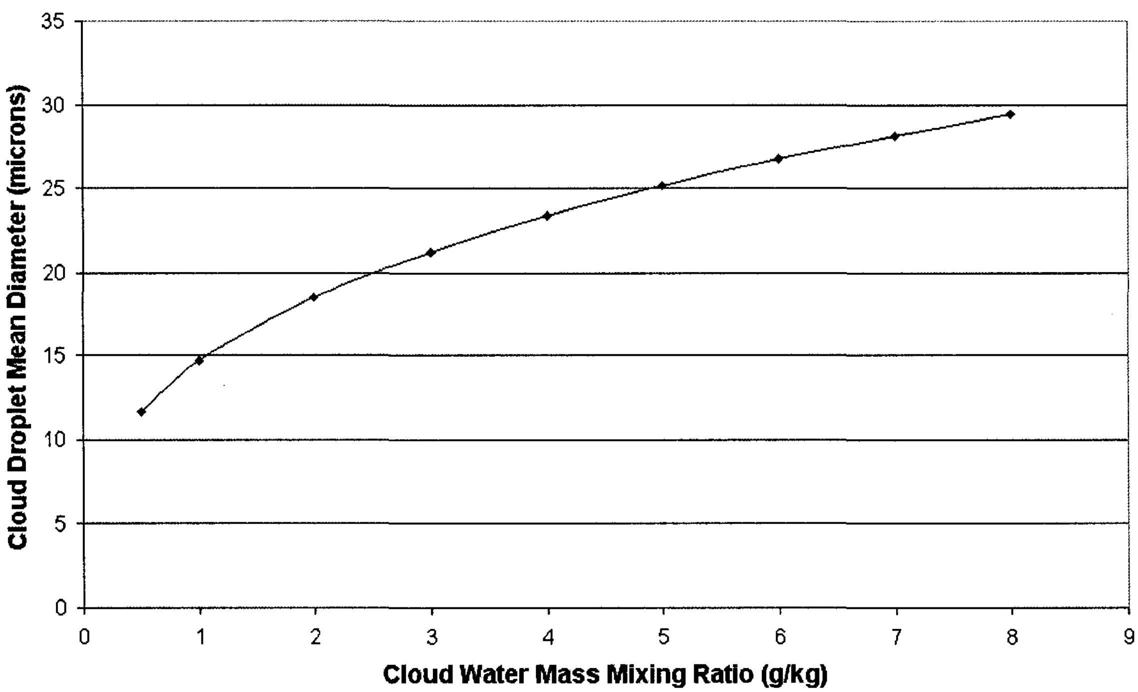

Figure 18. Cloud droplet mean diameter (μm) as the cloud water mass mixing ratio is varied, from Eq. (9). Cloud droplet number concentration, N, is fixed at 600 mg^{-1}.

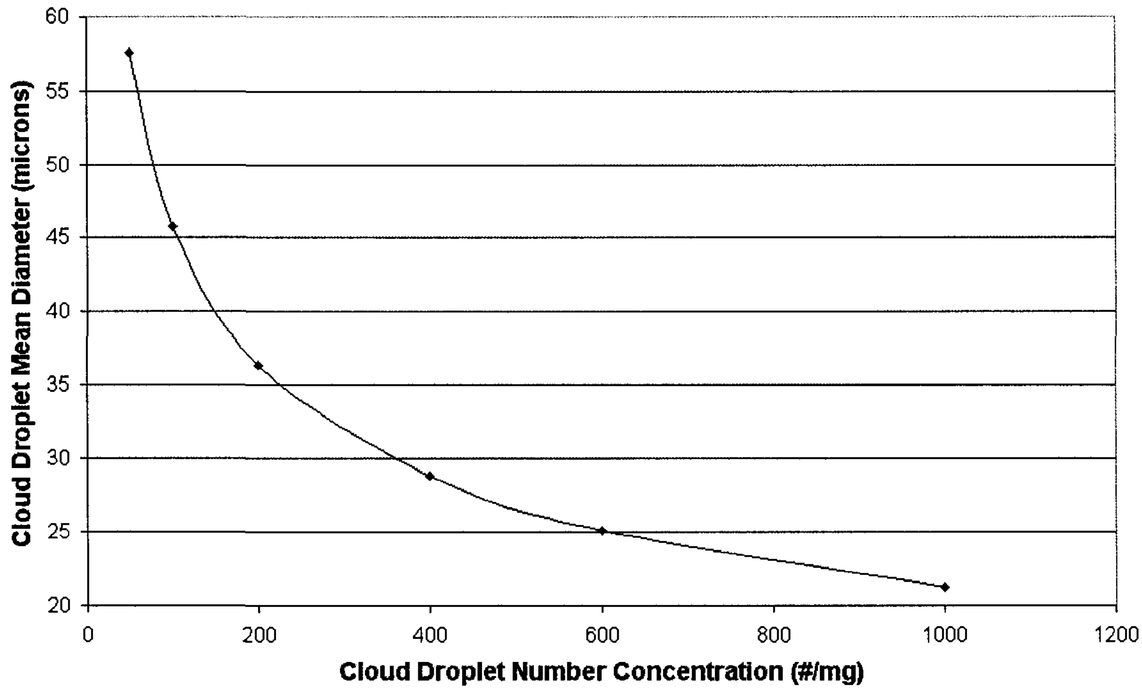

Figure 19. Cloud droplet mean diameter (μm) as the cloud water number concentration is varied, from Eq. (9). Cloud droplet mass mixing ratio, M, is fixed at 5 g kg^{-1}.

Fig. 18 shows that the cloud droplet mean diameter varies between about 10 and 30 μm for reasonable values of mass mixing ratio and a number concentration of 600 mg^{-1}, and adding more water mass results in larger droplets. This also means that, in general, larger droplets can be expected in clouds with warmer cloud-base temperatures. Fig. 19 shows that cloud droplet mean diameter decreases as the number concentration increases. Based on the discussion above, then, adding more CCN should result in smaller cloud droplet mean diameters, but this result is well documented in the literature.

As the cloud droplet population is lofted vertically within an updraft, several processes can potentially occur. First, collision-coalescence between the cloud droplets results in larger droplets, and the collection efficiency is a function of droplet size, so that smaller droplets collect less frequently than larger droplets (Rogers and Yao 1989).

Second, the cloud droplets will grow by condensation. Third, when the temperature drops below 0 °C, some of the droplets may begin to freeze heterogeneously if ice nuclei (IN) are present. As soon as ice is present, cloud droplet growth by condensation is considerably decreased because the available water vapor will preferentially deposit onto the ice crystals. Additionally, the ice begins to accrete cloud water droplets and often will grow appreciably as it's lofted higher into the storm. Any cloud droplets which are still in the form of liquid will freeze homogeneously when they reach -40 °C. Therefore, thunderstorm anvils are, in general, composed of ice which may have frozen either heteorogeneously or homogeneously, but the relative "activeness" of these two processes is fairly undocumented in the literature.

The growth of a population of ice crystals in a mixed phased environment is quite complex and is difficult to diagnose without the help of a cloud model. In general, though, ice freezing heterogeneously has more opportunity to grow to larger sizes than does homogeneously frozen ice (Rosenfeld et al. 2008). Graupel and hail are examples of heterogeneously frozen ice crystals which have grown appreciably from their original size. Cloud droplets which make it to the -40 °C level and freeze homogeneously are generally significantly smaller than ice which formed in the mixed phase region. When these relatively small droplets freeze, the resulting ice crystals should be approximately the same size as the droplets. Further ice growth may occur by vapor deposition at temperatures below -40 °C, but water vapor contents are quite low at temperatures that cold, so these homogeneously frozen particles will likely remain quite small. The best way to diagnose the result of these complex and intertwined cloud water and ice formation and growth processes is with the use of a cloud model having a sophisticated treatment of cloud physics.

In summary, updraft strength helps in determining the number of CCN which are activated, but for a relatively strong updraft, all CCN will likely serve to form cloud droplets. Cloud droplet size is determined by the amount of available water vapor and the number of available CCN. As water vapor mass increases, cloud droplets get larger, and as CCN concentrations increase, cloud droplets get smaller. Cloud droplets freezing homogeneously will approximately maintain their size after they become ice crystals.

5.3 Observations of the CCN Effect

Since the processes governing the resulting cloud-top ice crystal size are so complex, isolating one process and observing that in nature is a very difficult task. However, occasionally a natural experiment presents itself. In the case of the effect of CCN on ice crystal size, an event was observed by GOES back in 1998, which provides a very convincing link. Large wildfires are relatively common during the summer throughout much of Canada and Alaska. Under the right conditions, the massive amount of heat from a large fire can help initiate convection directly over it, and the resulting "pyrocumulonimbus cloud" (pyroCB) can readily be observed from satellite (e.g. Fromm et al. 1998). Wildfires typically generate a massive amount of smoke, and these aerosols may play an important role in the formation and evolution of the pyroCBs.

On 4 July 1998, a number of wildfires were burning in British Columbia and the Yukon (Fig. 20). The GOES 3.9 μm band is ideal for identifying fires due to its sensitivity to subpixel heat (Weaver et al. 2004). In Fig. 20, fires can be identified by the bright white pixels (warmest brightness temperatures). The largest fires were occurring in northwestern British Columbia and southern Yukon Territory, as noted in the bottom-left frame of Fig. 20. Convective clouds can be seen primarily north and east of these fires as the darker (colder) pixels. Fig. 21 is a 10.7 μm image showing the general convective activity. Most of the cloud top temperatures range between -40 and -60 °C. Using the 10.7 μm alone, it's impossible to identify the clouds forming over hot spots because their brightness temperatures are generally about the same as the surrounding "regular" convection. Closer examination of Fig. 20, bottom right panel, shows a storm going up just to the southeast of the largest fire in the Yukon (the fire and associated pyroCB is shown with a red box). Its 3.9 μm brightness temperature is significantly warmer (brighter colors) than the regular convection, suggesting that more solar radiation is being reflected and that it is likely composed by smaller ice crystals. Fig. 22 shows the GOES effective radius retrieval at four times when the sun was sufficiently high in the sky. By 0200 UTC (bottom right), four pyroCBs have become evident. They are easily identified by their extremely small effective radius values compared to the surrounding convection.

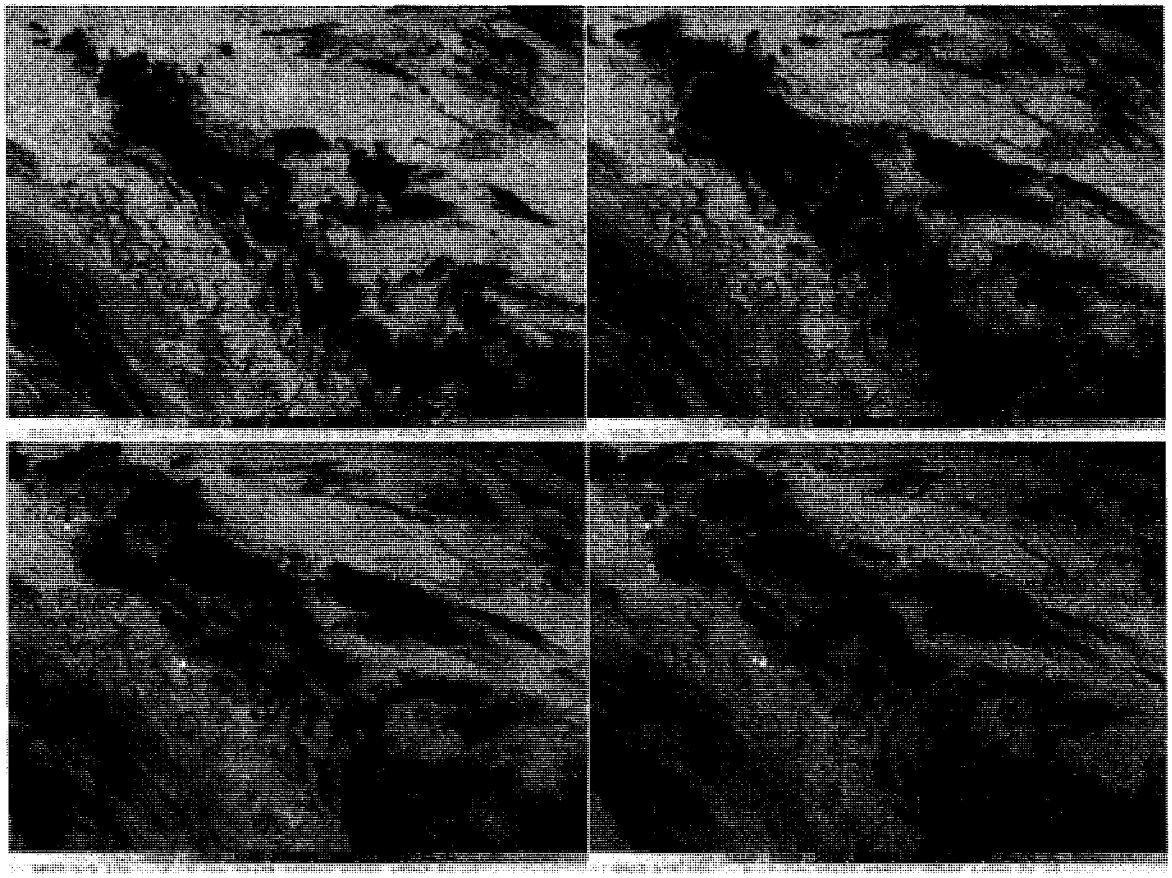

Figure 20. GOES-9 3.9 μm band from 4-5 July 1998 at 2245 UTC (top left), 0030 UTC (top right), 0200 UTC (bottom left), and 0300 UTC (bottom right). The locations of some wildfires are noted in the bottom left frame, and the location of a fire and associated pyroCB is shown with a red box in the bottom right frame.

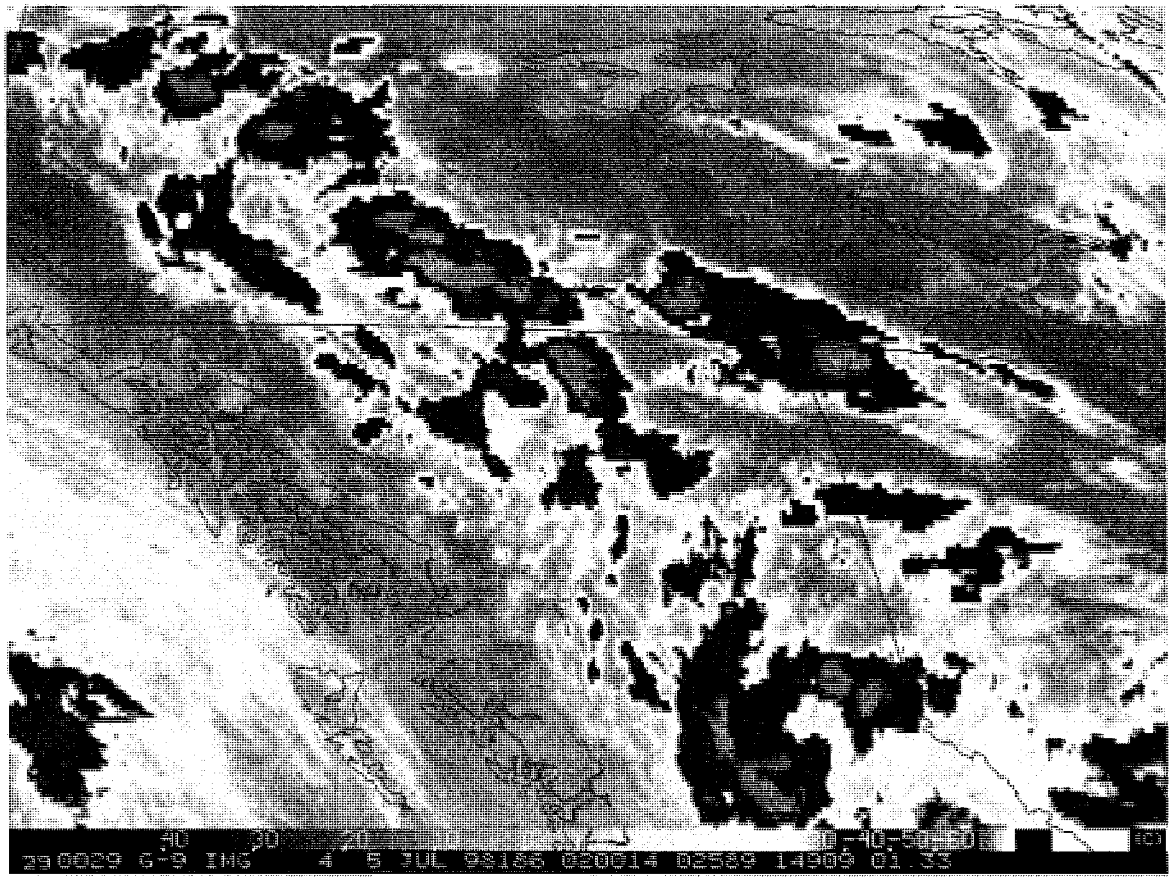

Figure 21. GOES-9 10.7 μm band from 5 July 1998 at 0200 UTC.

It is hypothesized that the small effective radii associated with the pyroCBs is a direct result of large amounts of CCN being provided by the fires. The resulting cloud then has a (relatively) large number of cloud droplets which must be smaller than the surrounding convection since the horizontal moisture availability likely doesn't vary dramatically. These small cloud droplets ascend in the vigorous updraft before freezing homogeneously, resulting in a large number of small ice crystals. What makes this a convincing case is that the only obvious difference between the pyroCBs and the surrounding convection is the availability of aerosols for those storms forming over the fires.

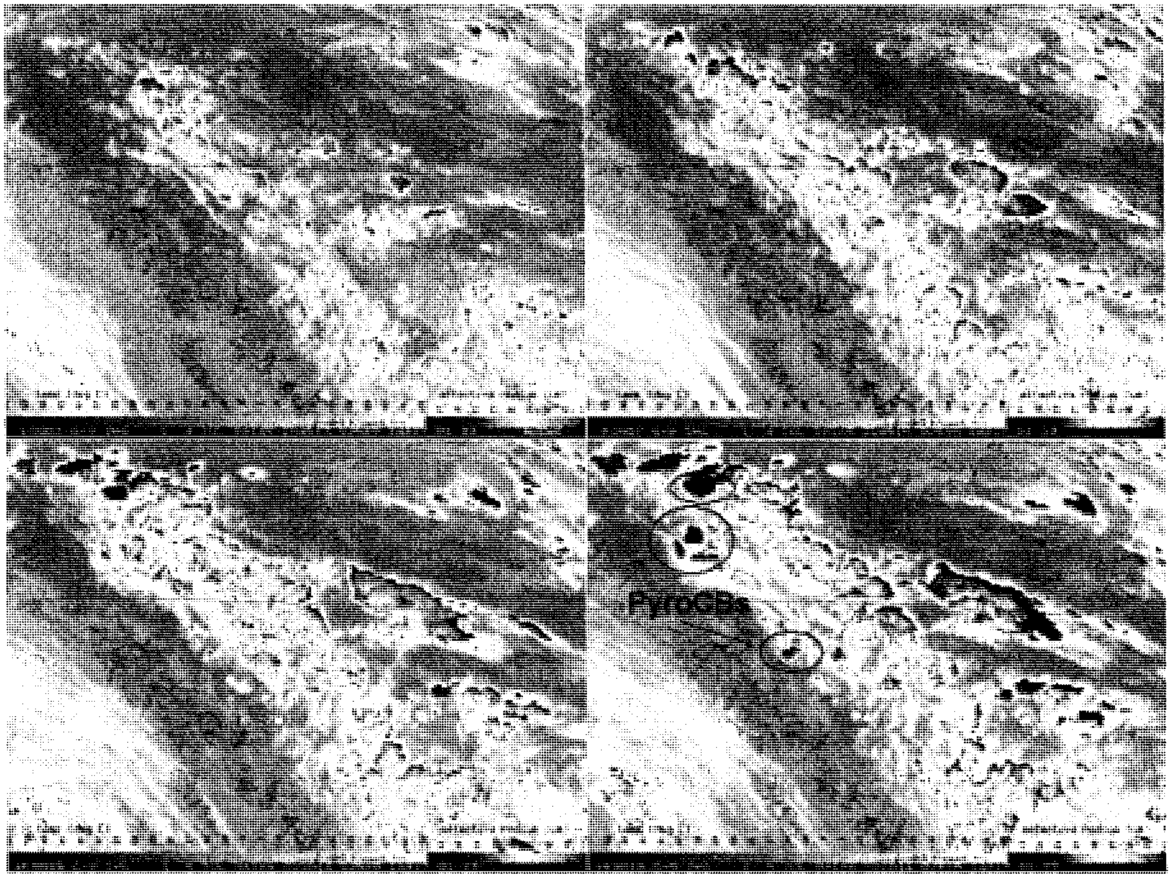

Figure 22. GOES-9 effective radius retrieval from 4-5 July 1998 at 2045 UTC (top left), 2245 UTC (top right), 0100 UTC (bottom left), and 0200 UTC (bottom right). The locations of some pyroCBs are noted in the bottom right frame.

Another interesting facet of this example is that the pyroCB anvils persisted through the night and into the next day. Their lifetime was about 6 hours longer than the anvils from the regular convection. This lends evidence to the "cloud residence time" idea, which is an aerosol indirect effect (IPCC 2007). The theory is that smaller cloud droplets result in less efficient collision-coalescence, decreasing precipitation production and sending more of the storm's water mass into its anvil. These anvils then persist longer, which has potential radiative effects. While this is an interesting result, it is beyond the scope of this study.

5.4 Cloud Model Simulations

The model used in this study is the Colorado State University Regional Atmospheric Modeling System (RAMS; Pielke et al. 1992; Cotton et al. 2003). It is a three-dimensional, non-hydrostatic, cloud-resolving model which employs a two-moment microphysics package (Meyers et al. 1997; Saleeby and Cotton 2004), a necessary feature for this particular study. Mass mixing ratio and number concentration are predicted for each of the following water species: cloud water, rain, pristine ice, snow, aggregates, graupel, and hail. A Gamma distribution is assumed, so that the mean diameter can be calculated for each water species.

As explained in more detail in Van den Heever and Cotton (2007) and Saleeby and Cotton (2004), initial CCN concentrations can be specified, and the number of activated cloud droplets is dependent on CCN availability. CCN mass is tracked so that if a droplet evaporates, that aerosol particle again becomes available for another nucleation event. Initial CCN concentrations are set to decrease with height, and if all available CCN are nucleated, then no further cloud droplets can form unless more become available.

Model simulations were performed using an idealized framework. Similar to Grasso and Greenwald (2004), horizontal grid spacing was set to 1-km within a 50 km by 50 km domain. Lateral boundaries were set using the Klemp and Wilhelmson (1978a) condition. Vertical grid spacing was set to 100 m at the surface, stretching to 500 m aloft, with 58 total vertical levels, and a wall with friction layers was placed at the top boundary. For each simulation, a horizontally homogeneous sounding was specified and each run was initialized with a warm bubble at the center of the domain.

Based on the statistical results presented in Section 5.1 and the pyroCB observations in Section 5.3, we will use RAMS to test the CCN effect, the cloud-base temperature effect, and the updraft strength effect. Even though vertical shear was shown to be significantly different between the large and small ice cases (Table 2), this will not be tested with the model because it is believed that anomalously weak westerly mid-level winds associated with an upper-level low in the southwestern U.S. accompanied some of the large ice cases. This synoptic setup often brings anomalously moist conditions to the High Plains, which will result in warmer cloud-base temperatures.

5.4.1 Base Case Simulation

For the forthcoming series of sensitivity tests, it is most convenient to perform a "base case" simulation upon which the remaining runs can be compared. Fig. 23 shows the sounding which is used to initialize the model. Ample low-level moisture sits below an extremely unstable airmass (the CAPE is 2651 J kg^{-1}) with abundant deep-layer sheer. A straight line hodograph is designed so that splitting supercells may occur (Klemp and Wilhemson 1978b). The goal of using this profile is to generate a long-lived, intense thunderstorm, but the details of the storm's microphysics are of largest interest in all of these runs. The model was allowed to run for 90 minutes. Interestingly, the details of the storm's microphysics were fairly constant within an intense updraft region (> ~20 m s^{-1}) throughout the simulation, so examining output as early as t = 20 minutes is equally as valuable as that output later on in the simulation after the effects of the initial warm bubble have completely disappeared. The base case is initialized with a surface CCN concentration of 1200 cm^{-3}.

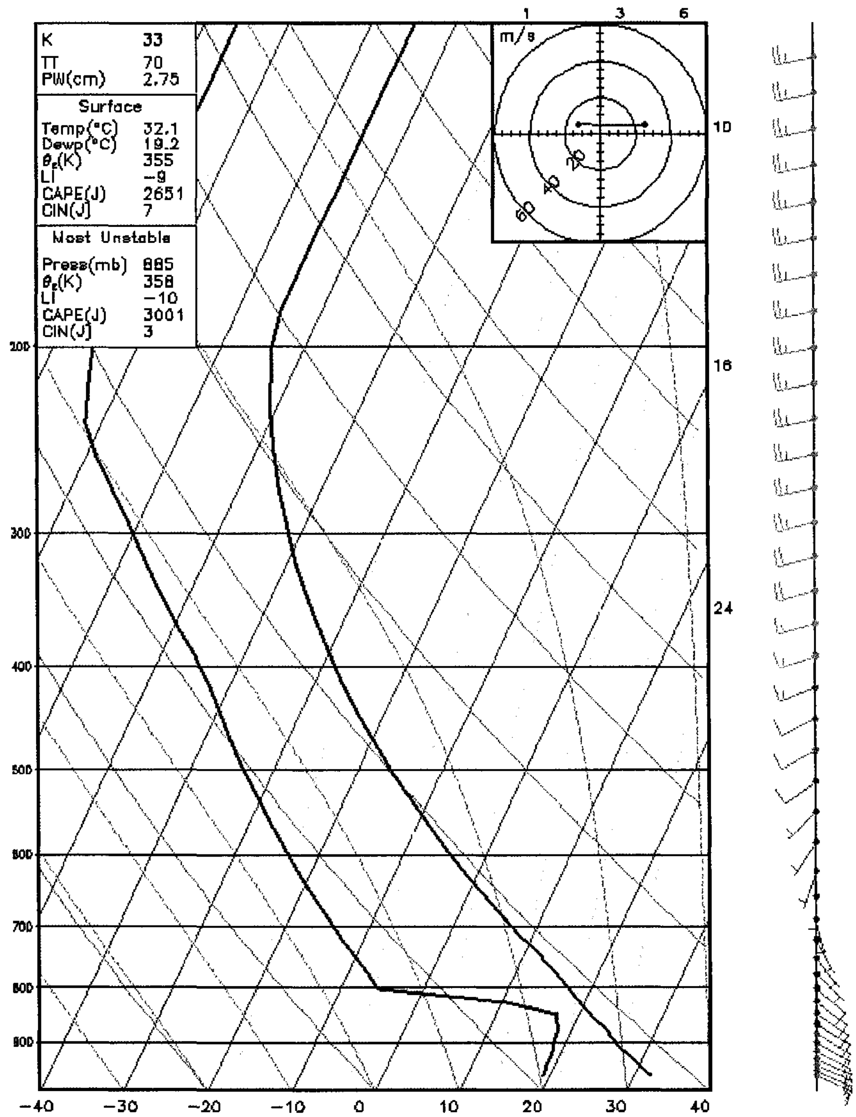

Figure 23. Sounding used to initialize the base case simulation.

Fig. 24 shows horizontal cross-sections at z = 3 km of vertical velocity for the base case at 6 different times. An intense updraft is evident, and by 45 minutes the storm has split into a right and left mover. By 65 minutes the right mover continues to persist and is still quite strong. A number of vertical cross-sections will be shown at $t = 35$ minutes along the black line in Fig. 24.

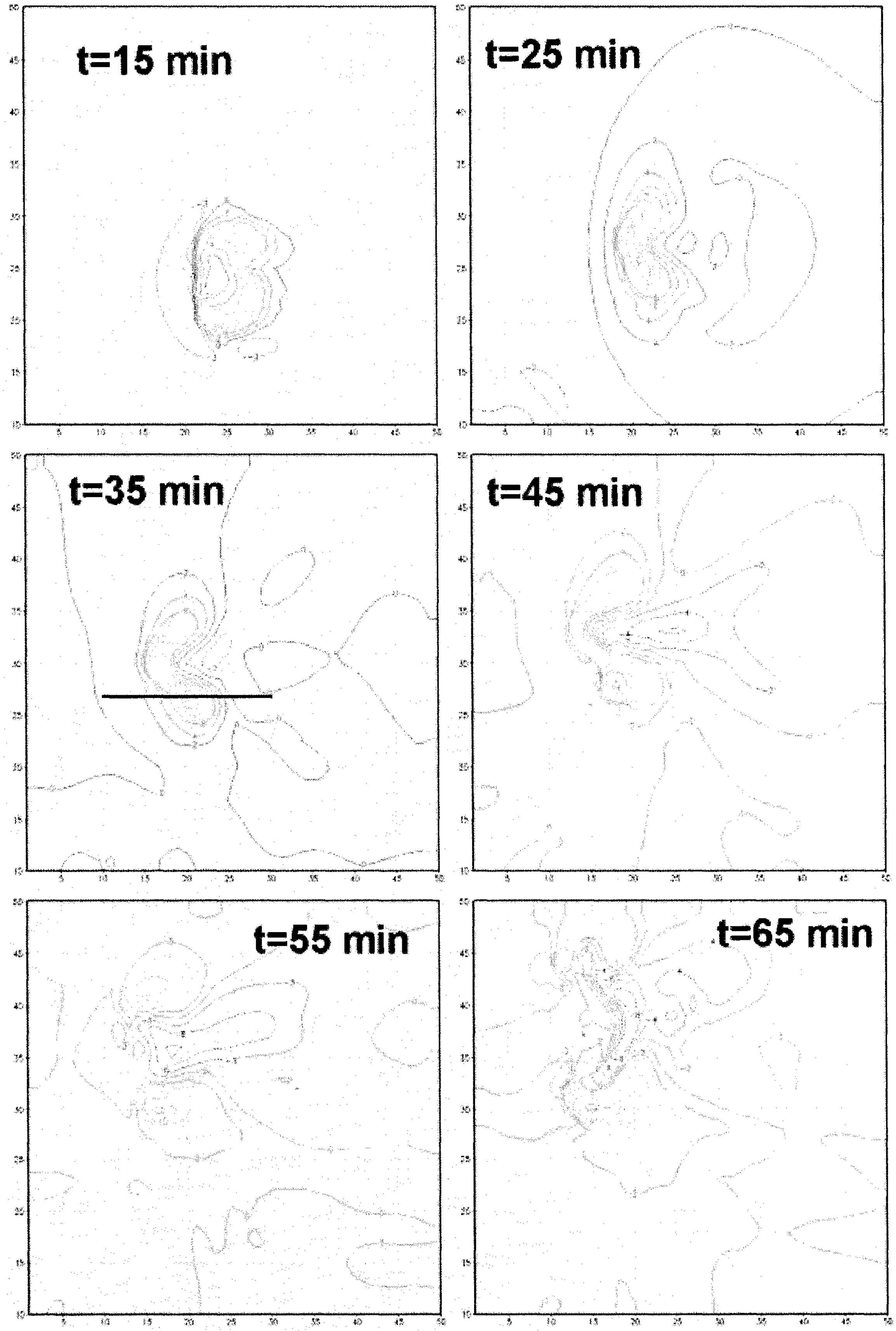
t=15 min
t=25 min
t=35 min
t=45 min
t=55 min
t=65 min

Figure 24. RAMS model output from the base case. Each panel is a horizontal cross-section at z = 3 km ASL showing vertical velocity (m s^{-1}), valid at the indicated times. Positive values indicate updrafts, negative downdrafts. The location of forthcoming vertical cross-sections is shown with a black line at t = 35 mins.

Fig. 25 shows a vertical cross-section of vertical velocity, cloud water mixing ratio, and pristine ice mixing ratio. Updraft speeds exceeding 40 m s^{-1} indicate a very intense storm. Cloud water mixing ratio values increase in a fairly uniform manner from cloud base up to about 6km ASL, and peak near 5.5 g kg^{-1} near 8 km ASL. This increase is due to droplet growth by condensation, and the fact the peak occurs just below the homogeneous freezing level suggests that the rate of mass increase due to condensation exceeds the rate of mass loss due to cloud droplets being transferred to other categories such as rain, graupel, or hail. Cloud water mass begins to rapidly fall just above 8km ASL due to homogeneous freezing, and is completely gone by -40 °C. Pristine ice mixing ratio values also peak near 5.5 g kg^{-1} in the core of the updraft, meaning that a very large percentage of the cloud water mass from below is being transferred to pristine ice mass. This is evidence that, in this simulation at least, homogeneous freezing is far more active than heterogeneous freezing. Notice that between 0 and 0.5 g kg^{-1} of pristine ice mass does exist between about 5 and 8 km ASL, so some heterogeneous freezing is occurring, but it only accounts for a small percentage of the total ice mass being injected in the anvil.

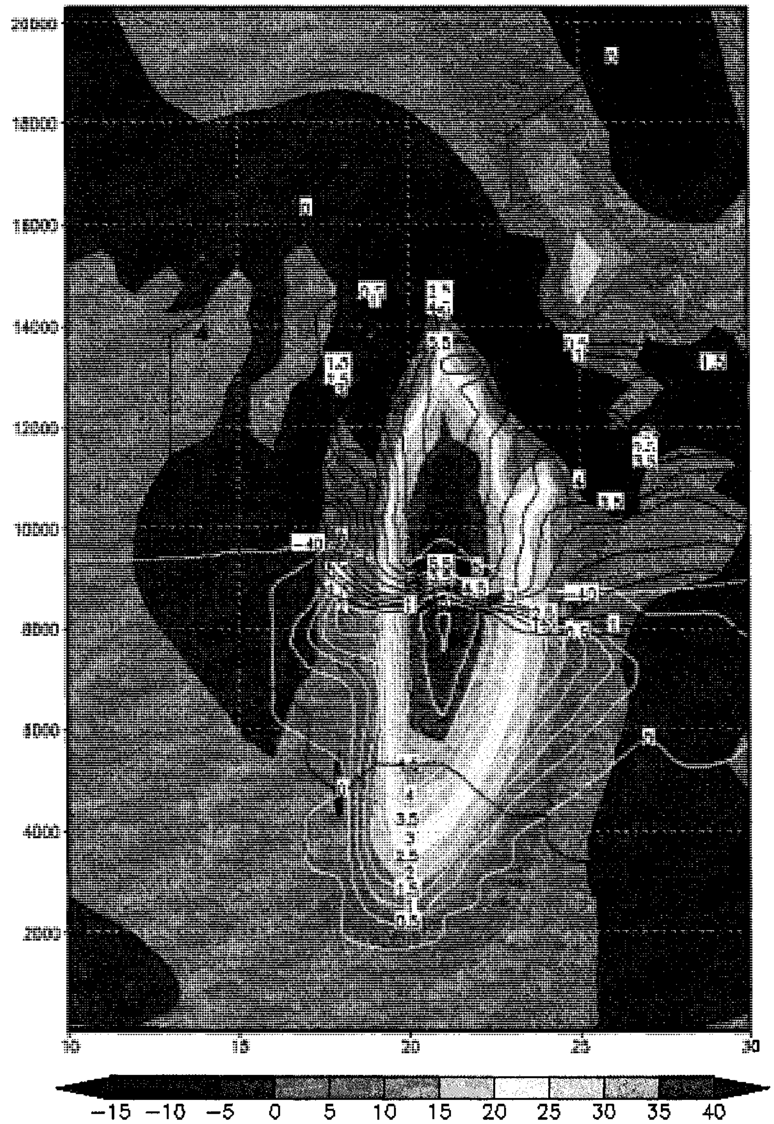

Figure 25. Vertical cross-section at the time and location shown in Fig. 24 of vertical velocity (colors, m s^{-1}), cloud water mixing ratio (white contours, g kg^{-1}), and pristine ice mixing ratio (black contours, g kg^{-1}) for the base case simulation. Also shown here and in the forthcoming figures in a white dashed line is the location of the -40 °C isotherm. The vertical scale is in meters ASL, and the horizontal scale is in km east of the western edge of the domain.

Cloud water and pristine ice number concentrations are shown for the same cross-section in Fig. 26. Values at cloud base are around 900 mg^{-1}, which when converted to cm^{-3} is fairly close to 1200 cm^{-3}, the initial surface CCN concentration. This means nearly all of the CCN are being activated near cloud base, as the analysis in Section 5.2 suggested may happen within an intense updraft. Cloud droplet number concentrations then decrease as they ascend to around 500 mg^{-1} just below the homogeneous freezing level. This decrease is due to some of the cloud droplets being transferred to rain, graupel and hail. After these droplets are frozen homogeneously, pristine ice number concentrations are also near 500 mg^{-1} within the updraft near the top of the cloud.

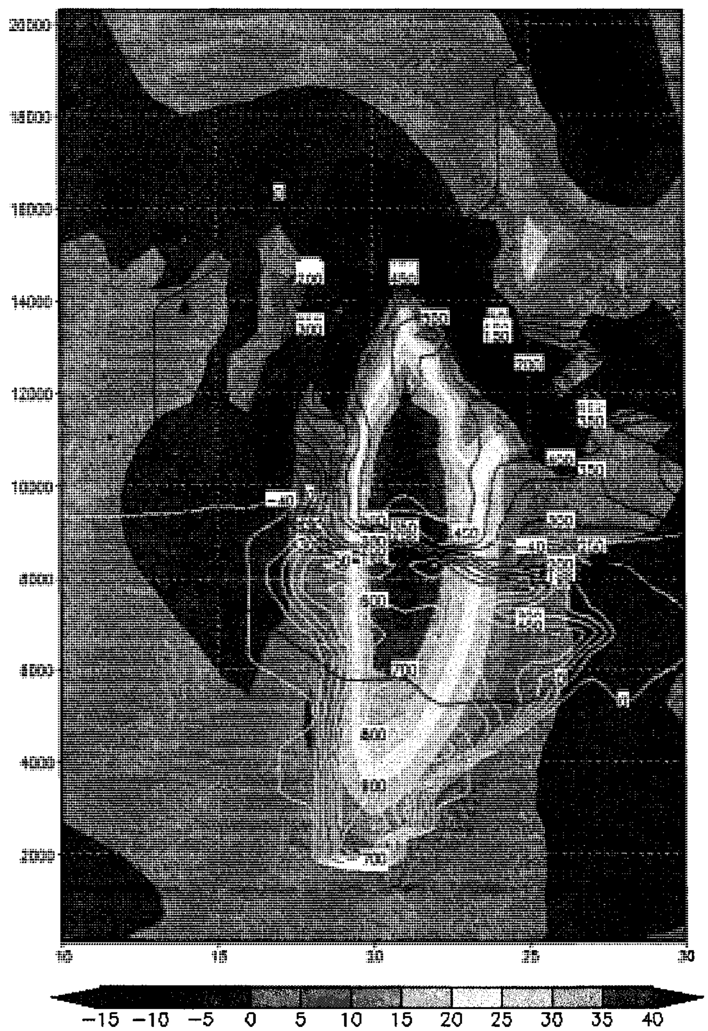

Figure 26. As in Fig. 25, except white contours are cloud water number concentration (mg^{-1}) and black contours are pristine ice number concentration (mg^{-1}).

Fig. 27 shows the resulting cloud droplet and pristine ice mean diameters based on the mass and number concentrations given in Figs. 25 and 26. Cloud droplets grow within the updraft to peak values near 25 μm, and after homogeneous freezing, pristine ice mean diameters are generally between 30 and 35 μm within the updraft region. Pristine ice sizes can be seen more readily in Fig. 28 (now in colors). The largest values are actually within the updraft, while slightly smaller values can be seen making up other portions of the anvil. By looking at a single cross-section, it is impossible to determine the reasons for the pristine ice sizes in areas outside the updraft core.

5.4.2 Testing the CCN Effect

Now that the base case has been established, we may begin performing some sensitivity tests. The first test involves decreasing the surface CCN concentration from 1200 to 200 cm^{-3} (hereafter referred to the "clean run"). Although this may be an unrealisticly low value for continental regions, the purpose is simply to show the storm's sensitivity to surface CCN changes. Fig. 29 shows the same vertical cross-section as was shown in Fig. 25, except for the clean run. Comparing these two figures, the updraft structure is very similar. Cloud water mixing ratio values peak at slightly smaller values in the clean run. This is likely because more of the cloud water is being transferred to other hydrometeors such as rain (because the cloud droplets are larger, as will be shown below). As a result of having smaller cloud water mass, the pristine ice mass is also smaller than the base case, peaking at just over 3 g kg^{-1}. So one very important result of this sensitivity test is that increasing surface CCN appears to increase the amount of ice mass in the upper portion of the storm. This is consistent with the pyroCB example shown in Section 5.3.

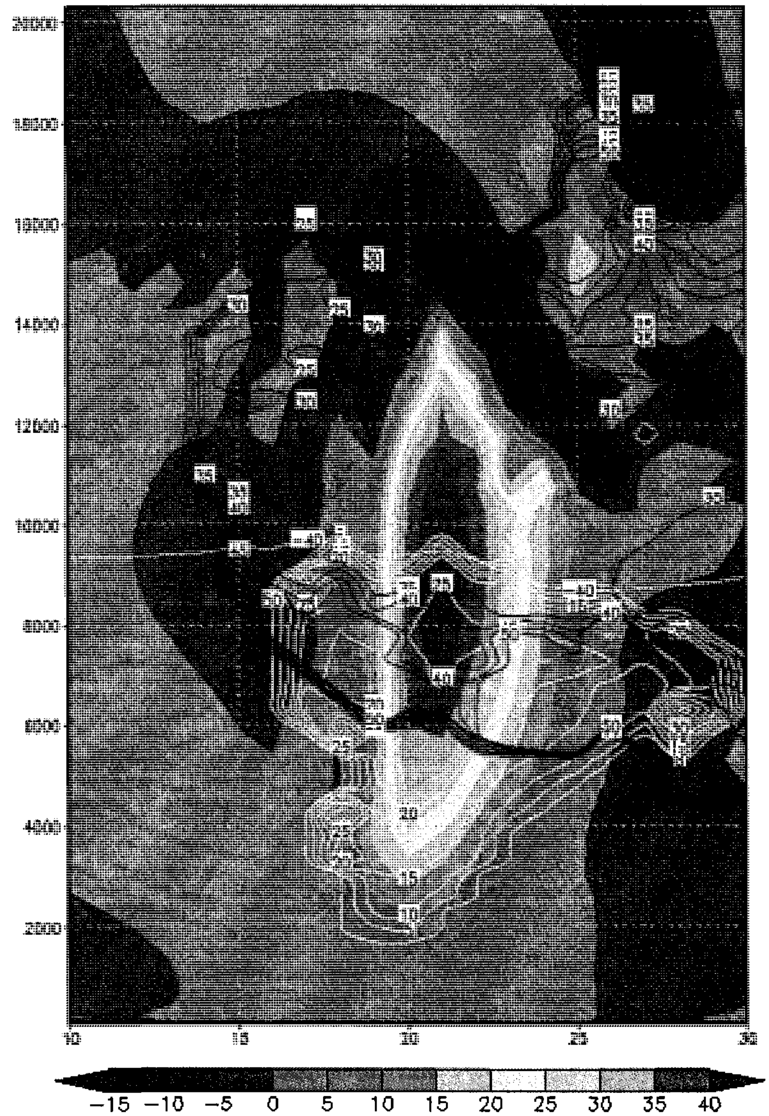

Figure 27. As in Fig. 25, except white contours are cloud droplet mean diameter (μm) and black contours are pristine mean diameter (μm).

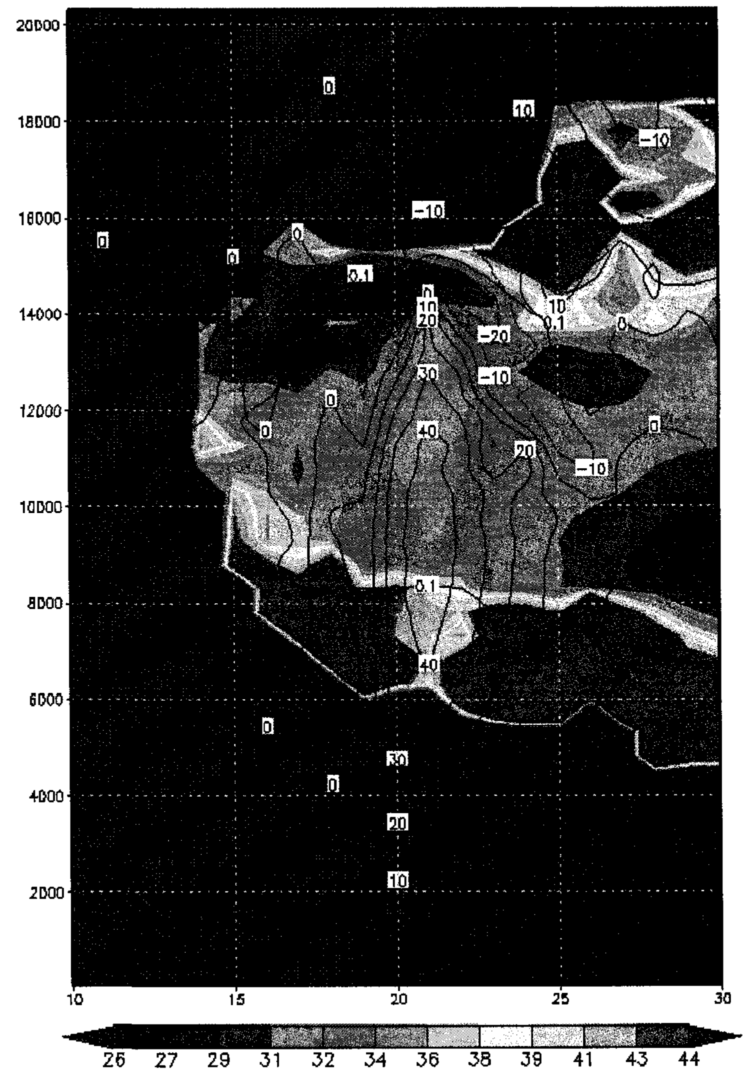

Figure 28. As in Fig. 25, except colors now indicate pristine ice mean diameter (μm) and the black contours show vertical velocity (m s^{-1}).

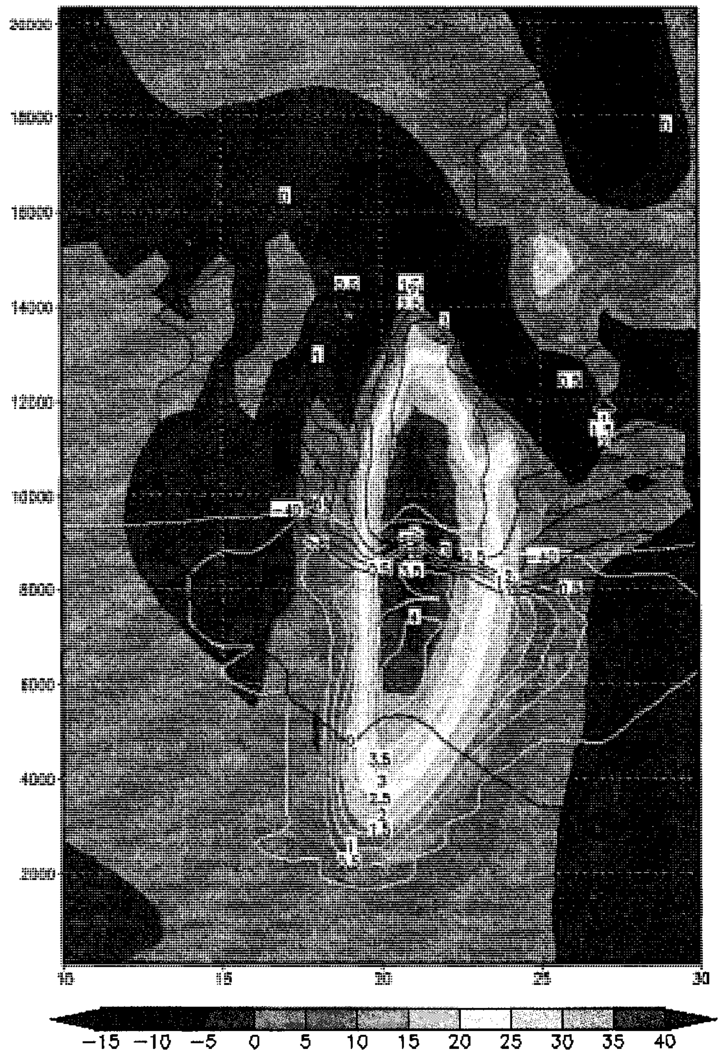

Figure 29. Same as Fig. 25 (cloud water and pristine ice mixing ratio), except for the simulation using a surface CCN concentration of 200 cm^{-3}.

Fig. 30 shows the cloud droplet and pristine ice number concentrations for the clean run. Comparing this to Fig. 26, it is evident that decreasing surface CCN values has a major effect on cloud droplet number concentrations, as we might expect. Peak values decrease by an order of magnitude. Similarly, the ice crystal numbers are significantly smaller since there are far fewer cloud droplets to be frozen homogeneously. Fig. 31 shows the resulting cloud droplet and pristine ice mean diameters for the clean case, and

Fig. 32 shows the pristine ice diameters more precisely. Both cloud droplet and pristine ice mean diameters are about 10 μm larger in the clean case. The reason for this trend is that the large decrease in cloud droplet numbers overwhelmed the modest decrease in mass, resulting in larger cloud droplets and therefore larger ice crystals. Again, this is consistent with the effective radius observations of the pyroCBs.

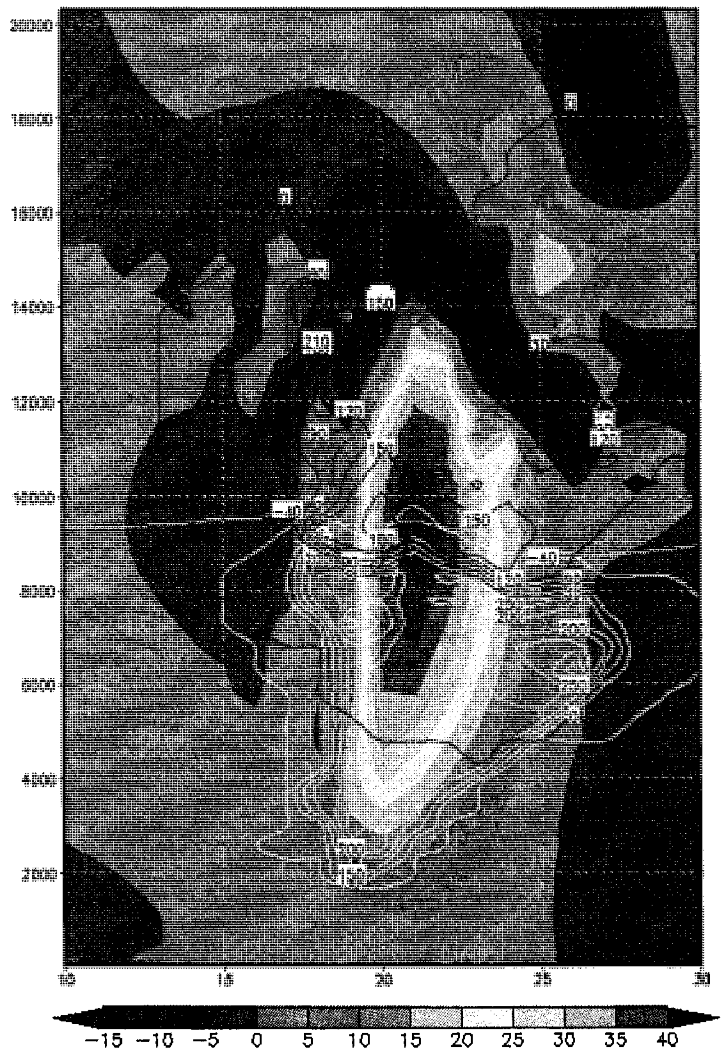

Figure 30. Same as Fig. 26 (cloud water and pristine ice number concentration), except for the simulation using a surface CCN concentration of 200 cm^{-3}.

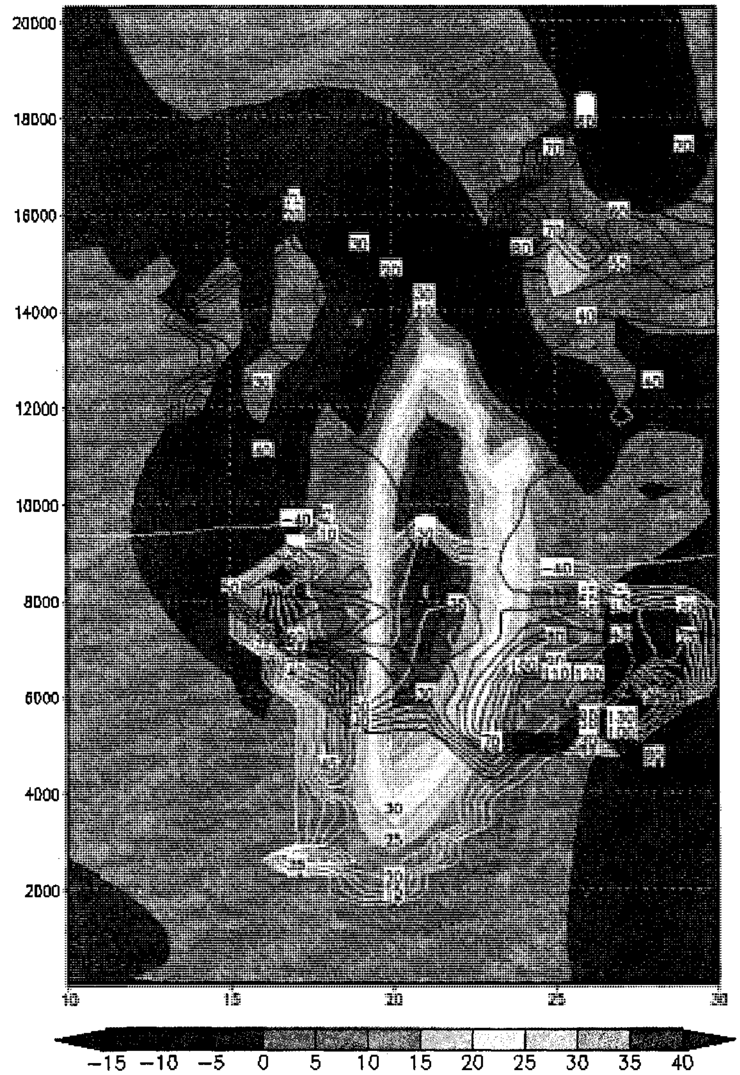

Figure 31. Same as Fig. 27 (cloud water and pristine ice mean diameter), except for the simulation using a surface CCN concentration of 200 cm^{-3}.

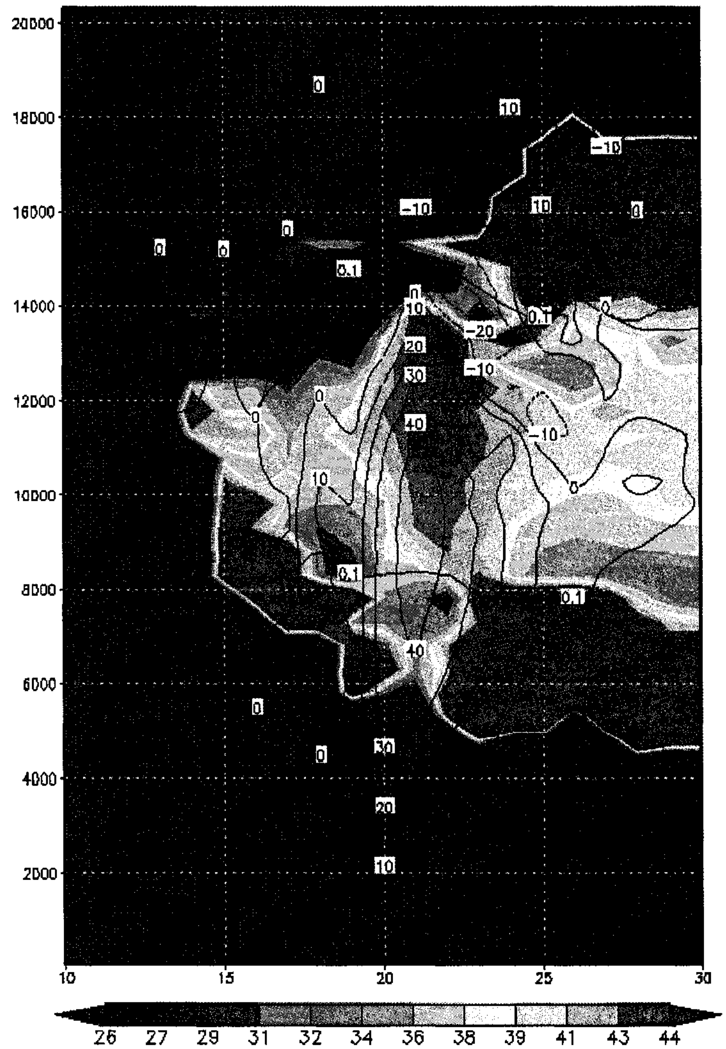

Figure 32. Same as Fig. 28 (pristine ice mean diameter in color), except for the simulation using a surface CCN concentration of 200 cm^{-3}.

5.4.3 Testing the Cloud Base Temperature Effect

As discussed in Section 5.2, a second factor which should have an impact on cloud-top ice crystal size is the cloud base temperature. There are two ways to achieve a colder cloud-base temperature: increase the surface elevation (like in the High Plains of the U.S.), and decrease the surface relative humidity. A larger surface temperature/dew point spread will result in a higher, and therefore colder, cloud base. For this sensitivity test, the input sounding is changed dramatically by both making the surface pressure lower and the surface much dryer; this new sounding is given in Fig. 33. The temperature and pressure of the LCL in this environment is -3 °C and 560 hPa, respectively. An "inverted-V" sounding of this nature is quite common in the High Plains during the summer months, such as near Denver, Colorado. This run will be referred to as the "high base case."

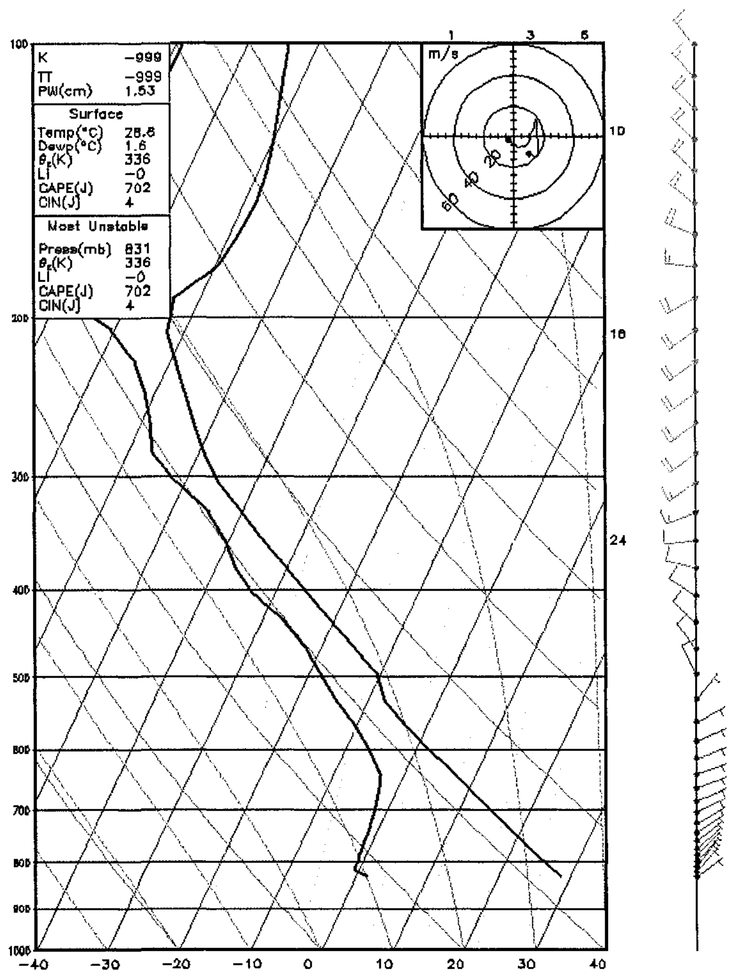

Figure 33. Sounding used to test the cloud base temperature effect.

Fig. 34 shows the time evolution of the midlevel updraft in the high base simulation. The initial warm bubble creates a fairly strong updraft which moves to the southeast with time. A vertical cross section is again taken at t = 55 min (along the black line in Fig. 34), and the cloud water and pristine ice mixing ratios are given in Fig. 35. Despite very steep mid-level lapse rates, the updraft strength in the case is weaker than in the base case. This is due to the extremely dry boundary layer. Also noteworthy is that the largest updraft values are nearly 9 km ASL, significantly higher than in the base case. Cloud water mixing ratio values are also nearly a factor of two smaller in the high base case. Its significantly colder cloud base temperature means less water vapor is available to form cloud droplets, hence the lower cloud water mass. Fig. 36 shows that cloud droplet concentrations are comparable with the base case simulation near their respective cloud bases, but the decrease with height is not as evident in the high base case. As cloud droplet size decreases, collection and riming efficiency also decrease (Rogers and Yao 1989), so more of these smaller cloud droplets are remaining cloud droplets and not being transferred to rain, graupel, or hail. Figs. 37 and 38 show the cloud droplet and pristine ice mean diameters. Cloud droplet mean diameters are approximately 5 μm smaller in the high base case due to smaller cloud water mass and approximately the same number concentrations. Pristine ice mean diameters are about 8 μm smaller in the dry case within the updraft core, but horizontal variations do exist within the anvil.

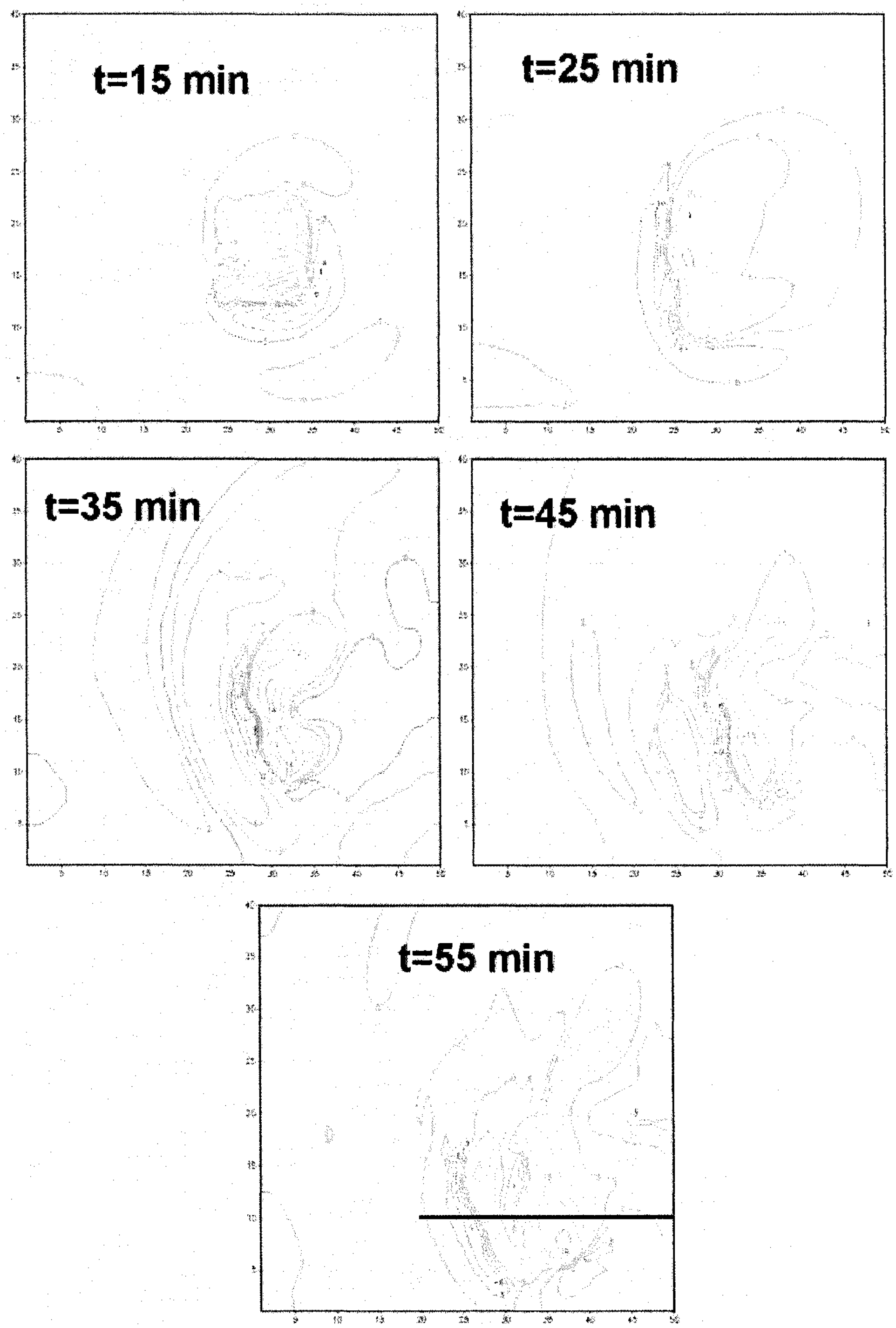

Figure 34. Same as Fig. 24, except for the high base case, and the horizontal cross-section is taken at z = 5 km ASL. The location of the forthcoming vertical cross-sections is shown by the black line at t = 55 min.

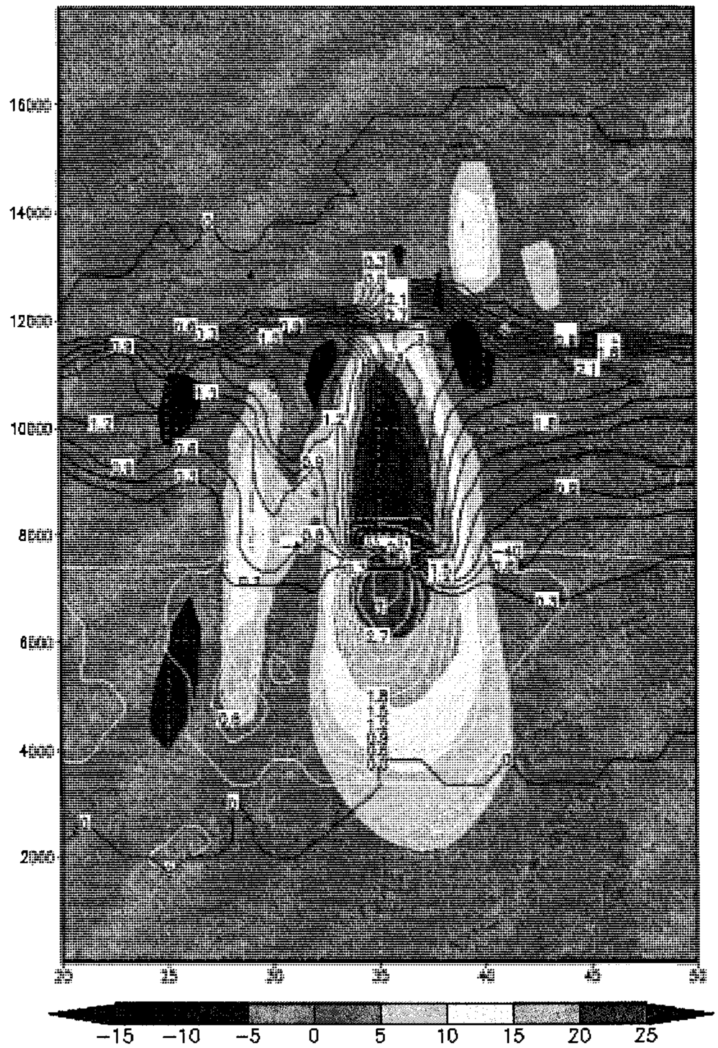

Figure 35. Same as Fig. 25 (cloud water and pristine ice mixing ratio), except for the high base case, and for a vertical cross-section shown at t = 55 min in Fig. 34.

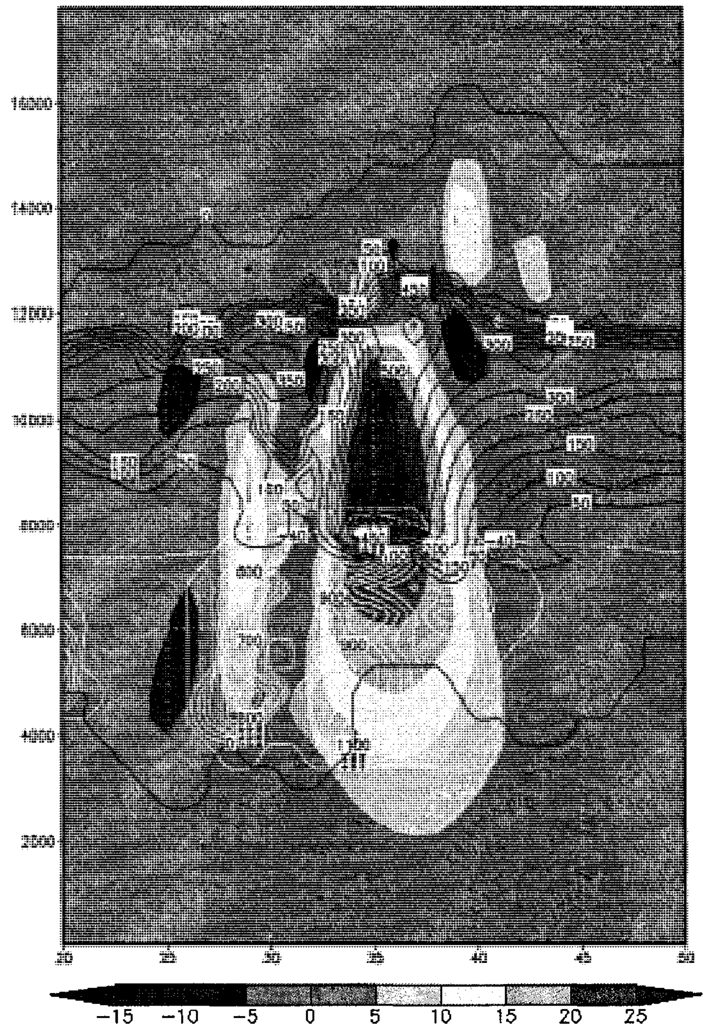

Figure 36. Same as Fig. 26 (cloud water and pristine ice number concentration), except for the high base case, and for a vertical cross-section shown at t = 55 min in Fig. 34.

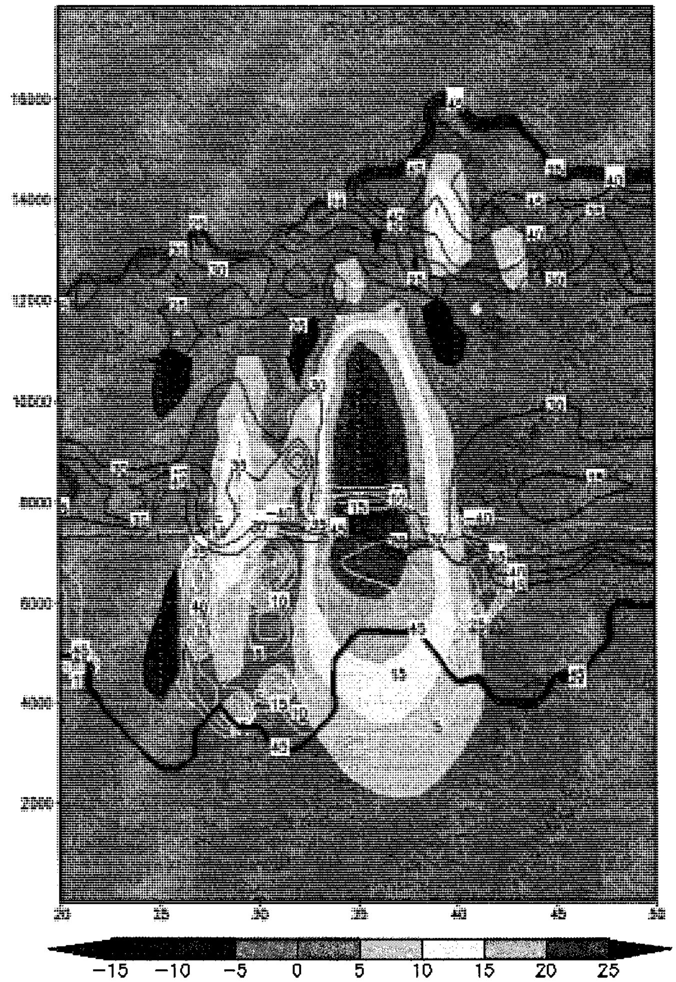

Figure 37. Same as Fig. 27 (cloud water and pristine ice mean diameter), except for the high base case, and for a vertical cross-section shown at t = 55 min in Fig. 34.

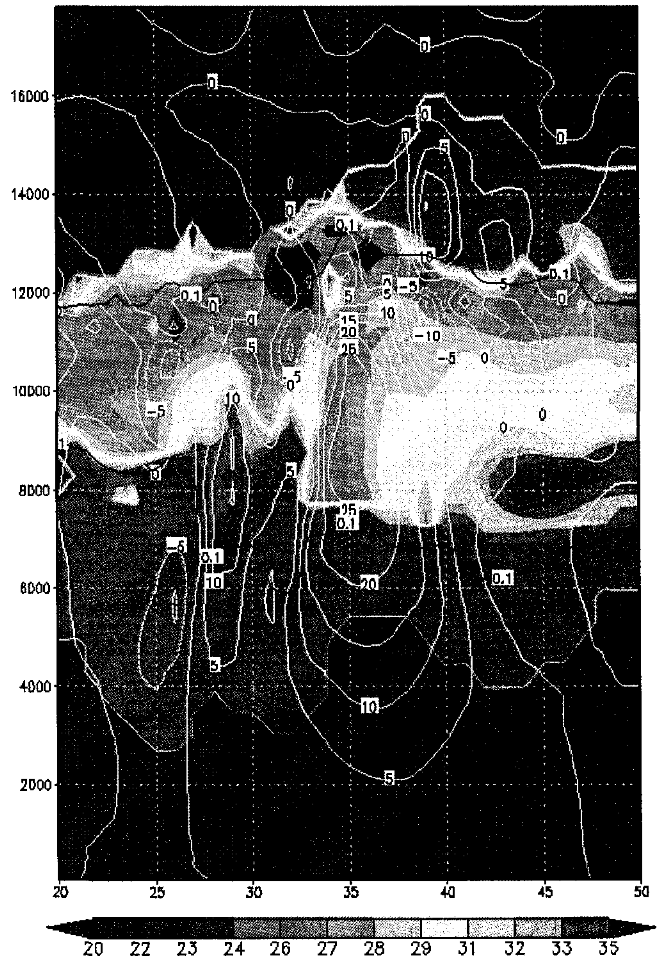

Figure 38. Same as Fig. 28 (pristine ice mean diameter in color), except for the high base case, and for a vertical cross-section shown at t = 55 min in Fig. 34.

5.4.4 Testing for Sensitivity to Updraft Strength

The statistical results given in Section 5.1 suggested that updraft strength may play a role in determining storm-top ice crystal size. To test this, another sensitivity test was designed to create a similar low-level environment as the base case, but the mid-level temperature lapse rate was adjusted to decrease atmospheric instability. This new input sounding is given in Fig. 39. A difference in the temperature lapse rate is very difficult to see by means of a visual comparison between Figs. 23 and 39, but the CAPE drops from 2651 to 1900 J kg^{-1}. This subtle decrease was necessary in order to ensure that the storm did not completely change its temporal evolution.

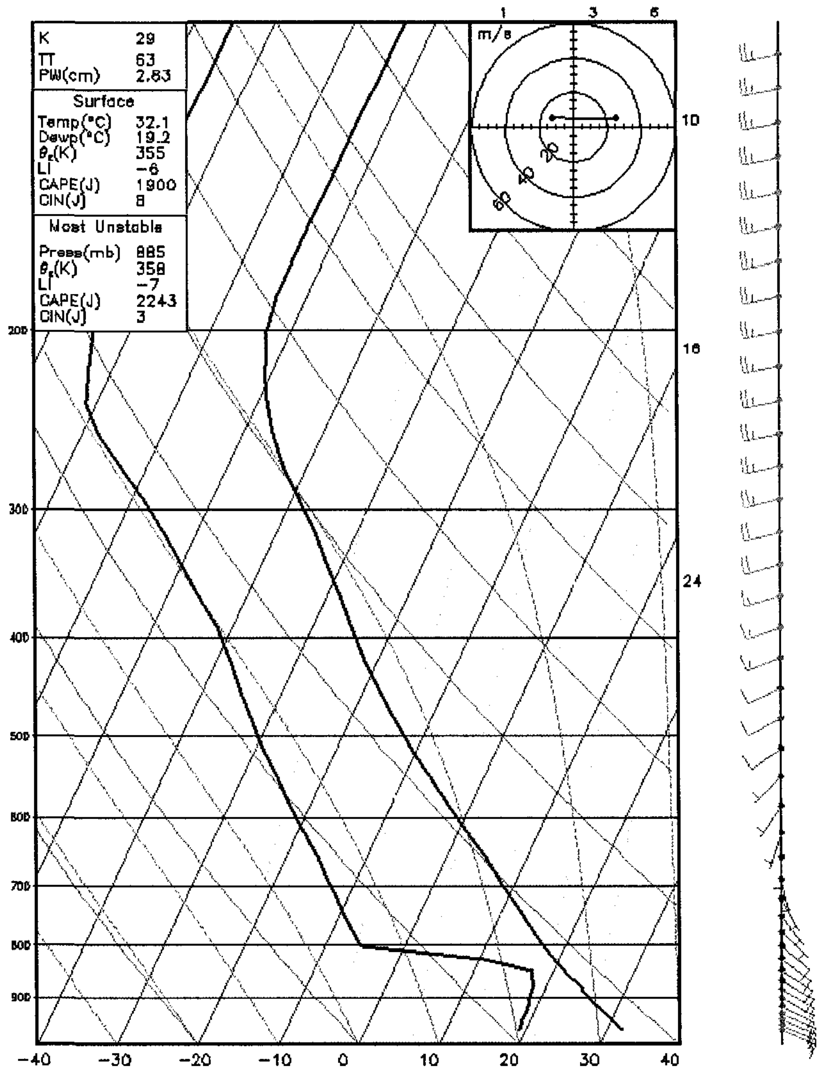

Figure 39. Sounding used to test the updraft strength effect.

Thirty-five minutes into the simulation, the updraft strength at 3 km ASL is indeed slightly weaker than in the base case (Fig. 40, compared with Fig. 24). Fig. 41 shows a vertical cross-section at the location given in Fig. 40 of updraft strength (contours) and pristine ice mean diameter (μm). Peak updraft magnitudes are about 15 ms^{-1} weaker in this case compared to the base case (Fig. 28), and pristine ice mean diameters are actually about 3 μm smaller in the weaker updraft case. This observation is due primarily to lower pristine ice mass above the homogeneous freezing level, despite having similar cloud water mass values. Perhaps the differing vertical location of the updraft peak played a role in the water mass partitioning. Regardless of the exact explanation, RAMS does not support the hypothesis that stronger updrafts leads to smaller cloud-top ice crystals. Following the discussion in Section 5.2, however, perhaps an updraft effect would be more pronounced for significantly smaller vertical velocities, since in those situations all CCN may not be activated (Fig. 17).

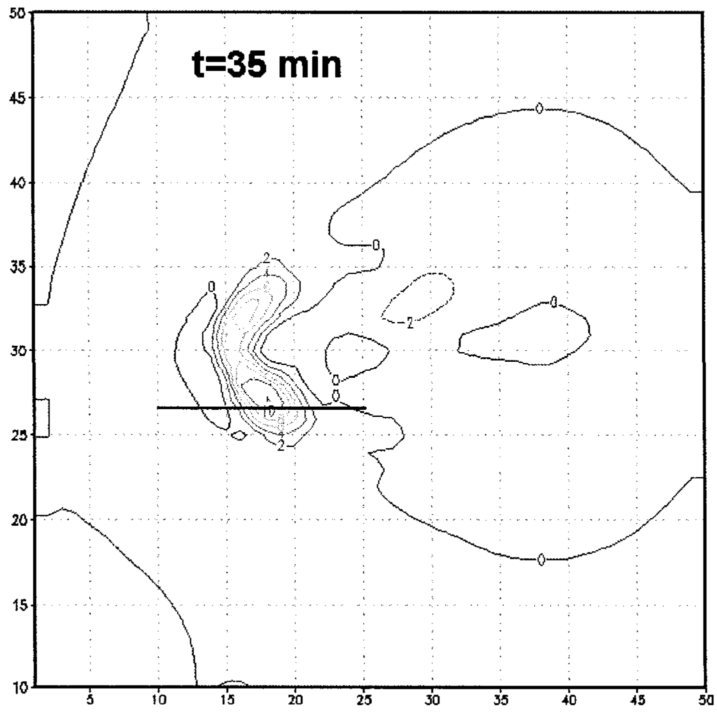

Figure 40. Horizontal cross-section of vertical velocity (ms^{-1}) at t = 35 min and z = 3 km ASL for the simulation using Fig. 39 as an input sounding. The black line shows the location of the vertical cross-section given in Fig. 41.

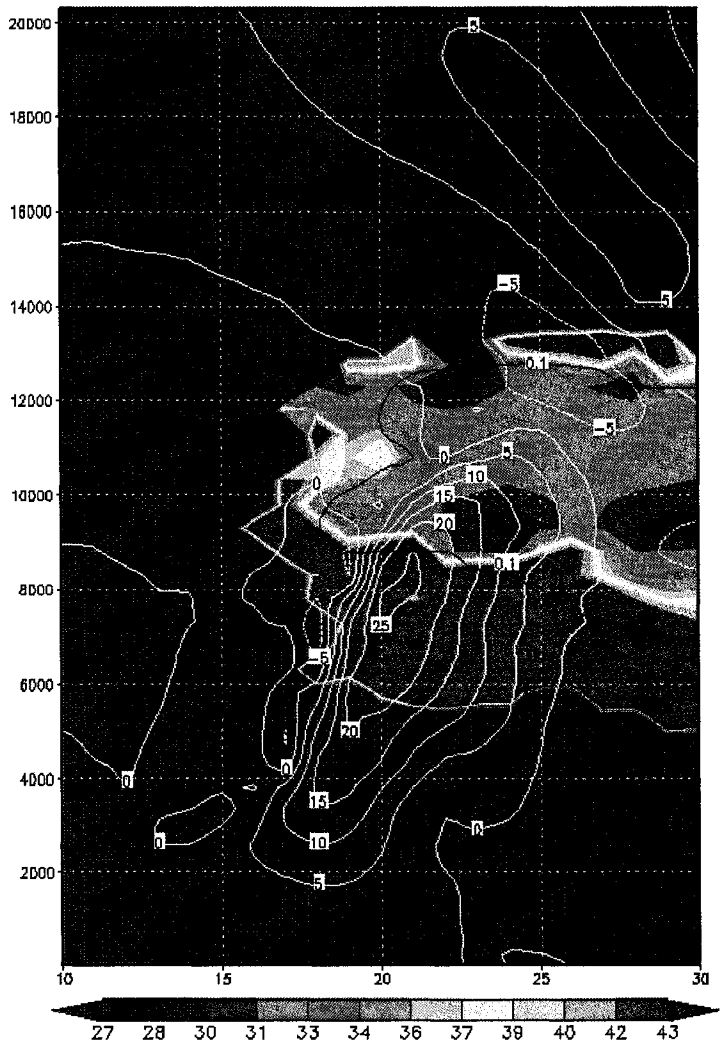

Figure 41. As in Fig. 28 (vertical velocity contoured and pristine ice mean diameter shaded), except using the more stable sounding.

CHAPTER 6

SUMMARY AND CONCLUSIONS

In this study, a number of methods are employed to examine the relationship between thunderstorm processes and storm-top ice crystal size. The difficulty in taking detailed in-situ measurements within intense convection necessitates the use of indirect observing methods, including satellite remote sensing. Using primarily the GOES 3.9 μm band, several climatologies were created over the continental U.S. The following observations were made from these maps:

- 3.9 μm reflectivity values are largest over the High Plains and parts of the Rocky Mountains of the U.S., with other maxima occurring downwind of other western mountain ranges
- A large east-west gradient in 3.9 μm reflectivity is found across the central plains, and mean values across much of the eastern U.S. are fairly uniform
- Differing mean values as viewed from GOES-East and GOES-West suggest that the scattering is not isotropic, and that forward scattering is preferred
- 3.9 μm reflectivity is slightly larger in the summer than in other months

Since 3.9 μm reflectivity varies with time due to sun-cloud-satellite geometry, it was necessary to correct for this effect by performing a particle size (effective radius) retrieval. Using an observational operator, a large number of model runs were performed which varied both cloud-top ice crystal size and scattering angle over a wide range of possible values. Output from these runs was used to populate a lookup table, so that with a GOES observation of visible reflectance, 3.9 and 10.7 μm brightness temperature, an estimate for cloud-top effective radius could be made. In this retrieval, only optically thick ice clouds were considered. The reason for this restriction was to minimize transmission from below and to ensure that only ice particles were being observed.

Several methods were used to validate the effective radius retrieval. First, a comparison with MODIS effective radius retrieval showed good agreement for the smaller sizes, but for larger sizes the GOES retrieval returned significantly larger values. The primary reason for this large difference is due to large errors in the GOES retrieval for large particles. A second validation effort compared GOES-East and GOES-West effective radius values in the central U.S. where their coverages overlap. This comparison also showed good agreement, suggesting that the assumed ice scattering properties were quite reasonable. Finally, an effective radius climatology was computed, and the GOES-East and GOES-West maps agreed closely in the region of overlap.

As a means of understanding the connection between the pre-storm environment and resulting cloud-top ice crystal size, a composite analysis was performed within the central Rocky Mountain region. Sixteen days having both large and small effective radii were selected, and mean values of several meteorological variables from the NARR were computed for each. Results show that storms having smaller cloud top ice crystals are associated with relatively large surface temperature/dew point spreads (and therefore higher cloud bases and colder cloud base temperatures), steeper mid-level lapse rates, and more instability. Since this was a purely statistical analysis, definite conclusions about physical mechanisms are not possible, but these results provide a good basis for cloud model runs.

Model simulations were performed using RAMS, a cloud model developed at Colorado State University. This model was chosen due to its sophisticated treatment of microphysics, specifically its ability to predict both the mass and number concentration of cloud water, pristine ice, and five other hydrometeors. As of the writing of this paper, the Weather Research & Forecasting (WRF) model's most advanced microphysics package only predicts the mass of cloud water, and it specifies the number concentration of ice which is homogeneously frozen rather than diagnosing it. Therefore, RAMS is superior to WRF for the purposes of examining cloud-top ice crystal information.

A base case simulation was performed using a supercell sounding with abundant low-level moisture. Next, a series of sensitivity tests were performed by changing various aspects of the base case initial state, including the initial CCN concentration, the low-level thermodynamic environment (following results from the statistical study), and the mid-level lapse rate (also following results from the statistical study). The most important results from these simulations are as follows:

- The base case simulation showed that the grand majority of ice particles within the simulated storm's anvil were frozen homogeneously (as opposed to heterogeneously), and that the size of the cloud droplets just prior to homogeneous nucleation roughly corresponds to the size of the ice crystals in the anvil.
- By decreasing the surface CCN concentration from 1200 to 200 cm^{-3}, the cloud droplet number concentration decreased by an order of magnitude, and the cloud water mass decreased slightly, probably due to more of the cloud mass being

transferred to rain, graupel, and hail. The net effect was that larger cloud droplets were formed. When these droplets froze homogeneously, the resulting pristine ice mass was smaller in the clean case, but the number concentrations were significantly smaller, so the pristine ice mean diameters were larger.

- When the input sounding was changed by making the surface pressure lower and the surface RH significantly larger, the resulting simulated storm had smaller cloud water mass compared to the base case, a direct result of the cloud base temperature being colder in the higher based storm. Smaller cloud droplets were then homogeneously frozen to produce smaller anvil pristine ice crystals.
- An attempt to determine whether updraft strength affected ice crystal size showed that there is very little sensitivity, at least for intense convection. The weaker updraft produced slightly smaller ice crystals.

After the multitude of methods to understand what determines thunderstorm-top ice crystal size, the primary mechanisms have been narrowed it down to two factors which are summarized in Fig. 42:

1) Boundary layer CCN concentration. Observational evidence from the pyroCB case, as well as cloud model simulations show that as more surface CCN become available, cloud droplets are smaller and more numerous, and as these are lofted to the -40 °C level, they freeze homogeneously resulting in small and numerous ice crystals. In Fig. 42a, the case on the left represents a situation with relatively few available CCN (clean), and the case on the right is for a relative abundance of CCN (dirty). In the clean case, larger cloud droplets are formed, resulting in larger ice crystals, while in the dirty case, smaller cloud droplets lead to more tiny ice crystals.

2) Cloud base temperature. Larger temperature/dew point spreads at the surface and lower surface pressures result in cloud bases forming at colder temperatures. This is represented by the vertical cross section in Fig. 42b; the storm on the left represents the colder cloud base temperature, and the storm on the right has a warmer cloud base temperature. Colder temperatures mean lower saturation vapor pressures, so less water vapor mass is available to be distributed among the available CCN, resulting in smaller cloud droplets. These smaller droplets then freeze homogeneously to form smaller ice crystals. Conversely, a warmer cloud base results in larger cloud droplets and ultimately larger cloud-top ice.

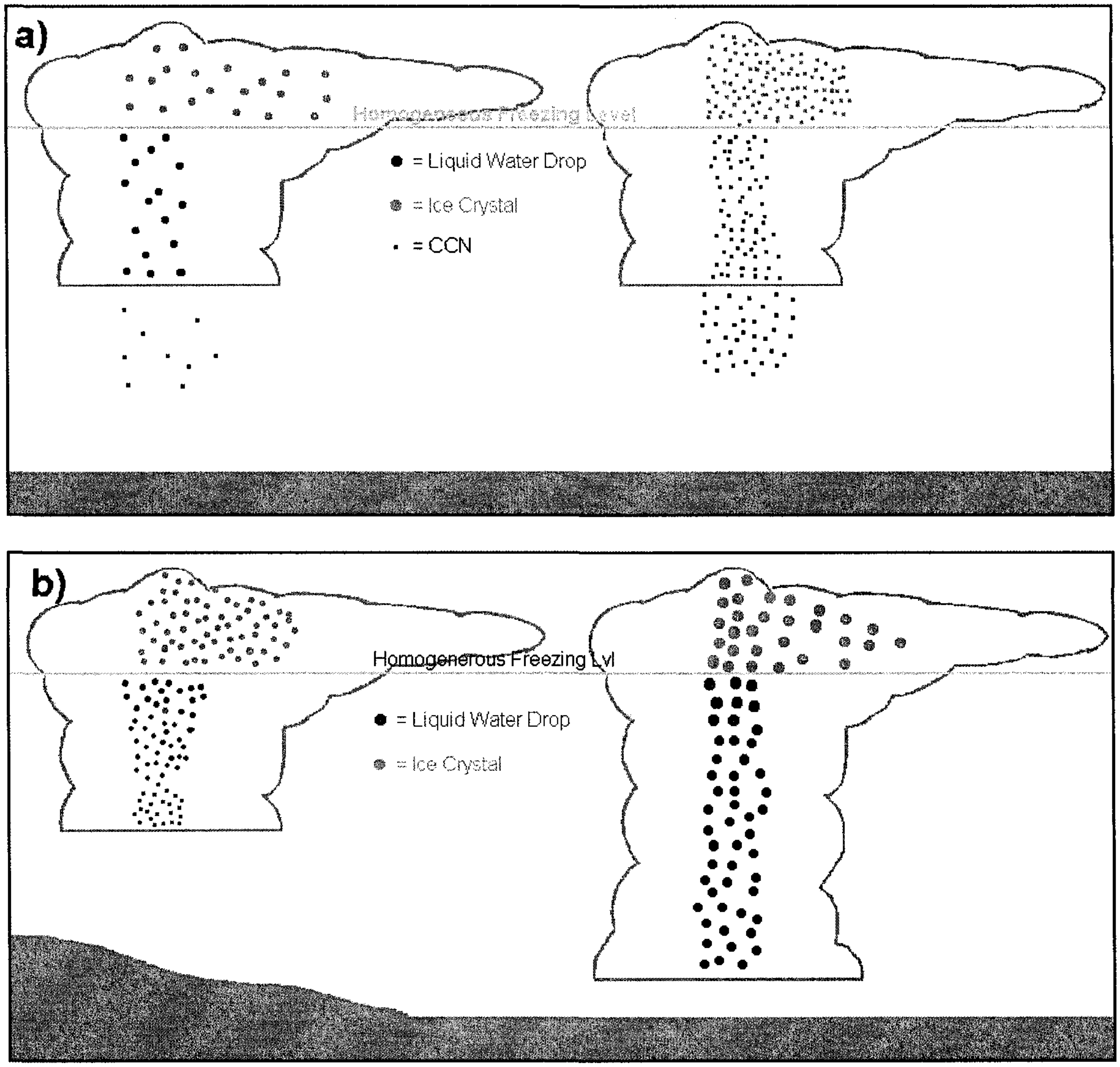

Figure 42. Conceptual diagram showing a vertical cross section of a) the CCN effect, and b) the cloud base temperature effect. The size of the dots represents the relative size of CCN (gray dots below cloud base), cloud droplets (blue dots), and ice crystals (gray dots in the upper portion of the storm).

In reality, both of these effects, as well as other less understood mechanisms, are likely constantly at work. In explaining the climatology of ice crystal size shown in Fig. 15, it is impossible to separate the relative contributions from CCN and cloud-base temperature, but CCN concentrations do not vary dramatically between the High Plains and points farther east (Demott 2008, personal communication). Therefore, over a continental region, mean cloud base temperature explains the majority of the geographical variation in mean ice crystal size.

Within the next ten years, advances in remote sensing technology will continue to aid in our understanding of thunderstorm microphysics. Specifically, the GOES-R series will have an Advanced Baseline Imager (ABI) which is capable of routine 5-minute imagery, double the resolution of the current GOES, and eleven additional spectral bands. This improvement will allow for more accurate particle size retrievals, and it may permit a similar retrieval for cloud droplet size of towering cumulus clouds. Such information may have severe weather nowcasting and forecasting utility, so continued research in this area is needed.

REFERENCES

Adler, R. F., and D. D. Fenn, 1979: Thunderstorm intensity as determined from satellite data. *J. Appl. Meteor.*, **18**, 502-517.

_____, M. J. Markus, and D. D. Fenn, 1985: Detection of severe midwest thunderstorms using geostationary satellite data. *Mon. Wea. Rev.*, **113**, 769-781.

Andreae M. O., D. Rosenfeld, P. Artaxo, A. A. Costa, G. P. Frank, K. M. Longo, and M. A. F. Silva-Dias, 2004: Smoking rain clouds over the Amazon. *Science*, **303**, 1337-1342.

Baum, B. A., A. J. Heymsfield, P. Yang, and S. T. Bedka, 2005: Bulk scattering properties for the remote sensing of ice clouds. Part I: Microphysical data and models. *J. Appl. Meteor.*, **44**, 1885-1895.

_____, P. Yang, A. J. Heymsfield, S. Platnick, M. D. King, Y. -X. Hu, and S. T. Bedka, 2005: Bulk scattering properties for the remote sensing of ice clouds. Part II: Narrowband models. *J. Appl. Meteor.*, **44**, 1896-1911.

Boudala, F. S., G. A. Isaac, N. A. McFarlane, and J. Li, 2007: The sensitivity of the radiation budget in a climate simulation to neglecting the effect of small ice particles. *J. Climate*, **20**, 3527-3541.

Cooper, S. J., T. S. L'Ecuyer, P. Gabriel, A. J. Baran, and G. L. Stephens, 2006: Objective assessment of the information content of visible and infrared radiance measurements for cloud microphysical property retrievals over the global oceans. Part II: Ice clouds. *J. Appl. Meteor. and Climate.*, **45**, 42-62.

Cotton, W. R., R. A. Pielke, Sr., R. L. Walko, G. E. Liston, C. J. Tremback, H. Jiang, R. L. McAnelly, J. Y. Harrington, M. E. Nicholls, G. G. Carrio, and J. P. McFadden, 2003: RAMS 2001: Current status and future direction. *Meteor. Atmos. Phys.*, **82**, 5-29.

DeMott, P. J., M. P. Myers, and W. Cotton, 1994: Parameterizations and impact of ice initiation processes relevant to numerical model simulations of cirrus clouds. *J. Atmos. Sci.*, **51**, 77-90.

Evans, K. F., 1998: The spherical harmonics discrete ordinate method for three-dimensional atmospheric radiative transfer. *J. Atmos. Sci.*, **55**, 429-446.

Fromm, M., R. Bevilacqua, R. Servranckx, J. Rosen, J.P. Thayer, J. Herman, and D. Larko (2005), Pyro-cumulonimbus injection of smoke to the stratosphere: observations and impact of a super blowup in northwestern Canada on 3-4 August 1998. *J. Geophys. Res.*, *110* (D8), D08205.

Grasso, L. D., and T. J. Greenwald, 2004: Analysis of 10.7-μm brightness temperatures of a simulated thunderstorm with two-moment microphysics. *Mon. Wea. Rev.*, **132**, 815-825.

Greenwald, T. J., R. Hertenstein, and T. Vukićević, 2002: An all-weather observational operator for radiance data assimilation with mesoscale forecast models. *Mon. Wea. Rev.*, **130**, 1882-1897.

Hillger, D. W., T. J. Schmit, and J. M. Daniels, 2003: Imager and sounder radiance and product validation for the GOES-12 science test. NOAA Tech. Rep., NESDIS 115, (September), 70p.

Intergovernmental Panel on Climate Change, 2007: The Physical Science Basis. Contribution of Working Group I to the Fourth Assessment Report of the IPCC.

Kidder, S. Q., and T. H. Vonder Haar, 1995: *Satellite meteorology: an introduction.* Academic Press, New York, 466pp.

King, M. D., W. P. Menzel, Y. J. Kaufman, D. Tanré, B. C. Gao, S. Platnick, S. A. Ackerman, L. A. Remer, R. Pincus, and P. A. Hubanks, 2003: Cloud and aerosol properties, precipitable water, and profiles of temperature and humidity from MODIS. *ieee Trans. Geosci. Remote Sens.*, **41**, 442-458.

Klemp, J. B., and R. B. Wilhelmson, 1978: The simulation of three-dimensional convective storm dynamics. *J. Atmos. Sci.*, **35**, 1070-1096.

_____, and _____, 1978: Simulations of right- and left-moving storms produced through storm splitting. *J. Atmos. Sci.*, **35**, 1097-1110.

Liljas, E., 1987: Multispectral methods for cloud classification. *Proc. Satellite and Radar Imagery Interpretation Workshop*, Reading, United Kingdom, European Organization for the Exploitation of Meteorological Satellites, 475-493.

Lindsey, D. T., D. W. Hillger, L. Grasso, J. A. Knaff, and J. F. Dostalek, 2006: GOES Climatology and Analysis of Thunderstorms with Enhanced 3.9 mm Reflectivity. *Mon. Wea. Rev.*, **134**, 2342-2353.

_____, and L. Grasso, 2008: An effective radius retrieval for thick ice clouds using GOES. *J. Appl. Meteor. and Climat.,* **47**, 1222-1231.

Maddox, R. A., 1981: Satellite depiction of the life cycle of a mesoscale convective complex. *Mon. Wea. Rev.*, **109**, 1583-1586.

McCann, D. W., 1983: The Enhanced-V: A satellite observable severe storm signature. *Mon. Wea. Rev.*, **111**, 887-894.

McKague, D. and K. F. Evans, 2002: Multichannel satellite retrieval of cloud parameter probability distribution functions. *J. Atmos. Sci.*, **59**, 1371-1382.

Melani, S., E. Cattani, V. Levizzani, M. Cervino, and F. Torricella, 2003: Radiative effects of simulated cirrus clouds on top of a deep convective storm in METEOSAT second generation SEVIRI channels. *Meteorol. Atmos. Phys.*, **83**, 109-122.

_____, E. Cattani, F. Torricella, and V. Levizzani, 2003: Characterization of plumes on top of a deep convective storm using AVHRR imagery and radiative transfer model simulations. *Atmos. Res.*, **67-68**, 485-499.

Mesinger, F., G. DiMego, E. Kalnay, K. Mitchell, P. C. Shafran, W. Ebisuzaki, D. Jovic, J. Woolen, E. Rogers, E. H. Berbery, M. B. Ek, Y. Fan, R. Grumbine, W. Higgins, H. Li, Y. Lin, G. Manikin, D. Parrish, and W. Shi, 2006: North American regional reanalysis. *Bull. Amer. Meteor. Soc.*, **87**, 343-360.

Minnis, P., K. -N. Liou, and Y. Takano, 1993: Inference of cirrus cloud properties using satellite-observed visible and infrared radiances. Part I: Parameterization of radiance fields. *J. Atmos. Sci.*, **50**, 1279-1304.

Meyers, M. P., R. L. Walko, J. Y. Harrington, and W. R. Cotton, 1997: New RAMS cloud microphysics parameterization. Part II: The two-moment scheme. *Atmos. Res.*, **45**, 3-39.

Nakajima, T. and M. King, 1990: Determination of the optical thickness and effective particle radius of clouds from reflected solar radiation measurements. Part I: Theory. *J. Atmos. Sci.*, **47**, 1878-1893.

Pielke, R. A., W. R. Cotton, R. L. Walko, C. J. Tremback, W. A. Lyons, L. D. Grasso, M. E. Nicholls, M. D. Moran, D. A. Wesley, T. J. Lee, and J. H. Copeland, 1992: A comprehensive meteorological modeling system -- RAMS. *Meteor. Atmos. Phys.*, **49**, 69-91.

Platnick, S. , M. D. King, S. A. Ackerman, W. P. Menzel, B. A. Baum, J. C. Riédi, and R. A. Frey, 2003: The MODIS cloud products: Algorithms and examples from Terra. *IEEE Trans. Geosci. Remote Sens.*, **41**, 459-473.

Purdom, J. F. W., 1973: Meso-highs and satellite imagery. *Mon. Wea. Rev.*, **101**, 180-181.

_____, 1976: Some uses of high-resolution imagery in the mesoscale forecasting of convection and its behavior. *Mon. Wea. Rev.*, **104**, 1474-1483.

Rogers, R. R. and M. K. Yau, 1989: A short course in cloud physics. Third Edition, 290 pp.

Rosenfeld, D. and I. M. Lensky, 1998: Satellite-based insights into precipitation formation processes in continental and maritime convective clouds. *Bull. Amet. Soc. Soc.*, **79**, 2457-2476.

_____, W. L. Woodley, A. Lerner, G. Kelman, and D. T. Lindsey, 2008: Satellite detection of severe convective storms by their retrieved vertical profiles of cloud particle effective radius and thermodynamic phase. *J. Geophys. Res.*, **113**, D04208, doi:10.1029/2007JD008600.

Saleeby, S. M., and W. R. Cotton, 2004: A large-droplet mode and prognostic number concentration of cloud droplets in the Colorado State University Regional Atmospheric Modeling System (RAMS). Part I: Module descriptions and supercell test simulations. *J. Appl. Meteor.*, **43**, 182-195.

Scorer, R. S., 1987: Convective rain as seen by channel 3. *Proc. Satellite and Radar Imagery Interpretation Workshop*, Reading, United Kingdom, European Organization for the Exploitation of Meteorological Satellites, 509-513.

Setvák, M., and C. A. Doswell III, 1991: The AVHRR channel 3 cloud top reflectivity of convective storms. *Mon. Wea. Rev.*, **119**, 841-847.

_____, R. M. Rabin, C. A. Doswell III, V. Levizzani, 2003: Satellite observations of convective storm tops in the 1.6, 3.7, and 3.9 μm spectral bands. *Atmos. Res.*, **66-67,** 607-627.

Stamnes, K., S. C. Tsay, W. Wiscombe, and K. Jayaweera, 1988: A numerically stable algorithm for discrete-ordinate-method radiative transfer in multiple scattering and emitting layered media. *Appl. Opt.*, **27**, 2502-2509.

Stephens, G. L., 1978: Radiation profiles in extended water clouds. Part II: Parameterization schemes. *J. Atmos. Sci.*, **35**, 2123-2132.

Turk, J., J. Vivekanandan, T. Lee, P. Durkee, and K. Nielsen, 1998: Derivation and applications of near-infrared cloud reflectances from GOES-8 and GOES-9. *J. Appl. Meteor.*, **37**, 819-831.

Van den Heever, S. C., and W. R. Cotton, 2007: Urban aerosol impacts on downwind convective storms. *J. Appl. Meteor. Clim.*, **46**, 828-850.

Weaver, J.F., D.T. Lindsey, D.E. Bikos, C.C. Schmidt, and E. Prins, 2004: Fire Detection using GOES-11 Rapid Scan Imagery. *Wea. Forecasting*, **19**, 496-510.

Wetzel, M. A., Borys, R. D., and Xu, L. E., 1996: *Satellite microphysical retrievals for land-based fog with validation by balloon profiling.* J. Appl. Meteor., **35**, 810-829.

Yang, P., K. N. Liou, K. Wyser, and D. Mitchell, 2000: Parameterization of the scattering and absorption properties of individual ice crystals. *J. Geophys. Res.*, **105**, 4699-4718.

_____, B. A. Baum, A. J. Heymsfield, Y. X. Hu, H. -L. Huang, S. -C. Tsay, and S. Ackerman, 2003: Single scattering properties of droxtals. *J. Quant. Spectrosc. Radiat. Transfer*, **79-80**, 1159-1169.

_____, H. Wei, H. -L. Huang, B. A. Baum, Y. X. Hu, G. W. Kattawar, M. I. Mishchenko, and Q. Fu, 2005: Scattering and absorption property database for nonspherical ice particles in the near- through far-infrared spectral region. *Appl. Optics*, **44**, 5512-5523.

_____, L. Zhang, G. Hong, S. L. Nasiri, B. A. Baum, H-L. Huang, and M. D. King, and S. Platnick, 2007: Differences between collection 4 and 5 MODIS ice cloud optical/microphysical products and their impact on radiative forcing simulations. *IEEE Trans. Geosci. Remote Sens.*, **45,** 2886-2899.